

AD-783 440

EXPERIMENTAL INVESTIGATION OF THE
EFFECTS OF HELICOPTER ROTOR DESIGN
PARAMETERS ON FORWARD FLIGHT STALL
CHARACTERISTICS

E. D. Bellinger, et al

United Aircraft Research Laboratories

Prepared for:

Army Air Mobility Research and Development
Laboratory

April 1974

DISTRIBUTED BY:

NTIS

National Technical Information Service
U. S. DEPARTMENT OF COMMERCE
5285 Port Royal Road, Springfield Va. 22151

Unclassified

SECURITY CLASSIFICATION OF THIS PAGE(When Data Entered)

20. Continued

fixed collective pitch. Torsional frequency was varied by using a special blade root flexure which would produce the required rigid blade torsional frequencies. Rotor performance, blade response, and boundary layer separation data were acquired to determine the occurrence and extent of blade stall.

Boundary layer information was obtained by means of the hot-film gages installed over the outer 25 percent span on the suction surface of two blade designs. The data obtained indicated consistently the azimuthal, chordwise, and radial location of stall onset and recovery and the laminar/turbulent transition of the boundary layer. The initiation of stall occurred on the retreating blade at approximately 300 deg but spread rapidly over the retreating portion of the rotor disc with increasing rotor lift and asymptotically approached an azimuthal extent of 200 deg encompassing the entire retreating side. The rotor lift at the stall threshold, indicated by hot-film measurements, was generally coincident with a change in rate of lift growth, vibratory flapping, and vibratory edgewise stress with increasing rotor shaft angle.

Based on the average of these stall indicators, it was possible to assess the effects of the various design parameters on stall for the specific flight conditions tested. The results indicated that camber and taper improved stall performance at the lower advance ratios (0.15 and 0.30); however, twist, aspect ratio, and increasing the number of blades from two to four had no significant effect. At the highest advance ratio tested (0.45), all rotors produced similar results with the exception of the four-bladed rotor, which demonstrated a lower stall threshold. Stall flutter responses were measured at stall threshold conditions but were manifested as impulsive-type nose-down deflections at higher stall conditions. Lowering the torsional frequency tended to delay the onset of stall flutter.

Unclassified

SECURITY CLASSIFICATION OF THIS PAGE(When Data Entered)

PREFACE

This experimental investigation of model rotor stall characteristics was sponsored by the Eustis Directorate, U. S. Army Air Mobility Research and Development Laboratory under Contract DAAJ02-72-C-0030, Task 1F162204AA4102. The work for this contract covered the period from January 1972 to October 1973 and was performed by United Aircraft Research Laboratories, East Hartford, Connecticut. The project was managed by Mr. A. J. Landgrebe. The experimental data were acquired by Messrs. L. E. Greenwald, B. W. Goepner, and W. P. Patrick. Reduction and analysis of performance and blade response data were performed by Messrs. E. D. Bellinger and A. J. Landgrebe. The hot-film data were reduced and analyzed by Messrs. W. P. Patrick, B. V. Johnson, and A. J. Landgrebe. Assistance in management of the program and preparation of the final report was provided by Mr. M. C. Cheney, Jr.

The technical representative of the Contracting Officer for this contract was Mr. Donald Merkley of the Eustis Directorate.

TABLE OF CONTENTS

	<u>Page</u>
PREFACE	iii
LIST OF ILLUSTRATIONS	vii
INTRODUCTION	1
TEST EQUIPMENT AND PROCEDURES	3
WIND TUNNEL	3
SMALL-SCALE ROTOR TEST RIG	3
MODEL ROTORS	3
HOT-FILM TEST EQUIPMENT	5
TEST VARIABLES	6
TEST PROCEDURES	8
ACCURACY OF DATA	9
EXPERIMENTAL RESULTS	12
ROTOR STALL CHARACTERISTICS FOR A TWO-BLADED ROTOR WITH UNTWISTED, UNTAPERED, AND UNCAMBERED BLADES	13
EFFECT OF BLADE TWIST	14
EFFECT OF BLADE SECTION CAMBER	16
EFFECT OF BLADE TAPER RATIO	17
EFFECT OF BLADE ASPECT RATIO	18
EFFECT OF NUMBER OF BLADES	19
EFFECT OF BLADE TORSIONAL FREQUENCY	21
SUMMARY OF STALL THRESHOLD DATA	22
BLADE BOUNDARY LAYER RESULTS	23
Determination of Boundary Layer Transition and Separation Indicators Using Hot-Film Gages	23
Boundary Layer Separation Results (Stall)	28
Effect of Thrust on Boundary Layer Separation	28
Effect of Spanwise Position on Boundary Layer Separation	29
Chordwise Extent of Boundary Layer Separation	30
Effect of Collective Pitch on Boundary Layer Separation	30
Effect of Advance Ratio on Boundary Layer Separation	31

	<u>Page</u>
Boundary Layer Transition Results	31
Effect of Thrust on Boundary Layer Transition	31
Effect of Azimuth Position on Chordwise Location of Transition Point	32
Comparison of Boundary Layer Separation and Transition Results	33
CONCLUSIONS	34
RECOMMENDATIONS	38
REFERENCES	128
APPENDIX -- TORSIONAL FLEXURES	129
LIST OF SYMBOLS	132

LIST OF ILLUSTRATIONS

<u>Figure</u>	<u>Page</u>
1 Model Rotor Test Rig in Wind Tunnel	39
2 Schematic Cross Section of Rotor Test Rig	40
3 Model Rotor Hub Region	41
4 Schematic of Model Rotor Blade Construction	42
5 Schematic of Hot-Film Gage Locations on Blade Suction Surface for Rotors Numbers 1 and 5	43
6 Resultant Velocity Estimates Used To Position Hot-Film Gages	44
7 Experimental Apparatus for Hot-Film Measurements	45
8 Rotor Number 1 Performance Data (Reference Rotor)	46
9 Effect of Collective Pitch on Rotor Lift at Stall Threshold Determined From Hot-Film Measurements for Rotor Number 1	49
10 Vibratory Flapping Data for Rotor Number 1	50
11 Vibratory Flatwise and Edgewise Stress Data for Rotor Number 1	52
12 Rotor Performance Based on Effective Drag for Rotor Number 1	53
13 Comparison of Rotor Lift at Stall Threshold Indicated by Hot-Film and Average Data for Rotor Number 1	54
14 Effect of Blade Twist on Rotor Performance	55
15 Effect of Blade Twist on Blade Flapping Response	58
16 Effect of Twist on Rotor Lift at Stall Threshold Indicated by Hot-Film Measurements	60
17 Effect of Blade Twist on Vibratory Flatwise and Edgewise Stress	61

<u>Figure</u>	<u>Page</u>
18 Effect of Blade Twist on Rotor Lift at Stall Threshold -- Average of All Stall Indicators	62
19 Effect of Blade Twist on Rotor Performance Compared on a Lift-Effective Drag Basis	63
20 Comparison of Vibratory Amplitudes and Longitudinal Harmonics of Blade Flapping	64
21 Comparison of Vibratory and Harmonic Amplitudes of Flatwise and Edgewise Stress	65
22 Harmonic Amplitudes of Blade Pitching Moment	66
23 Effect of Blade Section Camber on Rotor Performance	67
24 Effect of Blade Section Camber on Blade Flapping Response . .	70
25 Effect of Blade Section Camber on Vibratory Flatwise and Edgewise Stress Data	71
26 Effect of Blade Section Camber on Rotor Performance Compared on a Lift-Effective Drag Basis	72
27 Effect of Taper Ratio on Rotor Performance	73
28 Effect of Taper Ratio on Blade Flapping Response	76
29 Effect of Taper Ratio on Vibratory Flatwise and Edgewise Stress	77
30 Effect of Taper Ratio on Rotor Performance Compared on a Lift-Effective Drag Basis	78
31 Effect of Aspect Ratio on Rotor Performance	79
32 Effect of Aspect Ratio on Blade Flapping Response	82
33 Effect of Aspect Ratio on Vibratory Flatwise and Edgewise Stress	83
34 Effect of Aspect Ratio on Rotor Performance Compared on a Lift-Effective Drag Basis	84

<u>Figure</u>	<u>Page</u>
35 Effect of Number of Blades on Rotor Performance	85
36 Effect of Number of Blades on Blade Flapping Response	88
37 Effect of Number of Blades on Vibratory Flatwise and Edgewise Stress	89
38 Effect of Number of Blades on Rotor Performance Compared on a Lift-Effective Drag Basis	90
39 Effect of Torsional Frequency on Rotor Performance - $\bar{\omega}_\theta = 12$	91
40 Effect of Torsional Frequency on Rotor Performance - $\bar{\omega}_\theta = 9$	94
41 Effect of Torsional Frequency on Rotor Performance - $\bar{\omega}_\theta = 5$	97
42 Effect of Torsional Frequency on Blade Flapping Response - $\bar{\omega}_\theta = 5$	100
43 Effect on Torsional Deflection of Increasing Rotor Lift by Increasing Shaft Angle	101
44 Effect of Torsional Frequency on Oscillatory Torsional Deflection Onset	103
45 Comparison of the Average Rotor Lift Coefficient to Solidity Ratio at Stall Threshold Indicated by Hot-Film, C_L/σ , Flapping and Edgewise Stress Data	104
46 Experimental Apparatus for Correlation Tests Between Oil-Film Flow Visualization and Hot-Film Measurements	105
47 Flow Patterns on Nonrotating NACA 0012 Airfoil Determined by Oil-Film Flow Visualization	106
48 Output Voltages From Hot Films Mounted on Nonrotating NACA 0012 Airfoil	107
49 Oscilloscope Outputs of Hot-Film Signals at 85% Span	108

<u>Figure</u>	<u>Page</u>
50 Oscilloscope Outputs of Hot-Film Signals for Rotor Number 5	110
51 Azimuthal Boundaries of Stall for Variations of Rotor Lift as Determined by Hot-Film Gages on Rotor Number 5	114
52 Spanwise Variations in Stall Boundaries at 75% Chord for Rotor Number 5	115
53 Spanwise Variations in Stall Boundaries at 75% Chord for Rotor Number 1	116
54 Chordwise Variations in Azimuthal Extent of Separated Boundary Layer at 75% Span	117
55 Effect of Collective Pitch on Stall Boundaries as Determined From Hot-Film Gage Data for Rotor Number 1	118
56 Effect of Collective Pitch on Stall Boundaries as Determined From Hot-Film Gage Data for Rotor Number 5	119
57 Effect of Advance Ratio on Stall Boundaries at 75% R, 75% c for Rotor Number 1	120
58 Effect of Advance Ratio on Azimuthal Extent of Stall at 75% R, 75% c for Rotor Number 5	121
59 Azimuthal Extent of Laminar and Turbulent Boundary Layer at 25% Chord as Determined From Hot-Film Gage Data	122
60 Chordwise Variations in Location of Boundary Layer Transition Point at 85% Span	123
61 Effect of Thrust Level on Boundary Layer Flow Charac- teristics as Determined From Hot-Film Gages	124
62 Schematic Cross Section of Torsional Flexure	125
63 Hub, Torsional Flexure, and Blade	126
64 Exploded View of Torsional Flexure	127

INTRODUCTION

The principal factor limiting the forward velocity of rotary-wing aircraft is known to be the occurrence of retreating blade stall. Since stall occurs over a fraction of the rotor disc, the forward velocity capability is usually dictated by the degree of penetration into the stall regime before adverse effects such as power losses, increased vibration, etc., become intolerable. Hence, the rotary-wing designer is relatively more concerned about the details of stall aerodynamics than is his fixed-wing counterpart. Unfortunately, rotary-wing stall is more complex than fixed-wing stall due to the influence of unsteady and radial flow effects. Additional complexity of rotor stall is created by the influence of the complicated flow field induced by the rotor's helical wake. Therefore, it seems quite natural that conventional theories which assume steady aerodynamics, constant inflow, and no radial flow effects would predict significantly different performance as the rotor blades encounter stall. More recent and sophisticated theories have relieved the above assumptions and have improved the correlation of predicted rotor performance with experimental results when rotor blades encounter stall. Despite the importance of rotor stall characteristics, a shortage exists of systematic performance data for rotors operating in a stalled environment. Available data have generally been obtained as one-of-a-kind tests, thus making it difficult to define or isolate the effects of individual rotor design parameters on rotor stall.

Although obviously desirable, full-scale rotor tests are expensive and introduce significant blade aeroelastic effects which both limit the range of conditions that can be tested and complicate the analysis of the data. Stall characteristics of model rotors can be expected to differ in detail from those of full-scale rotors due to Reynolds number effects; however, evidence exists that the same gross discrepancies between predicted and measured stall results are noted at both model and full scale. Measurement of the effect of rotor parameters on such discrepancies provides a systematic body of data to correlate with improved analyses. Substantiating test data are obviously desirable to assess the validity of such analyses.

The tests of model rotor blades were particularly appropriate at this time because of the availability of blades fabricated and tested under Eustis Directorate Contracts DAAJ02-69-C-0056 and DAAJ02-71-C-0012 which evaluated rotor wake and performance characteristics in hover. The results of these experiments are reported in Refs. 1 and 2. The use of these blades permitted testing to be extended to the forward flight regime with minimum expense. As with the hover tests, the objective of the forward

flight tests was to determine the effects of number of blades, aspect ratio, twist, camber, and taper on performance. Of particular interest was to determine these effects on forward flight stall characteristics. An additional objective was to explore the influence of blade torsional frequency on blade stall.

TEST EQUIPMENT AND PROCEDURES

WIND TUNNEL

The tests were conducted in the UAC 4- x 6-ft subsonic wind tunnel which has a closed return, closed throat circuit and operates with a maximum test section velocity and Reynolds number of 100 mph and 0.88×10^6 per ft, respectively. Static pressure in the irregular octagonal test section is atmospheric. Complete specifications for the tunnel are given in Ref. 3.

SMALL-SCALE ROTOR TEST RIG

The rotor test rig employed in this program is shown in Fig. 1. It was designed primarily for exploratory testing of small-scale rotors in the 4- x 6-ft subsonic wind tunnel. Power to the rotor is supplied through a 3-to-1 speed reduction system by a 40-hp, variable-speed electric motor. The motor, transmission, and rotor force measuring system are mounted outside the tunnel above the test section as shown schematically in Fig. 2. Rotor thrust, drag, and torque are measured by means of strain-gaged bending beams. (Drag bending beams not shown in Fig. 2). A 25-unit slip-ring assembly mounted on the rotor drive shaft provides a signal transfer point for measuring rotor blade motions and stresses as well as data from blade-mounted hot-film gages. Longitudinal and lateral vibrations are monitored using conventional pickups mounted immediately above the rotor hub.

MODEL ROTORS

Ten model rotor configurations were tested to determine the effects of number of blades, blade twist, aspect ratio, airfoil section, planform taper, and blade torsional frequency. The design parameters investigated are summarized in Table I. Blade flapping hinges were provided; however, no lag hinges or cyclic pitch were used. The flapping angle at the flapping hinge of one blade was measured by means of an arrangement consisting of a strain-gaged bending beam mounted on the hub and an eccentric cam on the end of the flapping pin. A close-up of the hub and root fittings is shown in Fig. 3.

The model blade design consisted of an aluminum spar and a balsa trailing-edge section, as shown in Fig. 4. The blades were designed such that the elastic axis, section center of gravity, and center of pressure were coincident at the quarter-chord position (within 1 percent of the chord).

TABLE I. MODEL ROTOR CHARACTERISTICS

$\Omega R = 300$ fps

Rotor No.	No. of Blades	Twist (deg)	Chord (in.)	Aspect Ratio	Airfoil Profile	Taper Ratio	1st Torsional Frequency (cycles/rev)*	Diameter (ft)	Solidity $bc_{3/4}/\pi R$	Cifset Ratio
1.	2	0	1.47	19.2	0012	1:1	22	4.694	.03323	.0297
2.	2	0	1.47	19.2	0012	1:1	12	4.694	.03323	.0297
3	2	0	1.47	19.2	0012	1:1	9	4.694	.03323	.0297
4	2	0	1.47	19.2	0012	1:1	5	4.694	.03323	.0297
5	2	-8.4	1.47	19.2	0012	1:1	23	4.694	.03323	.0297
6	4	-8.4	1.47	19.2	0012	1:1	23	4.694	.06645	.0297
7	2	0	1.47	19.2	23112	1:1	23	4.694	.03323	.0297
8	2	0	1.47**	19.2	0012	2:1	42	4.694	.03323	.0297
9	2	-8.4	1.96	14.4	0012	1:1	24	4.694	.04430	.0297
10	2	0	1.47	17.5	0012	1:1	24***	4.300	.03628	.0325

*Frequencies above 12 are with flexure locked out.

**Chord measured at 0.50R.

***w/o torsional flexure system.

The mass and stiffness of the model blades greatly exceeded those of model blades dynamically scaled to typical full-scale blades. For example, the Lock number of the blades with an aspect ratio of 19.2 was approximately 4 compared to a typical full-scale Lock number of 10. Hence, model blade coning angles were lower than full-scale coning angles. However, the use of such rotor blades permitted concentration on the aerodynamic, rather than aeroelastic, aspects of rotor performance.

A specially designed blade cuff (Fig. 3) with interchangeable torsional springs was used to vary blade torsional frequency. Strain gages mounted on the blade cuff torsional spring were used to measure blade torsional deflection. The design of the "torsional-flexure" blade cuff is detailed in the Appendix. Strain gages to measure flatwise, edgewise, and torsional stresses were mounted at critical locations on the blade spar. These stresses, along with the blade torsional deflection and flapping angle, were monitored and recorded during testing.

HOT-FILM TEST EQUIPMENT

An understanding of the stall characteristics of a helicopter rotor requires detailed knowledge of the character of the boundary layer on the blade surface. To obtain this knowledge, several hot-film gages were mounted on the suction surface of two blades to distinguish between laminar, turbulent, transitional, and separated boundary layer flow over the blade. By monitoring the energy dissipated by the heated films (i.e., the local shear stress), the thrust level and the spanwise, chordwise, and azimuthal location of the onset of (and recovery from) rotor blade stall could be determined.

Equipment used to obtain the hot-film measurements consisted of two rotor blades, each instrumented with twelve hot-film gages, a constant-temperature anemometer to heat the gages, and auxiliary equipment to record and monitor the data.

Two uncambered rotor blades having zero and -8.1 deg of linear twist were instrumented with ETG-50A temperature-sensor film gages as shown in Fig. 5. Twelve gages were mounted on the suction surface of each blade. Nine of these gages were located in a matrix at the 25-, 50-, and 75-percent chord positions at the 75-, 85-, and 95-percent spanwise stations; two additional gages were located at the 5- and 15-percent chord at the 85-percent spanwise station.

As shown in Fig. 5, the hot-film gages at each spanwise location were arranged along a line which intersected the blade leading edge at an angle of 45 deg. The gages were placed after considering the maximum flow angle deviation of the resultant section velocity expected over the outer 25-percent span of the rotor during the test program as shown in Fig. 6. Maximum inflow and outflow angles were calculated to be 37.5 deg at $\psi = 215$ deg and 325 deg, respectively, at 75-percent span for an advance ratio of 0.45. Although it is recognized that the flow direction of the resultant section velocity only approximates the direction of flow in the blade boundary layer, it is felt that alignment of the gages at 45 deg to the leading edge ensured that no gage was influenced by the thermal boundary layer from an upstream gage. Special procedures were used in mounting each hot-film gage to ensure that the energy dissipation rate of the gage was dependent solely upon the heat flux rate to the moving airstream rather than upon heat transfer to the blade surface.

The experimental setup used to obtain the hot-film measurements is shown schematically in Fig. 7. The temperature sensor gages were powered by a ten-channel constant-temperature anemometer. External resistances were used to load the anemometer bridge to impose a 20-percent overheat to the temperature sensor gages. The hot-film electrical output signals were transferred to the constant-temperature anemometer through a slip-ring unit on the rotor shaft (see Fig. 7). Two slip rings were used to provide each hot-film gage with a separate ground connection. The slip rings were loaded with double strength springs to obtain clean signals without slip-ring noise.

The output voltages of selected constant-temperature anemometer channels were monitored on a four-channel oscilloscope which was triggered by the 1/rev signal from the rotor. DC voltages and rms values of the AC voltage component were measured on a digital multimeter. Analog signals from the hot-film gages were recorded on magnetic tape and Visicorder strip charts; oscilloscope pictures were taken at selected operating parameters.

TEST VARIABLES

The experimental data for each model rotor were obtained for a matrix of test points consisting of variations in collective pitch (6, 9, 12 deg), advance ratio (0.15, 0.30, 0.45), and shaft angle (-16 deg to max). The maximum collective pitch could not be tested at all advance ratios due to limiting blade stresses. Rotor shaft angle was varied in increments of no more than two degrees with a minimum of eight points per run (a given collective pitch and advance ratio). In regions believed to be near the stall boundary, rotor shaft angle increments of one degree or less were

used, and in cases where stall was deeply penetrated fewer than eight shaft angles could be safely tested due to large edgewise stress levels.

Two uncambered rotors having zero and -8.4 deg of linear twist were instrumented with hot-film gages. Twelve gages were located on the suction surface of each blade as shown in Fig. 5. Using hot-film equipment, the spanwise and chordwise progression of the separated region of the boundary layer and the growth of the azimuthal extent of stall with increasing rotor thrust level were measured over the outer 25 percent span for two uncambered, untapered rotor blade configurations having zero and -8.4 deg of linear twist at the conditions shown in Table II. In addition, the extent of laminar, turbulent, and transitional boundary layer flow was determined at each gage location.

TABLE II. HOT-FILM TEST PARAMETERS

Blade Twist (deg)	Gage Location	Collective Pitch (deg)				
		at $\mu = 0.15$	at $\mu = 0.30$	at $\mu = 0.45$		
0	75% R	25% c	6, 9, 12	6, 9, 12	6, 9, 12	
		50% c	-	6, 12	-	
		75% c	6, 9, 12	6, 9, 12	6, 9, 12	
	85% R	5% c	6, 9	6, 9	6, 9	
		15% c	6, 9	6, 9	6, 9	
		25% c	6, 9	6, 9	6, 9	
		50% c	6, 9	6, 9	6, 9	
		75% c	6, 9, 12	6, 9, 12	6, 9, 12	
	95% R	25% c	6, 9, 12	6, 9, 12	6, 9, 12	
		50% c	-	6, 12	-	
		75% c	6, 9, 12	6, 9, 12	6, 9	
	-8.4	75% R	25% c	6, 9, 12	6, 9, 12	6, 9
			50% c	6, 9, 12	6, 9, 12	6, 9
			75% c	6, 9, 12	6, 9, 12	6, 9
		85% R	5% c	-	6	-
15% c			-	6	-	
25% c			-	6, 9	-	
50% c			-	6, 9	-	
75% c			6, 9, 12	6, 9, 12	6, 9	
95% R		25% c	6, 9, 12	6, 9, 12	6, 9	
		50% c	6, 9, 12	6, 9, 12	6, 9	
		75% c	6, 9, 12	6, 9, 12	6, 9	

TEST PROCEDURES

The general procedure for testing a given rotor was as follows. Blade collective pitch was set manually and data were gathered over a range of rotor angles of attack for each of three advance ratios (0.15, 0.30, 0.45). At least two collective pitch settings were tested for each model rotor.

For each model rotor, the following were measured:

rotor thrust

rotor torque

rotor drag

blade flatwise stress

blade edgewise stress

blade pitching moment

blade flapping angle

blade torsional deflection (for root spring conditions)

blade azimuth angle

hot-film gage data (on two selected rotors)

Rotor thrust, torque, and drag were measured with Baldwin self-balancing potentiometers; while blade stresses, torsional deflection, flapping angle, and an azimuth reference pulse were recorded on both FM tape and oscillograph charts.

The hot-film data were acquired in the following manner. The DC voltage level, E_0 , was recorded for each hot-film gage with the nonrotating rotor in still air. The rotor and wind tunnel were then brought up to operating speed for a desired advance ratio, and a shaft angle traverse was commenced. Initial measurements were made at the minimum thrust condition ($\alpha_s = -16$ deg). The shaft was then tilted in 2- or 4-deg increments in the positive direction (i.e., direction of increasing rotor thrust level) until maximum permissible rotor airloads or vibrations were encountered.

During the shaft angle traverse the output signal from the hot-film gage located at 75-percent span and 75-percent chord was monitored on the oscilloscope to determine within 1/2 deg the shaft angle at which the stall threshold occurred at that gage location. This gage proved to be an excellent "stall indicator" because with few exceptions it indicated boundary layer separation at a lower thrust level than any other hot-film gage on the blade surface. Generally, after determining the shaft angle at which stall initiation occurred, a second shaft angle traverse was made over a limited range near the stall threshold point in 1 deg, and occasionally 1/2 deg, increments to obtain more detailed information concerning the initiation and propagation of the separated boundary layer on the blade surface.

At each shaft angle for which thrust data were measured, hot-film data were recorded on magnetic tape and Visicorder analog traces; in addition, photographs of oscilloscope traces of the hot-film output signals were taken at selected operating conditions.

ACCURACY OF DATA

The estimated accuracies with which the parameters determining a given test condition could be set or determined are as follows:

<u>Parameter</u>	<u>Accuracy</u>
Collective Pitch	± 0.2 deg
Tip Speed	± 1 fps
Shaft Angle	± 0.05 deg
Tunnel Speed	± 1 fps
Air Temperature	± 2°F

The static data repeatability for thrust, drag, and torque was derived from repeated calibrations of the strain gages made while determining the calibration derivatives for conversion of strain-gage units (SGU's) into forces or moments. The dynamic data repeatability was established by considering the range of C_L/σ , C_Q/σ , and C_D/σ measurements observed from consecutive test points. The mean range was established and related to the standard deviation using the procedures outlined in Ref. 4. The results for the accuracy of the thrust, drag, and torque measurements are given below.

Thrust, Drag, and Torque Accuracy

<u>Static Repeatability</u>		<u>Dynamic Repeatability</u>
Thrust	± 0.15 lb	$\pm 0.002 C_L/\sigma$
Drag	± 0.20 lb	$\pm 0.004 C_D/\sigma$
Torque	± 0.1 ft-lb	$\pm 0.003 C_Q/\sigma$

The estimated accuracies of the dynamic data which were acquired on the recording oscillograph and FM tape unit are the following:

<u>Parameter</u>	<u>Accuracy</u>
Flatwise Stress	± 200 psi
Edgewise Stress	± 200 psi
Torsional Moment	± 0.02 in.-lb
Flapping Angle	± 0.2 deg
Azimuth Reference Angle	± 2 deg
Blade Torsional Deflection	± 0.2 deg

The determination of the stall boundaries for a helicopter rotor using hot films requires a subjective rather than a quantitative interpretation of the hot-film data. A measure of the data repeatability cannot be expressed by a conventional quantitative error analysis. However, because of reasons listed below the following limits of accuracy can be placed on the hot-film data:

- (1) The azimuthal extent of stall can be determined within ± 5 deg of azimuth at a given thrust level condition.
- (2) The shaft angle at the stall threshold can be determined to the nearest $1/2$ deg (i.e., $\Delta C_L/\sigma \cong \pm 0.0025$).
- (3) The azimuthal extent of the turbulent boundary layer at a given gage location can be determined within ± 3 deg of azimuth at given thrust level conditions.

These limits on the accuracy of the subjective interpretation of the hot-film signals have been established after considering the following aspects of the data acquisition procedure:

- (1) During repeat runs at the same operating conditions, the hot-film data fell within the error bounds established above.
- (2) Two runs were made at a given operating condition to obtain data from all hot-film gages mounted on the blade. Redundant measurements obtained during these tests from the hot-film gage at the 75-percent span and 75-percent chord location were consistently within the error bounds established above.
- (3) The point of boundary layer transition can be determined more accurately than the point of boundary layer separation because of the sharp change in gage voltage measured when the boundary layer transition point moves across the hot-film gage.

EXPERIMENTAL RESULTS

The rotor configurations listed in Table I were tested in forward flight to determine the effects of blade twist, camber, taper ratio, aspect ratio, torsional frequency, and number of blades on rotor stall characteristics. The measured performance data were plotted in coefficient form (i.e., C_L/σ , C_D/σ , and C_Q/σ) versus shaft angle (α_s) for collective pitch (θ_{75}) values of 6, 9, and 12 deg and for advance ratios (μ) of 0.15, 0.30, and 0.45. The blade flapping data were reduced to half peak-to-peak ($\frac{1}{2}$ PTP) blade flapping angles for all rotor operating conditions at $\theta_{75} = 6$ deg. The limits of the geometric range of operation for the rotor shaft angle were from -16 through 12 deg. The 6- and 9-deg values of collective pitch produced reasonable rotor operation for investigating blade stall characteristics. The 6-deg pitch setting allowed an appreciable range of both stalled and unstalled conditions. The 9-deg pitch setting enabled some unstalled data to be obtained and shifted the stall boundary to more negative shaft angles where more meaningful thrust-propulsive force combinations occur. Since stall-induced blade response characteristics become more severe at a given thrust level as collective pitch is increased, some rotors were also tested at a pitch setting of 12 deg to provide data for more severe stall operation. The data for each design parameter are presented along with referenced rotor data so that the effect of the particular parameter can be compared directly. All standard-chord blades were compared to rotor number 1 (in Table I) which had untwisted, untapered blades, and with the torsional flexures locked out. The wide chord blades were compared to rotor number 5, since both had -8.4-deg twist.

It is often of interest to know the rotor tip-path-plane angle of attack at particular flight conditions. The following approximate equation may be used in conjunction with the shaft angle and blade flapping response for the particular rotor configuration of interest.

$$\alpha_{\text{TPP}} = \alpha_s + \beta_{\frac{1}{2}\text{PTP}} + \Delta\beta$$

The term $\Delta\beta$ is a rotor interference correction determined from the longitudinal flapping response for a two-bladed rotor with zero twist ($\theta_1 = 0$ deg) and a symmetrical airfoil (rotor number 1 in Table I) operating at zero collective pitch. The values of $\Delta\beta$ were determined to be 0.3, 0.5 and 0.7 deg for advance ratios of 0.15, 0.30 and 0.45, respectively. For the test results reported herein it will be shown that $\beta_{\frac{1}{2}\text{PTP}}$ is sufficiently representative of the first harmonic longitudinal flapping, a_{1s} .

ROTOR STALL CHARACTERISTICS FOR A TWO-BLADED ROTOR WITH
UNTWISTED, UNTAPERED, AND UNCAMBERED BLADES

Rotor thrust, drag, and torque coefficient to solidity ratios are plotted for rotor number 1 in Fig. 8 versus the rotor shaft angle for three collective pitch settings ($\theta_{75} = 6, 9, \text{ and } 12 \text{ deg}$). The 6-deg collective pitch setting allowed testing at shaft angles equally below and above the stall threshold; however, at higher collective pitch settings a reduced range of shaft angles was dictated due to blade stress limits.

Blade flapping, flatwise stress, edgewise stress, pitching moment, and hot film (i.e., boundary layer separation) data were obtained in conjunction with the performance data so that the stall threshold could be identified in a consistent manner from various measured quantities. These data were analyzed to identify the occurrence of the stall threshold for variations of advance ratio and collective pitch. Based on hot-film measurements which indicate flow separation at the 0.75 radial station and the 0.75 chord station, a stall threshold was established in Fig. 8 which shows the variation of the rotor lift with shaft angle. Using the rotor lift coefficient to solidity ratio indicated at the hot-film stall initiation as shown in Fig. 8, it is possible to establish the effect of collective pitch and advance ratio variations on rotor lift at the stall threshold (see Fig. 9). It was found that the lift at the stall threshold was independent of collective pitch and decreased monotonically with advance ratio.

Generally, the stall threshold indicated by hot-film data is consistent with a decrease of the rotor lift curve slope as shown in Fig. 8, especially for $\theta_{75} = 6 \text{ deg}$. This decrease of lift curve slope is usually associated with the initiation of rotor stall as indicated by results of Refs. 5 through 7. This decrease is used herein as another means to identify stall initiation. Similar to the lift, the $\frac{1}{2}$ PTP blade flapping and edgewise stress also developed a distinct increase in rate of growth with respect to increasing shaft angle. The initiation of this increase is consistently near the stall threshold indicated by hot-film data. The blade flapping results are shown in Fig. 10, and the hot-film stall threshold has been indicated as a reference. A sample of the $\frac{1}{2}$ PTP edgewise stress data is shown in Fig. 11 for $\mu = 0.3$ and $\theta_{75} = 6 \text{ deg}$. Amplification of the blade pitching moment at the first elastic torsional frequency (22P) occurred beyond the hot-film stall threshold. However, fluctuations of the amplitude of this 22P vibratory moment near the hot-film stall threshold made the determination of the threshold difficult to assess from pitching moment data. Thus, compared to the flapping and edgewise stress

data, the blade pitching moment did not represent a good indication of stall initiation. The flatwise stress indicated a more gradual transition into stall and did not appear to produce a distinct means of defining stall onset. A sample of the $\frac{1}{2}$ PTP flatwise stress for $\theta_{75} = 6$ deg and $\mu = 0.3$ is shown in Fig. 11.

Another technique was also investigated to establish the stall threshold. A plot of C_L/σ versus C_{De}/σ was made to establish rotor stall characteristics and to compare rotor efficiency with other rotor configurations. The data for rotor number 1 are shown in Fig. 12 for three advance ratios and three collective pitch values. The data trends indicate that C_{De}/σ increases more rapidly after stall initiation than C_L/σ for all advance ratios. The C_{De}/σ values also tend to have a more gradual rate of growth with increasing advance ratio after stall initiation, thus making it difficult to observe a distinct stall threshold using this method.

Thus, it may be concluded that stall initiation is distinguished from hot-film, rotor lift, blade flapping, and blade edgewise stress data. Assuming these four indicators are predicting the occurrence of or are the manifestation of the same phenomenon, then the rotor lift at the stall threshold established by each indicator should be averaged with the others. This averaging procedure has been performed for rotor number 1, and the results are shown in Fig. 13 as a function of advance ratio. The averaged results are compared to the hot-film results taken from Fig. 9 and are essentially the same boundary. Normally, one would not expect a discontinuity as sharp as the ones shown in the figures (e.g., Figs. 8, 10, 11) for rotor lift, blade flapping, and edgewise stress. Although these discontinuities could have smooth curves drawn through the data points in most instances, straight-line segments were selected to accentuate the initiation of stall as indicated by significant changes in the growth of each parameter.

EFFECT OF BLADE TWIST

Rotor number 5 of Table I has blades similar to those of rotor number 1 except for -8.4 deg of linear twist. The performance data are compared in Fig. 14 where the dashed curves for rotor 1 have been reproduced from Fig. 8. The data trends for both rotors are generally the same, and the change in rotor lift curve slope occurs at approximately the same shaft angle. Corresponding to the performance data of Fig. 14, blade flapping data are compared in Fig. 15. In addition, flapping data obtained during acquisition of hot-film data are also shown in Fig. 15 as the flagged symbols. In general, the blade flapping data trends are approximately the same for rotor numbers 1 and 5, indicating a small effect due to twist for the conditions tested.

To determine the initiation of blade stall for rotor number 5, hot-film gages were mounted at the same radial stations and chordwise positions as rotor number 1 as shown in Fig. 5. Stall threshold results determined from hot-film measurements at the 0.75R and 0.75c blade positions are shown as a slashed line on the lift performance of Fig. 14. The lift coefficient to solidity ratio at which stall initiation is defined by the hot-film measurements at 0.75R and 0.75c has been plotted versus advance ratio in Fig. 16 for $\theta_1 = 0$ and -8.4 deg. The results of Fig. 16 indicate that stall initiation for the rotor with twist occurs at a slightly lower level of lift than for rotor number 1. This would be expected, since stall normally occurs inboard on the retreating side and progresses outboard with increasing lift, and negative twist would tend to aggravate the angle-of-attack distribution. The lift at the stall threshold for both rotors decreases monotonically with advance ratio and is relatively unaffected by collective pitch.

A sample of $\frac{1}{2}$ PTP edgewise stress data is shown in Fig. 17 for rotor number 5 operating at $\theta_{75} = 6$ deg and $\mu = 0.3$. The edgewise stress for rotor number 5 demonstrates a distinct increase in rate of growth near the stall threshold indicated by the hot-film results. These are similar to the results for rotor number 1 (see previous section). Edgewise stress data acquired during hot-film data runs are also shown in Fig. 17 as flagged symbols. Although the data acquired during hot-film data runs appear to have a different rate of growth, the change in rate of growth indicates that stall initiation occurs at approximately the same shaft angle. The edgewise stress data of Fig. 11 have been reproduced in Fig. 17 as dashed lines which have been faired through rotor number 1 edgewise stress data. Comparison of the data for rotors 1 and 5 indicates that both rotors have essentially the same edgewise stress characteristics. A sample comparison of $\frac{1}{2}$ PTP flatwise stress data is also shown in Fig. 17. As expected, the effect of adding blade twist increases the $\frac{1}{2}$ PTP flatwise stress rate of growth. As shown, the flatwise stress growth rate increases after the stall threshold; however, the gradual change in growth rate from unstalled to stalled test conditions does not allow a distinct definition of stall threshold using flatwise stress data.

Thus, the change in rate of growth of rotor lift, blade flapping, and edgewise stress has been identified with the initiation of blade stall and was used in addition to the hot-film results to define stall thresholds. The average of all four indicators is presented in Fig. 18, and the results are generally similar to the hot-film results of Fig. 16. The lift and effective drag coefficient to solidity ratios for rotor number 5 are shown in Fig. 19 and compared to the rotor number 1 results reproduced from Fig. 12. These results generally indicate relatively little change in the rotor efficiency by the addition of linear twist.

For the flight conditions investigated, linear twist had an adverse effect on flatwise stress, reduced rotor lift slightly at the stall threshold, and, in general, had a negligible effect on rotor operating efficiency, blade flapping, and edgewise stress.

Sample harmonics of blade flapping for $\theta_{75} = 6$ deg have been plotted versus rotor shaft angle in Fig. 20 for rotor number 5. The flapping consists primarily of first longitudinal harmonic (a_{1s}). The second harmonic content is approximately an order of magnitude less, and lateral flapping harmonics were essentially zero (not shown). Therefore the $\frac{1}{2}$ PTP data are approximately equal to a_{1s} . Harmonic and $\frac{1}{2}$ PTP flatwise and edgewise stress data are compared in Fig. 21 for an advance ratio of 0.30. The magnitudes of the $\frac{1}{2}$ PTP and first harmonic edgewise data are different; however, the rates of increase with increasing shaft angle are approximately the same. Also, the shaft angle at which the change in rate of increase of edgewise stress occurs is approximately the same for $\frac{1}{2}$ PTP and first harmonic data.

A blade response parameter which also demonstrates a change in magnitude at blade stall initiation is the blade root pitching moment. A sample of the first harmonic amplitude of blade pitching moment is shown in Fig. 22 for the same rotor flight condition as Fig. 21. As stall initiation is approached, the first harmonic of blade pitching moment decreases in magnitude and then increases as stall is further penetrated. The data point at $\alpha_s = 8$ deg showing a reduction in magnitude is not explainable at this time.

EFFECT OF BLADE SECTION CAMBER

The forward flight performance data for the cambered airfoil rotor (number 7) are shown in Fig. 23 and compared to the performance data for the symmetrical-airfoil rotor (number 1). The results shown in Fig. 23 for rotor number 7 indicate a significant increase in C_L/σ above that of rotor 1 for the same pitch setting and flight condition. This increase of C_L/σ is attributed to the zero-lift angle (α_{0L}) of the cambered NACA 23112 airfoil which has an α_{0L} of approximately -2 deg. This value is based on the collective pitch setting required in the hover tests of Ref. 2 to obtain zero thrust.

Performance at the same nominal flight condition can be compared using Fig. 23b. For example, at $\alpha_s = -10$ deg and $C_L/\sigma = 0.085$, the cambered blades are producing about the same propulsive force (C_D/σ) but absorbing considerably less torque (C_Q/σ). The delay in stall of the cambered rotor

is clearly indicated by the difference in rotor lift curve slopes between a C_L/σ of 0.06 and 0.085. The cambered rotor slope is significantly greater. Beyond $C_L/\sigma = 0.085$, both rotors 1 and 7 are stalled and the slopes are similar. Comparing the flapping angles from Figs. 10 and 24 indicates values of 7.5 deg and 5.4 deg for the uncambered and cambered rotors, respectively. The higher flapping, or rearward tilting, of the tip-path plane of the uncambered rotor is consistent with more extensive stall. Stall initiation is indicated by the change in rate of growth of flapping.

Samples of blade $\frac{1}{2}$ PTP flatwise and edgewise stress data are shown in Fig. 25 for rotor number 7 and compared to the uncambered data (faired) reproduced from Fig. 11. The edgewise stress data indicate a distinct change in rate of growth when stall initiation occurs at $\alpha_s = -9$ deg and -6.4 deg for cambered and uncambered blades, respectively. The results of Fig. 25 were compared at the same collective pitch setting; therefore, due to the α_{OL} of the cambered blade, the lift and stress levels of the two rotors are different. Their particular lift levels can be obtained from their respective performance curves presented earlier. When compared on a lift basis, the stress levels are generally similar; however, the increase in the slope of the edgewise stress occurs at a higher lift for the cambered rotor.

The cambered rotor C_L/σ values at the stall threshold averaged from the lift, flapping, and edgewise data are presented in Fig. 45. These results demonstrate the higher lift levels achieved with the cambered rotor before stall initiation compared to the uncambered rotor. Another approach to evaluating the influence of camber is to compare performance on a lift-equivalent drag basis where the combined effects of torque and propulsive force are included in one parameter. This result is shown in Fig. 26 and the improved performance (L/D_e) of the cambered rotor is evident except at an advance ratio of 0.45, where the results are mixed.

EFFECT OF BLADE TAPER RATIO

The performance data for the tapered-blade rotor (number 8) are compared to the reference untapered rotor (number 1) data in Fig. 27. The results show that the general trends in the data are similar, the absolute levels representing the only significant difference. The higher values of lift, drag, and torque of the tapered rotor result from the greater blade area of this rotor. The chords at the 80-percent radial station are the same; however, the total blade area of the tapered blade is approximately 14 percent greater. The lift levels would be similar in hover, where the inboard area is less effective; however, the total area, rather than its distribution, is more important with increasing advance

ratio. The lift levels at the stall threshold are slightly improved for the tapered blade (which is believed related to the smaller area of the tapered blade affected by stall). For example, if the outboard 20 percent of each rotor were fully stalled, the untapered blade would experience a greater loss in lift due to its greater blade area over the outer 20 percent.

The $\frac{1}{2}$ PTP blade flapping data corresponding to the performance data of Fig. 27 for $\theta_{75} = 6$ deg are plotted versus rotor shaft angle in Fig. 28 for the three advance ratios. The data are compared to those of the untapered rotor, and the comparison indicates the same nominal rate of increase of blade flapping with increasing shaft angle for both rotors. The magnitude of blade flapping of the tapered blade rotor is approximately 0.5 deg greater and is attributed to the higher lift of this rotor. The distinct increase in the rate of growth of blade flapping is interpreted as the initiation of blade stall.

A sample of the vibratory flatwise and edgewise stresses is shown in Fig. 29. The sharp increase in rate of growth of edgewise stress is attributed to blade stall and closely corresponds to the increased flapping shown on Fig. 28. The flatwise elastic response indicated by the flatwise stress in Fig. 29 shows a general increase with shaft angle but no increase in rate at stall initiation.

The operating efficiency (L/D_e) is compared to rotor number 1 in Fig. 30. The maximum lift-to-drag ratio for the tapered rotor is greater at $\mu = 0.15$ below stall; however, at the higher advance ratios the differences are not significant. The improved low-speed performance is consistent with the hover results of Ref. 2. Below stall, or drag divergence, the tapered blade can more nearly produce uniform downwash so that all radial stations can operate at improved L/D_e 's simultaneously. This effect is less important as forward speed increases, since the inflow becomes primarily a component of the free stream.

EFFECT OF BLADE ASPECT RATIO

The independent effect of aspect ratio cannot be obtained, since blade area or number of blades must also change as a result of changing aspect ratio. Results for a wider chord blade (rotor number 9 in Table I) are presented, which represent a decrease in aspect ratio from 19.2 to 14.4 but an increase in solidity from 0.0332 to 0.0443. The blades are twisted, and therefore the test results are compared to those of rotor number 5 which has the same twist rate.

The major differences in performance, shown in Fig. 31, are in the drag and torque data. These differences are not considered an aspect ratio effect but rather a Reynolds number effect. The significantly improved drag and torque performance of the wide chord blade is believed to be related to the improved airfoil aerodynamics at the higher Reynolds number. Table III lists the Reynolds number of the test rotors at critical azimuth stations, and Ref. 8 shows that the change in the retreating blade Reynolds number between the conventional and wide chord blade can produce a significant reduction in section drag.

Since the results are influenced by the Reynolds number difference, it is impossible to draw conclusions regarding the effect of aspect ratio. For completeness, the flapping, stress, and L/D_e results are presented in Figs. 32, 33, and 34, respectively. The noticeable reduction in flapping of the wide chord blade is due in part to its lower coning angle resulting from its reduced Lock number. The L/D_e data in Fig. 34 again demonstrates the improved performance related to the higher Reynolds number of the wide chord blade.

EFFECT OF NUMBER OF BLADES

A four-bladed rotor (rotor number 6 in Table I) was tested and its performance compared to that of a two-bladed rotor to investigate the effect of number of blades. The results are shown in Fig. 35 and compared to those of a two-bladed rotor (rotor number 5) whose performance was shown in Fig. 14. As expected, the performance of the four-bladed configuration is generally similar to that of the two-bladed rotor. At the lower speed ($\mu = 0.15$) some reduction in lift is predicted due to the higher inflow caused by the increased disc loading. As forward speed is increased and the inflow becomes more proportional to the forward speed, and less dependent on the disc loading, the performance difference between the two rotors is reduced. Stall initiation is indicated by a reduction in lift curve slope and is generally similar for both rotors. Blade flapping at $\mu = 0.30$ is shown in Fig. 36, and the four-bladed rotor follows the same general trends as the two-bladed rotor. A slight reduction in flapping level is shown which is consistent with the somewhat reduced lift of the four-bladed rotor shown in Fig. 35.

The flatwise and edgewise stress data for $\theta_{75} = 6$ deg and $\mu = 0.30$ are presented in Fig. 37 and compared to two-bladed data. Below the stall threshold the stress levels are nearly identical; however, beyond the stall threshold the four-bladed stresses, both flatwise and edgewise, increase at a much sharper rate. With the data available from the test it cannot be determined why the stress levels are higher. It can only

TABLE III. MODEL ROTOR REYNOLDS NUMBER VARIATION FOR TWO VALUES OF BLADE CHORD

Rotor No.	Azimuth Position (deg)	Radial Station	Reynold's Number at		
			$\mu = 0.15$	$\mu = 0.30$	
1 (c = 1.47 in.)	90	1.00 R	0.270×10^6	0.305×10^6	0.341×10^6
		0.75 R	0.203	0.229	0.256
		0.50 R	0.135	0.153	0.170
	270	1.00 R	0.200	0.164	0.129
		0.75 R	0.149	0.123	0.097
		0.50 R	0.110	0.082	0.065
2 (c = 1.96 in.)	90	1.00 R	0.360	0.407	0.454
		0.75 R	0.270	0.305	0.341
		0.50 R	0.180	0.203	0.227
	270	1.00 R	0.266	0.219	0.172
		0.75 R	0.200	0.164	0.129
		0.50 R	0.133	0.110	0.086

be surmised that the blades of a four-bladed rotor experience greater vortex interference than those of a rotor with fewer blades and therefore respond accordingly.

The lift-equivalent drag characteristics are compared in Fig. 38; and as with the separate performance results of Fig. 35, the increase to four blades had little effect on L/D_e .

EFFECT OF BLADE TORSIONAL FREQUENCY

The reference rotor (rotor number 1) had blades which were rigidly restrained at their roots, resulting in a first elastic torsional mode frequency of 22P. The addition of a root spring produced essentially a "rigid body" torsional mode of lower frequency, its value dependent upon the spring stiffness. Three separate springs were tested producing torsional frequencies of 12P, 9P, and 5P as listed in Table I. The performance results are shown in Figs. 39, 40, and 41 and in each case compared to the reference rotor. Generally, the rotor performance data were unaffected by variations of the torsional frequency. The largest difference occurs for the lowest torsional frequency at $\theta_{75} = 9$ deg and is manifested in performance as an effective increase in collective pitch. It is doubtful this pitch change occurred at the flexure, since the spring deflection results and the $\theta_{75} = 6$ and 12 deg results did not reflect this. The change is most likely due to a slight error in setting the collective pitch. Stall initiation, as indicated by the change in rotor lift-curve slope, was essentially unaffected by torsional frequency.

A sample of the $\frac{1}{2}$ PTP blade flapping response data is shown in Fig. 42 for the rotor with the lowest torsional frequency ($\bar{\omega}_\theta = 5$). The results are compared to the corresponding flapping results for the reference rotor ($\bar{\omega}_\theta = 22$); again, no important differences are indicated.

The vibratory stress data for the rotors with torsional flexures did not change significantly from similar data for the reference rotor.

The torsional response data were examined for the presence of stall flutter, and several conditions were found which indicated typical stall flutter characteristics; that is, a first mode torsional response initiated on the retreating side and damped or reduced in amplitude on the advancing side. Such responses were observed for all torsional stiffnesses, including the fixed-root condition where the blade first elastic mode responded at 22P. Samples of the response for the torsional frequencies of 9P and 5P are presented in Fig. 43. At an advance ratio of 0.15 a typical stall flutter response is shown in Fig. 43a at $\alpha_s = -4$ deg. As

shaft angle is increased and deeper stall penetration is experienced, stall flutter conditions are exceeded and a damped impulsive-type nose-down deflection occurs. At the lower torsional frequency (Fig. 43b), larger deflections are produced and oscillations persist over wider azimuthal ranges. The typical deflections during stall flutter were about ± 0.4 deg; however, values as high as ± 2 deg were measured for highly stalled conditions as shown in Fig. 43b at $\mu = 0.30$ and $\alpha_s = -4$ deg.

It was assumed for the rotors with torsional flexures that the operating boundary was associated with either a distinct increase in vibratory torsional response or a large nose-down deflection. These indicators are summarized in Fig. 44. Also presented on this figure is the boundary for rotor number 1, which had no flexure. This boundary was determined by the response of the first elastic mode at 22P as indicated by the torsional moment gage. This boundary is coincident with the stall threshold boundary presented earlier. The most significant result shown in this figure is a reduction of C_L/σ at torsional deflection onset when the torsional frequency was increased from 9P to 12P for rotors numbers 2 and 3. Furthermore, the C_L/σ at torsional deflection onset decreased with increasing advance ratio, but the rate of decrease was not particularly dependent on torsional frequency. Also, from Fig. 44, the C_L/σ at torsional deflection onset was relatively unaffected by collective pitch. For example, the double points shown at $\mu = 0.30$ and 0.45 were obtained from data at different collective pitch settings.

SUMMARY OF STALL THRESHOLD DATA

Stall thresholds for rotors 1 and 5 were presented in Figs. 9, 13, 16 and 18. A summary of the stall threshold results for these and other rotors with rigid root restraint is presented in Fig. 45. Stall thresholds for rotors with flexible root restraint (Rotors 2, 3 and 4) are essentially equivalent to those of rotor 1.

As mentioned previously, the changes in rate of growth of rotor lift, blade flapping, and edgewise stress are associated with blade stall and have been used to establish the C_L/σ at the stall threshold. They were averaged for each rotor to define the threshold boundaries as a function of advance ratio and are shown in Fig. 45 for rotors numbers 1, 5, 6, 7, 8, and 9. The average C_L/σ of rotors numbers 1 and 5 also contain the C_L/σ at the stall threshold as determined from the hot-film results. As shown in Fig. 45, the C_L/σ decreases approximately 0.02 per 0.1 increase in advance ratio. All two-bladed rotors developed blade stall at approximately the same C_L/σ for $\mu = 0.45$. Increasing the number of blades from two (rotor number 5) to four (rotor number 6) resulted in a

decrease in C_L/σ at $\mu = 0.45$ as shown in Fig. 45. The effect of blade section camber on the C_L/σ at the stall threshold is shown by comparing the results for rotor number 7 with the results of rotor number 1. The rotor with cambered blades increased C_L/σ at the stall threshold at $\mu = 0.15$ and 0.30 by approximately 20 percent. However, camber had no noticeable effect on the stall threshold for $\mu = 0.45$. Results for rotors numbers 1 and 5 indicate that blade twist produced a negligible effect on the stall threshold. Comparing the C_L/σ for rotor number 8 with rotor number 1 in Fig. 45, the effect of blade taper is to increase the C_L/σ at the stall threshold at $\mu = 0.15$; but taper had little effect at $\mu = 0.30$ and 0.45 . Decreasing blade aspect ratio by increasing the blade chord is shown in Fig. 45 to have a negligible effect on the stall threshold; however, the results should not be definitized due to the changes in Reynolds number and Mach number which accompanied the change in aspect ratio.

BLADE BOUNDARY LAYER RESULTS

Hot-film data obtained at experimental conditions listed in Table II have been analyzed to determine the extent of laminar, turbulent, transitional, and separated flow on the rotor blade surface. Azimuth angles at which boundary layer transition and separation (stall) were indicated by the hot-film signals have been tabulated for each hot-film gage throughout the thrust level range tested. Data are presented in this section to show the variation of the onset and azimuthal extent of stall as a function of thrust level, collective pitch, advance ratio, and location of the hot-film gages on the blade. The position of the boundary layer transition point and the azimuthal extent of the turbulent boundary layer as a function of thrust level and spanwise position on the blade are also presented. Finally, the boundary layer transition and separation data are compared to provide a better understanding of the boundary layer conditions leading to stall onset. Results are shown for rotors with untwisted and twisted blades.

Determination of Boundary Layer Transition and Separation Indicators Using Hot-Film Gages

Prior to the wind tunnel tests an experimental study was conducted to determine the qualitative effects of helicopter rotor stall on the electrical output signals from hot-film gages flush mounted on the blade suction surface. An NACA 0012 airfoil with 2-in. chord was mounted in the low-speed 3- x 3-in. calibration tunnel, as shown in Fig. 46. The desired free-stream turbulence level in the calibration tunnel was established by placing a turbulence generating grid upstream from the airfoil. The turbulence levels generated by the grids were measured with

a hot-wire anemometer, as shown below:

<u>Configuration</u>	<u>Turbulence Level</u>
No grid	0.7%
1/4" grid	2.5%
1/2" grid	8.0%

A thin film of oil was applied to the airfoil surface to indicate the locations of boundary layer transition and separation on the blade. Results of the oil-film flow visualization studies for the 1/4-in. grid configuration are summarized in Fig. 47. Regions of boundary layer transition and separation were easily discernible in the oil-film patterns on the blade surface for each angle-of-attack setting of the airfoil.

Following the oil-film flow visualization tests, an NACA 0012 airfoil was tested in the calibration tunnel with two hot-film gages mounted on the blade suction surface. One gage was mounted at the airfoil midchord and the second was located near the trailing edge. Both the mean and the fluctuating components of the hot-film output voltage were measured at each angle-of-attack setting of the airfoil. Figure 48 shows the mean and rms voltage fluctuation from the hot-film gages versus angle of attack for the 1/4-in. grid configuration tests.

Figures 47 and 48 were compared to obtain the basis for a qualitative evaluation of helicopter stall. When the boundary layer transition point moved upstream across the hot-film gage as the angle of attack was increased, both the mean component and the fluctuating component of the hot-film voltage output increased. The rise in the mean voltage was attributed to the increased heat transfer to the turbulent boundary layer. The turbulence increase downstream from the transition point caused the elevated fluctuating voltage. As the boundary layer separation point moved across the hot-film gage in the upstream direction, the fluctuating voltage increased but the mean voltage decreased. These results are caused by the increased turbulence in the separation region and the reduced heat transfer capability of the separated boundary layer.

To determine whether the turbulence levels established in the oil-film flow visualization tests were typical of turbulence levels encountered in model helicopter rotor testing in the UAC 4- x 6-ft subsonic wind tunnel, measurements were taken with a hot-wire anemometer to determine the free-

stream turbulence level in the tunnel. The turbulence level was found to be 0.52% for $U_\infty = 50$ ft/sec and 0.43% for $U_\infty = 100$ ft/sec. However, the turbulence level in the rotor coordinate system depends upon the total velocity vector encountered by the rotating blade. The free-stream turbulence level sensed by the moving rotor blade will be decreased when the blade is advancing and increased when it is retreating. Thus, the turbulence levels encountered in helicopter rotor testing in the UAC 4- x 6-ft subsonic wind tunnel were expected to be within the turbulence level range investigated in the no-grid and 1/4-in. grid calibration tests.

For the model rotor tests conducted in the UAC 4- x 6-ft wind tunnel, reduction of the hot-film data requires a subjective interpretation of Visicorder analog traces and oscilloscope photographs of hot-film output signals. The following criteria were established to relate qualitative changes in the hot-film output signal to boundary layer separation and transition on the blade surface:

- (1) Boundary layer separation - large amplitude fluctuations in the gage voltage at frequencies above 1 KHz generally accompanied by a decrease in the mean level of the hot-film signal.
- (2a) Boundary layer transition (laminar to turbulent) - sharp increase in the hot-film output voltage when the transition point moves upstream across the hot-film gage.
- (2b) Boundary layer transition (turbulent to laminar) - sharp decrease in the hot-film output voltage when the transition point moves downstream past the hot-film gage.
- (3) Stall threshold (initiation) - boundary layer separation observed at the blade trailing edge for approximately 10% of the azimuth.
- (4) Stall onset - the azimuth position at which the boundary layer at a given gage location separates from the blade surface.
- (5) Stall recovery - the azimuth position at which the boundary layer at a given gage location reattaches to the blade surface.

The application of these criteria in the data reduction procedure is illustrated in Fig. 49. In this figure a series of oscilloscope photographs are presented for a typical test depicting the change in the characteristics of the hot-film signals as the rotor thrust level (lift) is increased. The test was for the rotor having twisted blades operating at a collective pitch of 6 deg and an advance ratio of 0.30. The hot-film gages were located at 85-percent span and at 5-, 15-, 25-, and 75-percent chord.

In Fig. 49a the rotor was operating at a low thrust level and was unstalled. The sinusoidal pattern of the hot-film signals was caused by the change in the local free-stream velocity vector at each gage location as the rotor moved through one complete revolution. As the rotor blade advanced, the heat flux rate from a hot-film gage increased in proportion to the increase in the local free-stream velocity relative to the rotor blade at the gage location, until it reached a maximum near $\psi = 90$ deg. As the blade moved toward the retreating side the hot-film gage voltage decreased in proportion to the relative free-stream velocity until a minimum was reached near $\psi = 270$ deg (see Fig. 6).

Although it cannot be determined from viewing the analog traces in Fig. 49a independently, the 5-, 15-, and 25-percent chord gages were within the laminar region of the boundary layer on the blade surface over the entire 360-deg azimuth, whereas the 75-percent chord gage was within the turbulent region of the boundary layer throughout. This pattern was common for hot-film runs at low thrust levels. The presence of a laminar or turbulent boundary layer at the gage location was determined by references to the DC voltage levels of the hot-film gages. The heat flux from a hot-film gage to a turbulent boundary layer at the 75-percent chord location is approximately twice as large as the heat flux to a laminar boundary layer at the same location. A second check to indicate whether the boundary layer is laminar rather than turbulent at the gage location requires the measurement of the degree of turbulence indicated in the hot-film signal. This technique was judged impractical for hot-film measurements of rotor blade boundary layers for three reasons: (1) the scale of turbulence in the boundary layer is extremely fine, having a characteristic frequency in excess of 5 KHz which is near the upper frequency limit of the hot-film gages; (2) the hot-film gage located on the blade surface within the turbulent boundary layer is in direct contact with the laminar sublayer which acts as a buffer against the fluctuations in the turbulent boundary layer, thus, reducing the intensity of the turbulent fluctuations at the blade surface; (3) electronic noise generated in the slip rings tends to mask the differences between the laminar and turbulent signals.

As the thrust level was increased (Fig. 49b), the boundary layer transition point moved upstream to the 25-percent chord location at $\psi = 170$ deg, as indicated by the sharp rise in the hot-film signal. At $\psi = 200$ deg the hot-film signal at the 25-percent chord location reached a plateau, indicating that the transition point had moved completely upstream of the 25-percent chord location. At $\psi = 230$ deg the transition point had moved further forward on the blade surface to the 15-percent chord location where it remained until $\psi = 255$ deg when it began to return to the blade trailing edge. At $\psi = 280$ deg the boundary layer at the 25-percent

chord location returned to the laminar condition which it retained until $\psi = 170$ deg during the next revolution of the rotor.

As the thrust level was increased to $C_T/\sigma = 0.065$, Fig. 49c and 49d indicate that the mean position of the boundary layer transition point continued to move toward the leading edge of the blade. The azimuthal extent of turbulence at the 25-percent chord location increased to 175 deg. The 15-percent chord location was fully turbulent for 105 deg of azimuth and the transition point had moved forward on the blade surface to the 5-percent chord location at $\psi = 205$ deg.

In Fig. 49e, the large amplitude, high frequency fluctuations characteristic of turbulent boundary layer separation appear on all four hot-film analog traces. (Note that the oscilloscope sensitivity for the 75-percent chord gage was reduced inadvertently by a factor of 2, thus reducing the apparent magnitude of fluctuations for that gage.) The rotor blade was mildly stalled over 1/6 of the revolution, with stall onset at $\psi = 260$ deg and stall recovery occurring at $\psi = 320$ deg. Thus, within a shaft angle range of 2 deg the boundary layer separated from the entire suction surface of the blade at the 85-percent spanwise location. At the azimuth for stall onset the boundary layer at the 15-, 25-, and 75-percent chord locations was turbulent and at the 5-percent chord location the boundary layer was transitional. Separation occurred at all gage locations within the azimuthal extent of the turbulent boundary layer.

The degree of subjectivity inherent in the data reduction procedure is illustrated in the interpretation of the cause of the fluctuations in the hot-film gage signal at the 25-percent chord location within the azimuth range $320 \text{ deg} \leq \psi \leq 360 \text{ deg}$. One interpretation is that the fluctuations in output signal were caused by chordwise oscillations in the location of the transition point on the blade surface which caused the gage heat flux to fluctuate between laminar and turbulent levels. However, it could be argued that the signal fluctuations were caused by an extended region of stall because the large amplitude, high frequency fluctuations are characteristic of boundary layer separation. The first interpretation of the hot-film signals has been chosen for this special case because the second interpretation is inconsistent with the stall boundaries taken at other gage locations and operating conditions.

As the thrust level was increased further, both the azimuthal extent of the turbulent boundary layer and the region of boundary layer separation increased as shown in Figs. 49f through 49h. The mean position of the boundary layer transition point moved closer to the blade leading edge, causing the boundary layer at the 5-percent chord location to become

completely turbulent before the onset of boundary layer separation as shown in Fig. 49f.

When the rotor was severely stalled at a high thrust level condition (Fig. 49h), stall onset occurred at $\psi = 185$ deg, 190 deg, and 192 deg at the 5-, 15-, and 25-percent gage locations, respectively. Thus, it appears that when the rotor was severely stalled the initiation of boundary layer separation occurred at the blade leading edge and moved quickly toward the blade trailing edge. The cause of this phenomenon is thought to be a vortex which is shed from the blade leading edge at high angles of attack and swept back along the blade surface, initiating boundary layer separation along the entire blade chord.

Boundary Layer Separation Results (Stall)

Effect of Thrust on Boundary Layer Separation

The effect of the rotor thrust level (lift) on the location and azimuthal extent of boundary layer separation is clearly depicted in Fig. 50, which shows a series of oscilloscope traces of hot-film signals for an uncambered, untapered rotor having -8.4 deg of linear twist operating at a tip speed of 300 ft/sec, a collective pitch of 6 deg, and an advance ratio of 0.30. The analog voltage traces for eleven hot-film gages mounted on the blade suction surface are presented at four rotor shaft angles within a narrow thrust level range in which the rotor went from unstalled operation ($C_L/\sigma = 0.065$) to a severe stall condition ($C_L/\sigma = 0.079$). The hot-film analog traces have been positioned in Fig. 50 to correspond to their approximate locations on the blade surface.

At a shaft angle of -9 deg ($C_L/\sigma = 0.065$) the rotor was unstalled over the entire portion of the blade instrumented with hot-film gages (Fig. 50a). The 75-percent chord location was completely turbulent at 75-, 85-, and 95-percent span at all azimuth angles, whereas the 15-, 25-, and 50-percent chord gages fluctuated between laminar and turbulent flow and the gage near the leading edge at 5-percent chord, 85-percent span was laminar throughout 360 deg of azimuth. Small fluctuations characteristic of incipient boundary layer separation are apparent at $\psi = 295$ deg at the 75-percent chord, 75-percent span location.

Increasing the shaft angle by 1 degree (Fig. 50b) caused the rotor to undergo mild stall indicated by boundary layer separation at the 75- and 85-percent spanwise locations. At 75-percent span the

boundary layer separation region moved quickly forward from the trailing edge, where it originated, to the 25-percent chord location while at 85-percent span the separated region moved forward to the 50-percent chord over a limited azimuthal range. Thus, at moderate thrust levels stall is initiated at the blade trailing edge and propagates forward to the blade leading edge essentially instantaneously.

Another 1 deg increase in shaft angle (Fig. 50c) to $\alpha_s = -7$ deg ($C_L/\sigma = 0.076$) caused the stall to increase in severity. Boundary layer separation extended over the entire blade chord at 85-percent span, although at 95-percent span the boundary layer continued to remain attached at all azimuth angles. Finally, at $C_L/\sigma = 0.079$ (Fig. 50d) the separated region moved radially outward to 95-percent span to include the entire region of the blade instrumented by the hot-film gages.

The data from Fig. 50 have been supplemented with additional data from Visicorder analog traces to provide a map in Fig. 51 of the azimuthal and spanwise variations of stall with increasing rotor thrust level (lift). As shown, stall was initiated on the retreating side of the rotor at an azimuth position of approximately 300 deg. The azimuth for stall onset occurred progressively earlier with increased thrust until it approached the advancing side at the leading edge ($\psi = 180$ deg) of the rotor disc, whereupon the rate of progression decreased significantly. The azimuth for stall recovery progressed from 300 deg forward to 20 deg with increasing thrust, whereupon the rate of progression slowed considerably.

Effect of Spanwise Position on Boundary Layer Separation

Figures 50 and 51 show clearly that stall was initiated at the 75-percent span and progressed radially outward to the 95-percent span as the thrust level increased for the twisted blade rotor at a collective pitch of 6 deg and an advance ratio of 0.30. Figure 52 illustrates the spanwise variations in stall boundaries at the 75-percent chord for the same conditions. The azimuthal extent of stall at each thrust level varies inversely with radial extent on the blade. At high thrust levels the stall boundaries coalesced as the boundary layer separation spread uniformly over the blade surface.

The spanwise variation in stall boundaries for the untwisted blade is shown in Fig. 53. Stall onset occurred simultaneously at 75- and 85-percent span on the retreating blade ($\psi = 295$ deg) at $C_L/\sigma = 0.066$.

The 95-percent span remained unstalled until $C_L/\sigma = 0.073$. Although some variation existed in the boundary for stall onset, stall recovery occurred almost uniformly across the span at all thrust levels.

Chordwise Extent of Boundary Layer Separation

The chordwise variations in the onset and azimuthal extent of boundary layer separation at 75-percent span are presented in Fig. 54, which includes data from the hot-film oscilloscope traces in Fig. 49 supplemented with data from Visicorder analog traces. At $C_L/\sigma = 0.068$, boundary layer separation was initiated at 75-percent chord for the azimuth range $294 \text{ deg} \leq \psi \leq 322 \text{ deg}$. At a slightly higher thrust level, $C_L/\sigma = 0.072$, the boundaries for stall onset for 25-, 50-, and 75-percent chord are identical. Thus, stall, which was initiated at the blade trailing edge, propagated forward to the blade leading edge over a very narrow thrust range. As thrust level was increased further to $C_L/\sigma = 0.100$, the boundary for stall onset remained independent of chord, but chordwise variations in the stall recovery boundary were evident; the 25-percent chord location recovered from stall at $\psi = 0 \text{ deg}$, followed by the 50-percent chord location at $\psi = 8 \text{ deg}$ and the 75-percent chord location at $\psi = 16 \text{ deg}$. At very high thrust levels, $C_L/\sigma = 0.120$, stall onset occurred at 25-percent chord at $\psi = 175 \text{ deg}$ followed by the 50-percent chord at $\psi = 178 \text{ deg}$ and the 75-percent chord at $\psi = 190 \text{ deg}$. This initiation of stall at the blade leading edge is presumably caused by a vortex shed from the leading edge at high angles of attack. Data at 85- and 95- percent span substantiated the conclusions drawn from the 75-percent span data.

Effect of Collective Pitch on Boundary Layer Separation

Figures 55 and 56 present data obtained at all three collective pitch settings for rotors 1 and 5, respectively, operating at an advance ratio of 0.30. Points of onset and recovery of boundary layer separation have been plotted at each thrust level tested. The variations in the azimuthal extent of stall at a given thrust level are generally within the range of data repeatability which has been estimated to be $\pm 5 \text{ deg}$ of azimuth. Thus, although each rotor thrust level is the product of a unique combination of rotor shaft angle and collective pitch setting, the azimuthal extent of stall is dependent only on rotor thrust level. Increasing rotor thrust either by increasing the rotor shaft angle or the collective pitch setting produces a corresponding enlargement in the azimuthal extent of stall. Data obtained at advance ratios of 0.15 and 0.45 substantiate the conclusions drawn from the data for $\mu = 0.30$.

Effect of Advance Ratio on Boundary Layer Separation

Figures 57 and 58 present data obtained at all three advance ratios for rotors 1 and 5, respectively, operating at a collective pitch of 6 deg. As shown in Fig. 57, stall was initiated on the retreating blade of rotor 1 at approximately the same azimuth ($\psi = 285$ deg) for each advance ratio. Stall thresholds occurred at $C_{T1}/\sigma = 0.092$, 0.065, and 0.055 for the advance ratios of 0.15, 0.30, and 0.45, respectively. The stall boundaries for each advance ratio were similar in shape but shifted in thrust level.

For rotor 5 (Fig. 58) with -8.4-deg twist, stall also was initiated on the retreating blade although at different azimuths for each advance ratio. The azimuth positions for stall threshold were $\psi = 275$, 305, and 260 deg for $C_{T1}/\sigma = 0.087$, 0.068, and 0.060 at $\mu = 0.15$, 0.30, and 0.45, respectively. The stall boundaries for advance ratios of 0.15 and 0.30 are similar in shape but shifted in thrust level. For $\mu = 0.45$, the stall onset boundary was similar to stall onset boundaries for $\mu = 0.15$ and 0.30, although shifted in thrust level, whereas stall recovery occurred much earlier in the azimuth within the thrust level range $0.060 \leq C_{T1}/\sigma \leq 0.090$.

From the above data the following generalizations concerning the effect of advance ratio on stall can be made for both the twisted and untwisted blades: (1) the thrust level for the stall threshold decreases with advance ratio; (2) the stall boundaries for advance ratios 0.15, 0.30, and 0.45 are generally similar except for a shift in thrust level; and (3) at a given thrust level the azimuthal extent of stall increases with advance ratio.

Boundary Layer Transition Results

Data from the hot-film gages have been analyzed to determine the effect of azimuth position, thrust, collective pitch, advance ratio, and blade twist on the location of boundary layer transition on the rotor blade suction surface. Azimuth position and thrust level were the parameters which primarily influenced boundary layer transition, whereas for a given thrust level, the effects of collective pitch, advance ratio, and blade twist were secondary.

Effect of Thrust on Boundary Layer Transition

The effect of increasing thrust level on the characteristics of the suction surface boundary layer is shown in Fig. 59. The azimuthal extent of the laminar and turbulent boundary layer at the 25-percent

chord on the suction surface is presented for rotor 5 operating with a collective pitch of 6 deg and an advance ratio of 0.30. For all thrust level conditions tested, the boundary layer was predominantly turbulent on the retreating blade. As the thrust level was raised by increasing the rotor shaft angle, the local angle of attack at each azimuth position was increased accordingly, causing the mean position of the transition point to shift toward the leading edge. Thus, the 25-percent chord location became turbulent earlier in the azimuth. At $C_T/\sigma = 0.08$ the 25-percent chord location was turbulent over 75-percent of the azimuth, and at much higher thrust, $C_T/\sigma = 0.120$, the boundary layer was laminar over only a small region centered about $\psi = 90$ deg.

This growth of the azimuthal extent of the turbulent boundary layer with increasing thrust level was typical for all conditions tested.

Effect of Azimuth Position on Chordwise Location of Transition Point

The location of the boundary layer transition point at a given spanwise location can be inferred from a series of hot-film gages positioned along the chord at that span. In Fig. 60 the chordwise movement in the boundary layer transition point at 85-percent span has been inferred from the data in Fig. 49. On the advancing blade the transition point was located between the 50- and 75-percent chord location. At $\psi = 150$ deg the transition point moved forward rapidly toward the leading edge, where it remained until the blade reached the advancing side of the azimuth, whereupon the transition point returned quickly to the 60- to 70-percent chord location.

This movement of the transition point was typical for all conditions at which hot-film data were obtained. The flow was turbulent over the entire azimuth at the 75-percent chord. At 25- and 50-percent chord the flow was predominantly turbulent on the retreating side and laminar on the advancing side. However, for the data presented in Fig. 60, the Reynolds numbers (see Table III) were 230,000 and 123,000 at $\psi = 90$ and 270 deg, respectively. Thus, from Reynolds number considerations alone, transition point movement opposite that presented in Fig. 60 should be expected. However, the variation in blade angle of attack around the azimuth produced the dominant influence on boundary layer transition, as shown in Fig. 47 where a 5 deg change in the blade angle of attack caused the transition point to move from the trailing edge to the 25-percent chord location. For the data in Fig. 60 the change in blade angle of attack between $\psi = 90$ and 270

deg was estimated to be 6 deg, which caused the boundary layer on the retreating blade to be predominantly turbulent and the advancing blade to be laminar, contrary to expectations based on Reynolds number considerations alone.

Comparison of Boundary Layer Separation and Transition Results

The boundary layer transition and separation data have been compared to determine the characteristics of the blade boundary layer at stall onset. In Fig. 61, transition and stall boundaries for rotor 5 have been plotted as a function of rotor thrust level for the 25-percent chord, 85-percent span location from the data in Fig. 49. For $C_{I}/\sigma < 0.036$, flow at the 25-percent chord location was laminar throughout the azimuth. At $C_{I}/\sigma > 0.039$, the flow became turbulent on the retreating blade near $\psi = 220$ deg. As the thrust level was increased further the azimuthal extent of the turbulent boundary layer increased rapidly until it reached the advancing side of the azimuth where the rate of progression slowed considerably. At $C_{I}/\sigma = 0.070$, the stall threshold was reached and turbulent boundary layer separation occurred. As the thrust level was increased further the azimuthal extent of both the turbulent and stalled regions expanded but stall always remained within the turbulent region.

The data in Fig. 61 are typical of results obtained at all operating conditions. No regions of laminar separation were observed throughout the test program even though hot-film gages were located on the suction surface near the leading edge at 5-percent chord. It is recognized, however, that because of the finite active area of the hot-film gage (0.060 in. chordwise x 0.100 in. spanwise) small separation bubbles may affect the heat transfer rate from the gage by only a negligible amount and be undetectable by the hot-film technique.

CONCLUSIONS

The following conclusions concerning helicopter rotor stall are based upon model rotor performance and blade response data obtained for rotors with flapping freedom but no lag freedom or cyclic pitch and operating at low Mach and Reynolds numbers.

1. The rotor lift at blade stall threshold indicated by flow separation (hot-film measurements for rotors 1 and 5) was generally coincident with a change in rate of growth of C_L/σ , blade flapping, and vibratory edgewise stress with increasing shaft angle.
2. Based on the average stall threshold indicated by flow separation, rotor lift curve slope, flapping, and edgewise stress data, C_L/σ at stall threshold decreases approximately 0.02 for each 0.1 increase in advance ratio. All two-bladed rotors experienced stall at approximately the same C_L/σ for $\mu = 0.45$. Increasing the number of blades from two to four resulted in a decrease in C_L/σ at $\mu = 0.45$.
3. Blades with cambered sections increased C_L/σ at the stall threshold at $\mu = 0.15$ and 0.30 by approximately 20 percent. At $\mu = 0.45$, stall occurred at approximately the same C_L/σ for cambered and uncambered blades.
4. No significant effects on stall threshold were measured by increasing blade twist from zero to -8.4 deg.
5. Blade taper increased C_L/σ at stall threshold at $\mu = 0.15$ but had little effect at $\mu = 0.30$ and 0.45 .
6. At the conditions investigated, the effect of decreasing aspect ratio (by increasing chord) had a major influence on Reynolds number and Lock number and therefore could not be separately assessed.
7. Comparison of the rotor performance relative to data for a reference rotor on a lift-effective drag ratio basis indicates the following:
 - a. Decreasing aspect ratio by increasing blade chord produced a significant increase in rotor efficiency (L/D_e); however, this increase is believed to be primarily related to the reduction in airfoil drag due to an increase in Reynolds number.

- b. Blade-section camber does not appreciably affect $(L/D_e)_{\max}$; however, it does allow operation at higher C_T/σ at $(L/D_e)_{\max}$ due to delay of stall onset. This improvement was evident at $\mu = 0.15$ and 0.30 but not at $\mu = 0.45$.
 - c. Blade taper produced a small increase in L/D_e at $\mu = 0.15$ and 0.30 , but was ineffective at $\mu = 0.45$.
 - d. Blade twist of -8.4 deg and increasing the number of blades from two to four had negligible effect on L/D_e .
8. The C_T/σ at the onset of blade torsional oscillations decreased with increasing advance ratio similarly to the decrease in C_T/σ due to stall. Blade torsional frequency had negligible effect on the stall threshold.
9. Stall-flutter-type responses were measured at the stall threshold, but impulsive-type nose-down deflections were measured under deeper stall conditions.
10. Trends in the rate of growth of blade flatwise and edgewise bending stresses with increasing rotor lift by increasing shaft angle indicate:
- a. Blade twist induced a more rapid growth of flatwise bending stress with no effect on edgewise stress.
 - b. Blades with airfoil camber had little effect on the growth of flatwise and edgewise stresses.
 - c. Blades with taper lowered the flatwise and edgewise stress growth rate.
 - d. Corresponding to the lower rate of growth of flapping for a blade with lower aspect ratio, the flatwise and edgewise stresses grow at a lower rate.
 - e. Beyond the stall threshold, increasing the number of blades from two to four caused the flatwise and edgewise bending stresses to develop at a higher rate.
 - f. Decreasing aspect ratio significantly affected Lock number, and therefore its influence on stress could not be separately assessed.

The following conclusions specifically relate to the results of the hot-film measurements taken over the outer 25 percent of the blade:

1. Hot-film gage measurements consistently indicated the location of the stall and the laminar/turbulent transition of the boundary layer azimuthwise, chordwise, and spanwise.
2. Stall (flow separation) is indicated by large amplitude high frequency fluctuations in the anemometer voltage versus time (azimuth) trace. Boundary layer transition is indicated by a rapid change in the voltage level -- high voltage level indicates turbulent flow; low voltage level indicates laminar flow.
3. Stall was generally initiated on the retreating side of the rotor at an azimuth of approximately 300 deg.
4. The azimuth for stall onset progressed rapidly from 300 deg back to 180 deg with increased thrust level, whereupon the rate of progression decreased significantly. The azimuth for stall recovery progressed from 300 deg forward to 200 deg with increasing thrust level.
5. Stall progressed radially outward from 75% R to 95% R.
6. At moderate thrust levels stall is initiated at the blade trailing edge and propagates forward to the blade leading edge essentially instantaneously. At high thrust levels and severe stall conditions, stall is initiated at the blade leading edge, which is presumably attributable to a leading edge vortex.
7. At a given advance ratio, stall and transition boundaries are mainly dependent on thrust level and generally independent of the collective pitch and shaft angle combination used to establish a given thrust level.
8. Stall initiation is nearly independent of blade linear twist. At advance ratios of 0.15 and 0.30 the twisted blade stalled at a slightly lower thrust level than the untwisted blade, whereas at an advance ratio of 0.45 no effect of twist was observed.
9. The thrust level for stall initiation decreases with advance ratio.
10. The flow is turbulent over the entire azimuth at the 75-percent chord. At 25- and 50-percent chord the flow is predominantly turbulent on the retreating side and laminar on the advancing side.

11. The transition boundaries are similar in character to those for stall and are generally independent of twist.

12. Stall onset and recovery occurs within the azimuthal region for turbulence.

RECOMMENDATIONS

The following research tasks are recommended as a result of specific findings and/or limitations of this investigation.

1. Theoretical studies should be conducted to compare with the experimental data contained herein to assess the accuracy of various theories in predicting performance and stall effects.
2. Additional tests should be performed to investigate the effects of cyclic pitch, blade flexibility, and blade root restraint (i.e., teetering, hingeless, or articulated) on stall characteristics. Also, more extensive hot-film data and flow visualization data should be acquired to enhance the understanding of stall phenomena and provide wake data for analytical methods.
3. Low Reynolds number airfoil data, both steady and unsteady, should be obtained for incorporating in analytical methods to be used for comparing with test results.
4. Sufficient rotor tests should be conducted to evaluate the effects of higher Reynolds number and Mach number on the conclusions reported herein. The limited results obtained at somewhat higher Reynolds number than the main body of data implied a significant effect on performance. A further increase should be tested as well as possible combinations of higher Reynolds number and other design parameters. The validation of the conclusions reached herein at higher Reynolds number, above the sensitive range at which the present tests were conducted, would provide additional confidence in applying the results to full-scale rotors.

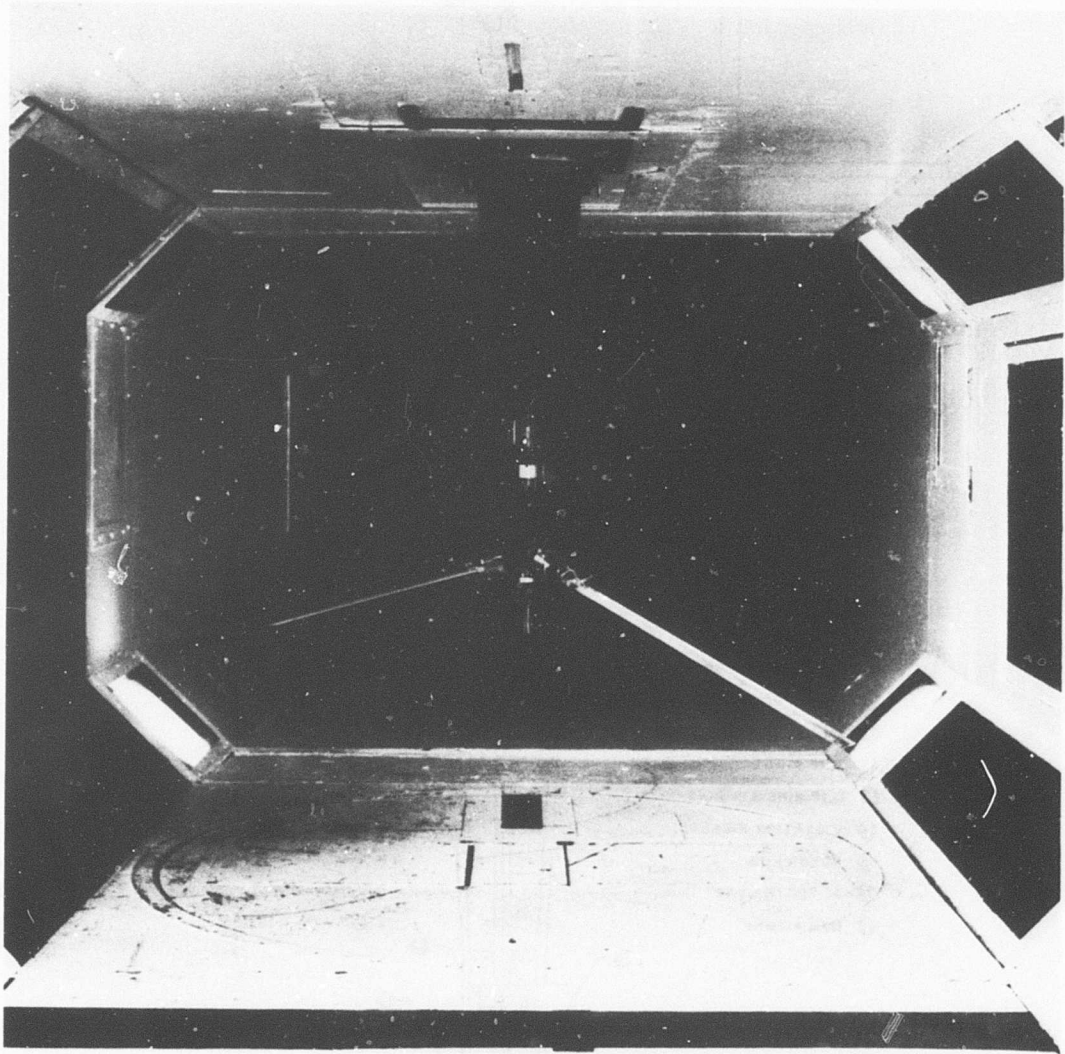


Figure 1. Model Rotor Test Rig in Wind Tunnel.

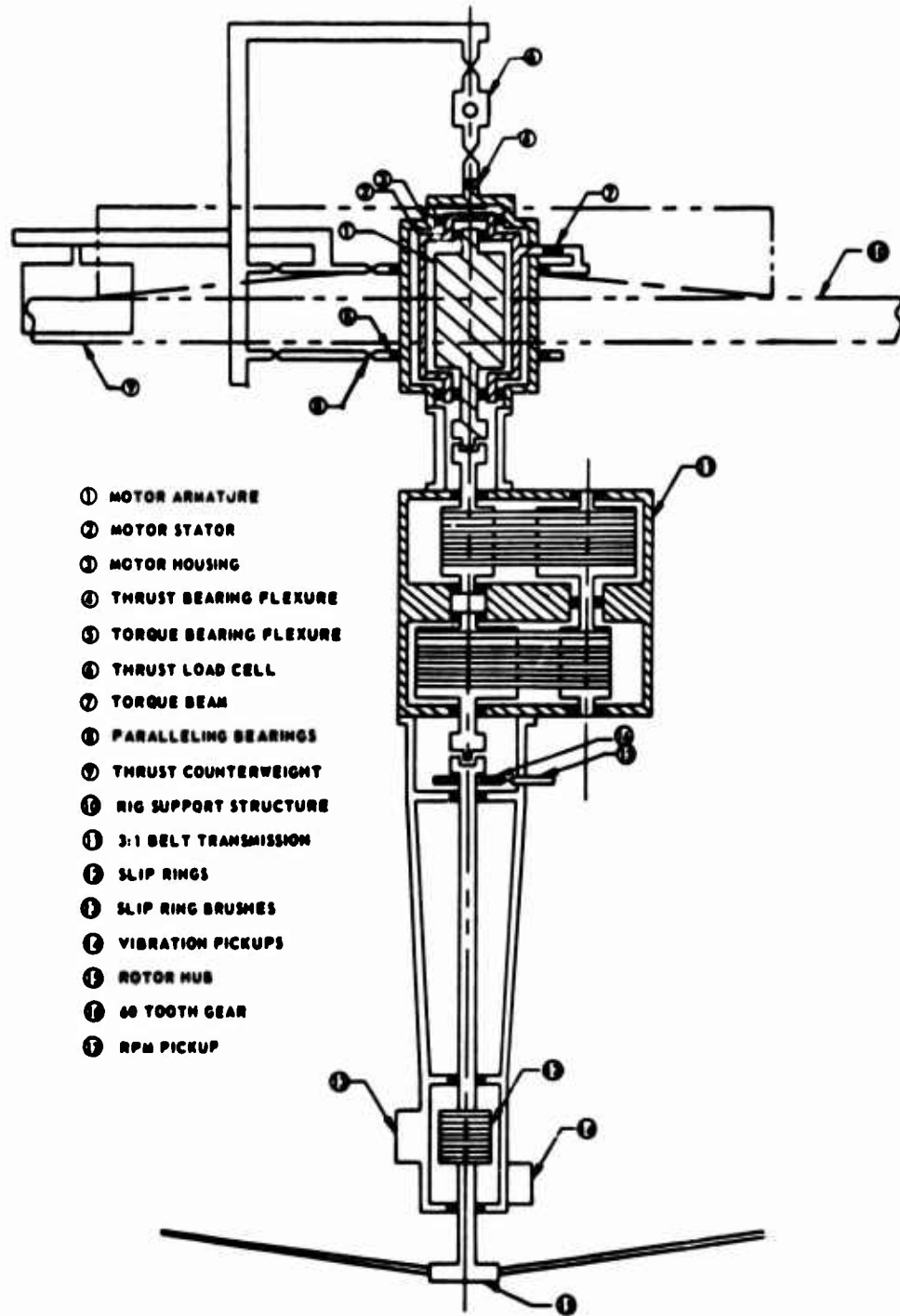


Figure 2. Schematic Cross Section of Rotor Test Rig.

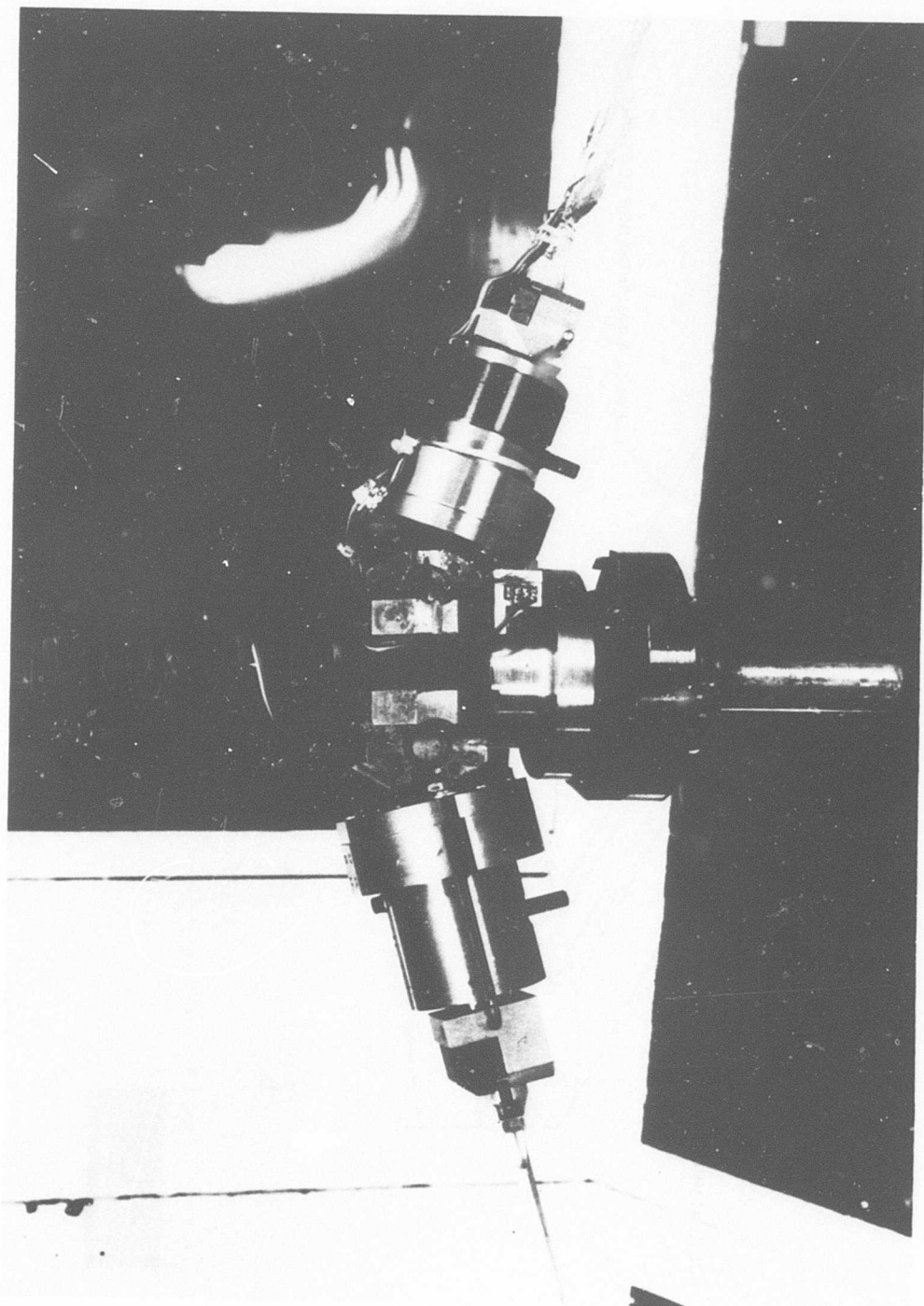


Figure 3. Model Rotor Hub Region.

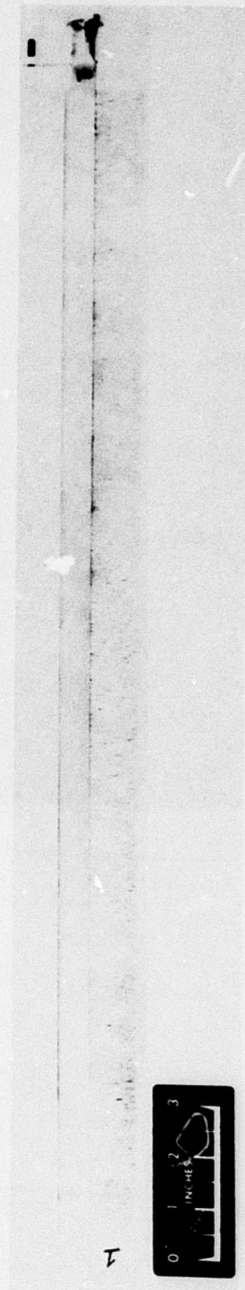
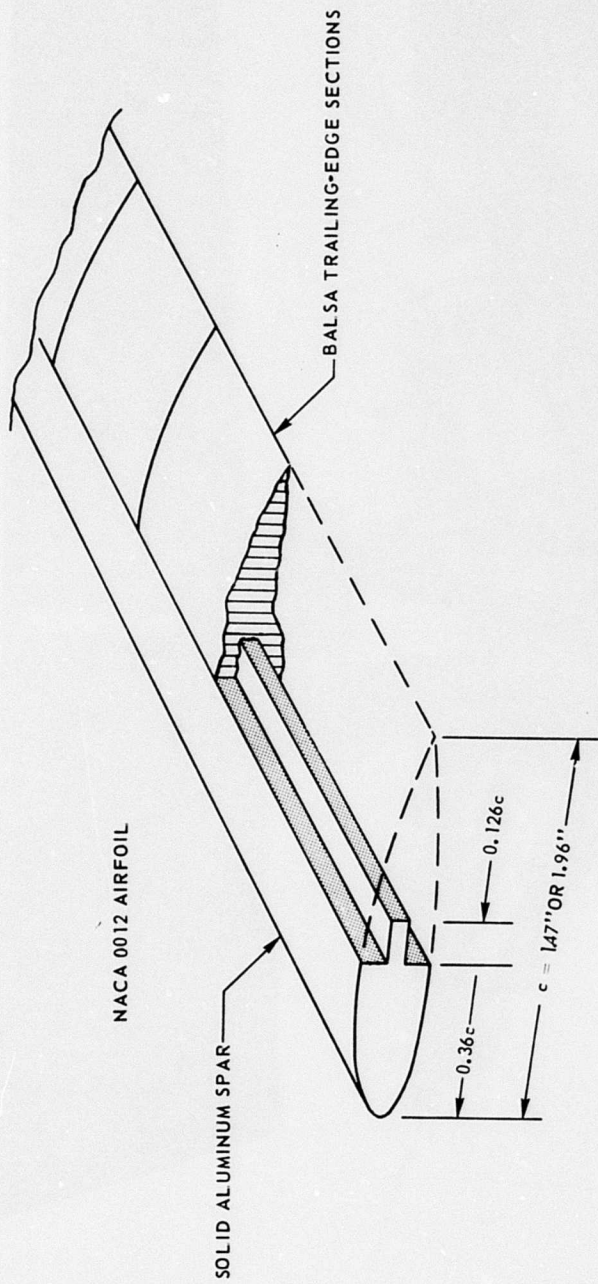
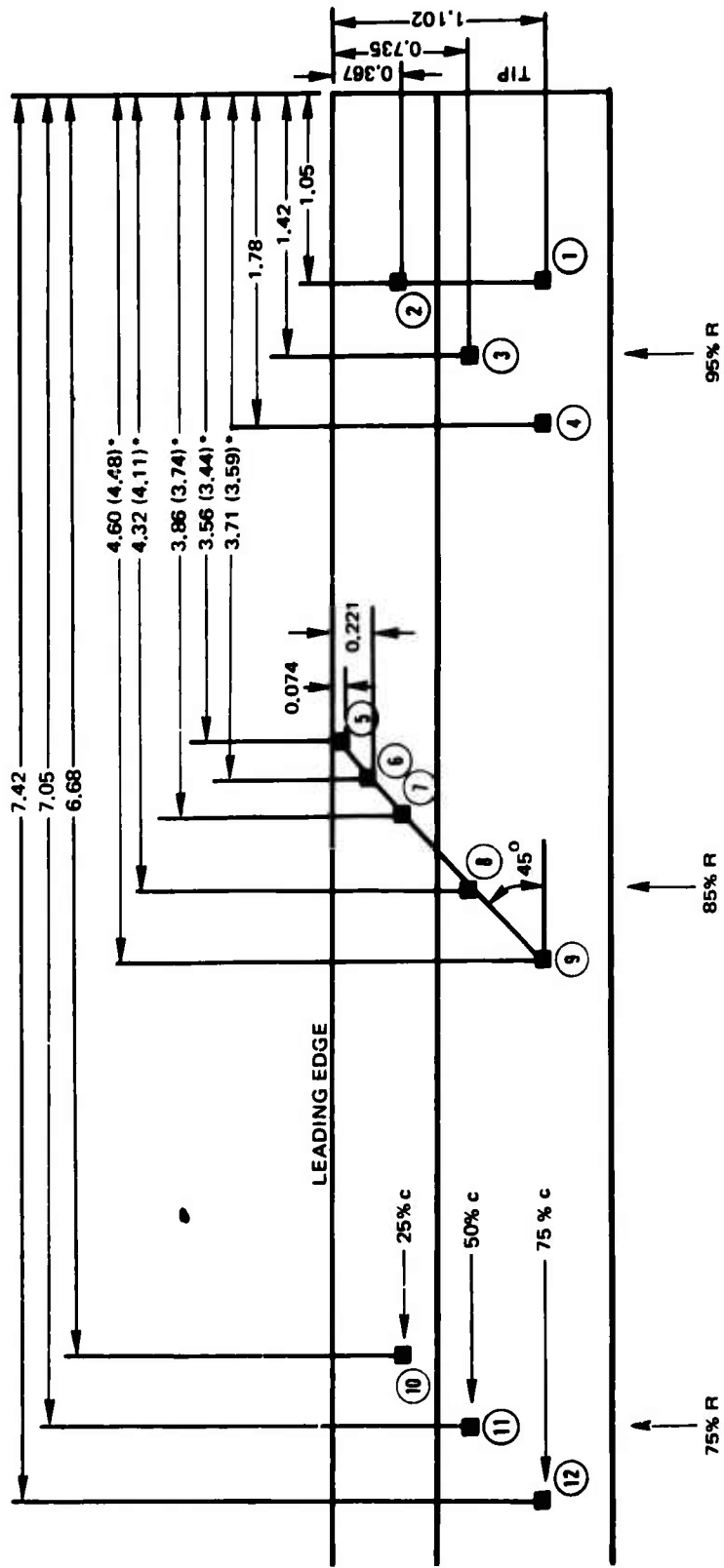


Figure 4. Schematic of Model Rotor Blade Construction.

RADIUS, R = 28,165 in. = 2,347 ft
 CHORD, c = 1,47 in.



ALL DIMENSIONS IN INCHES

*GAGE LOCATIONS FOR ROTOR 1 AT 85% SPAN

Figure 5. Schematic of Hot-Film Gage Locations on Blade Suction Surface for Rotors Numbers 1 and 5.

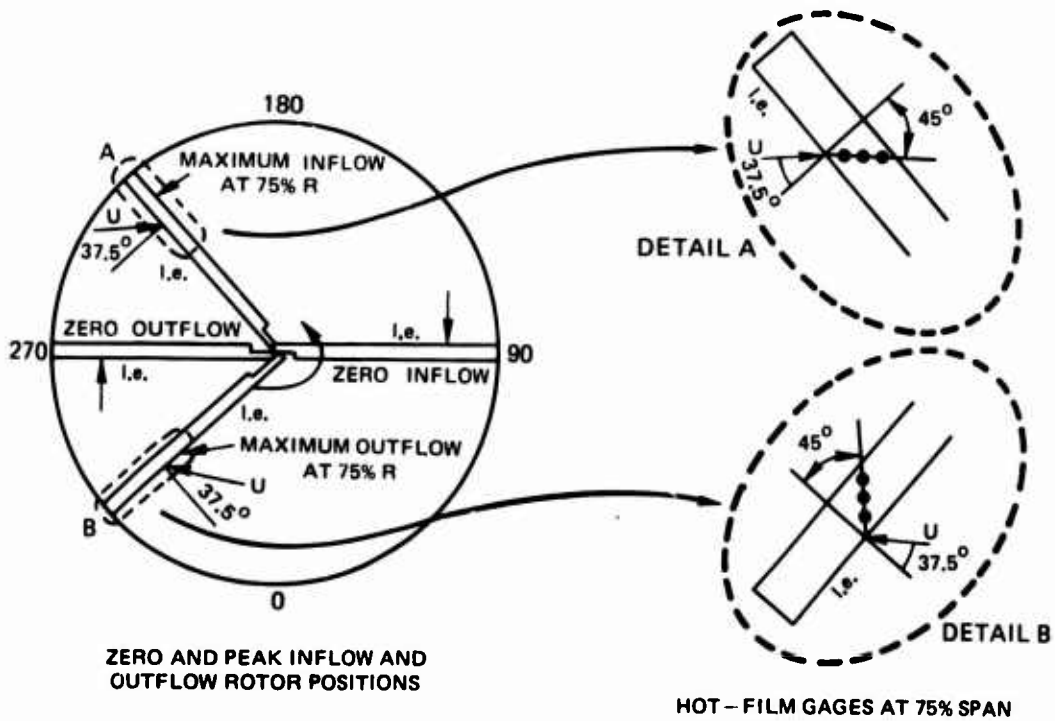
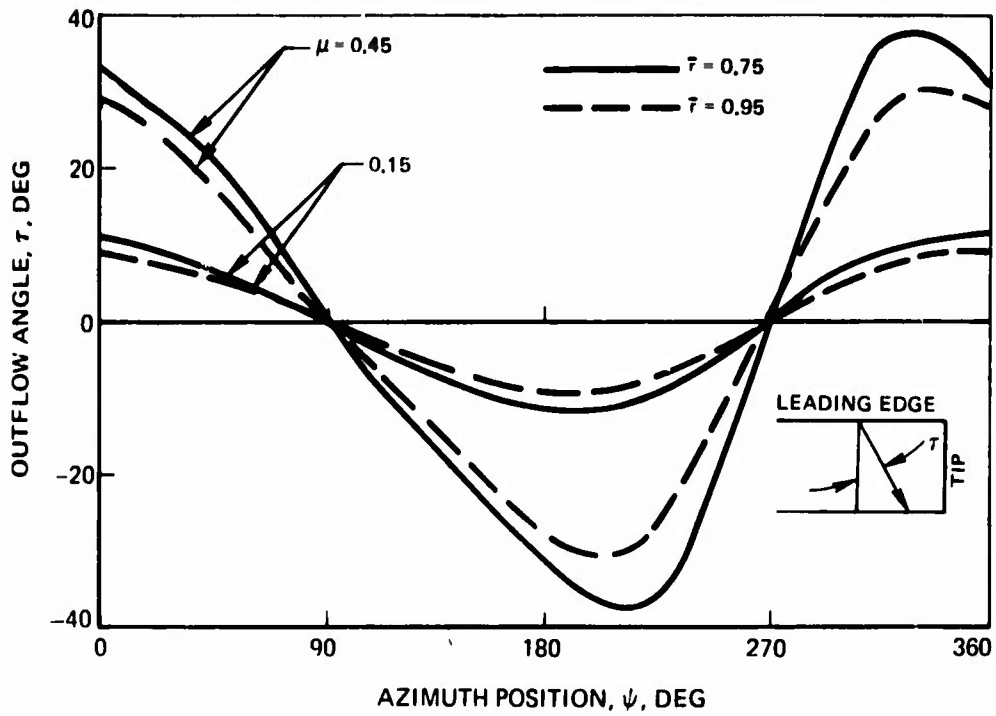


Figure 6. Resultant Velocity Estimates Used To Position Hot-Film Gages.

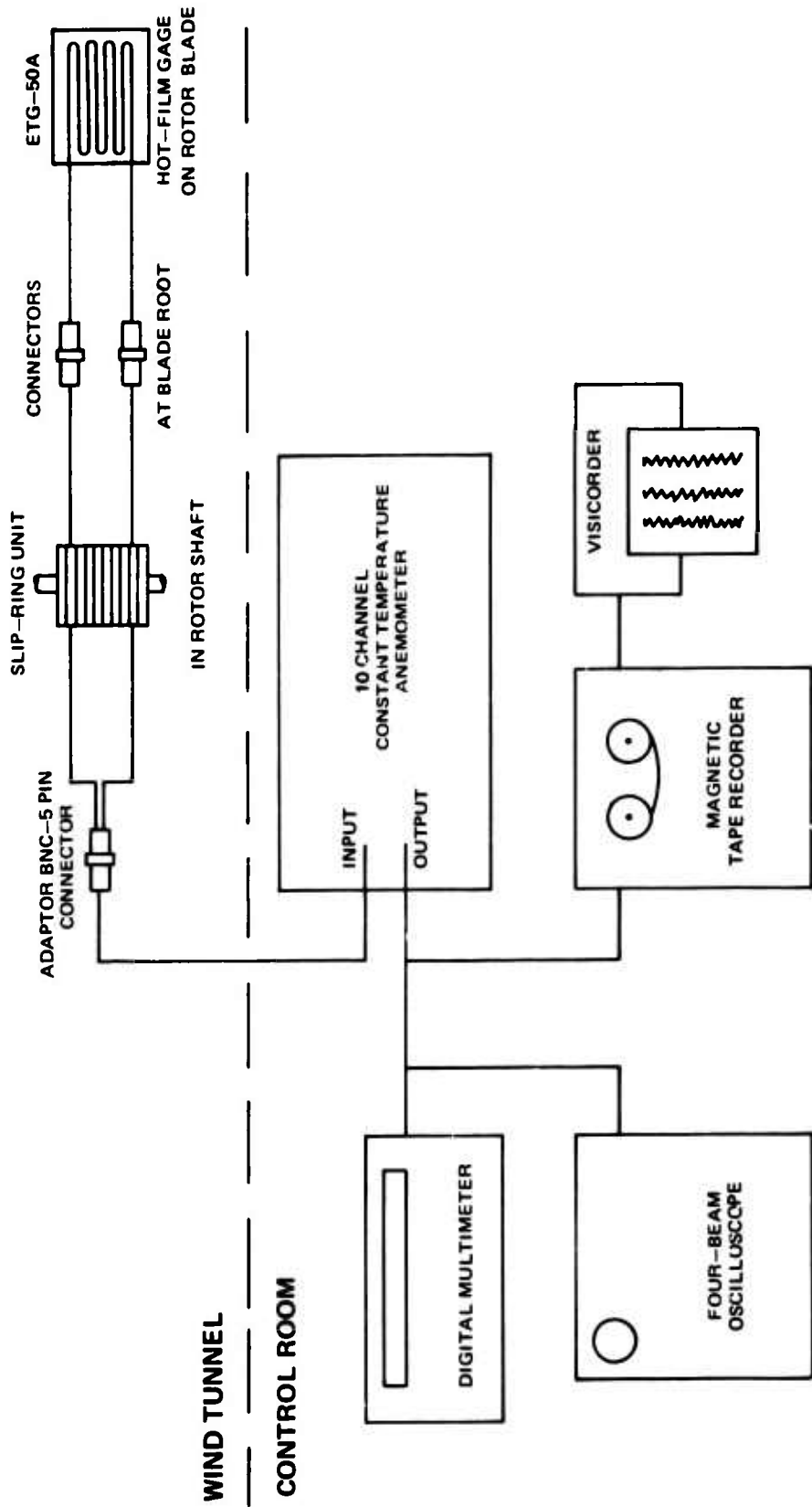


Figure 7. Experimental Apparatus for Hot-Film Measurements.

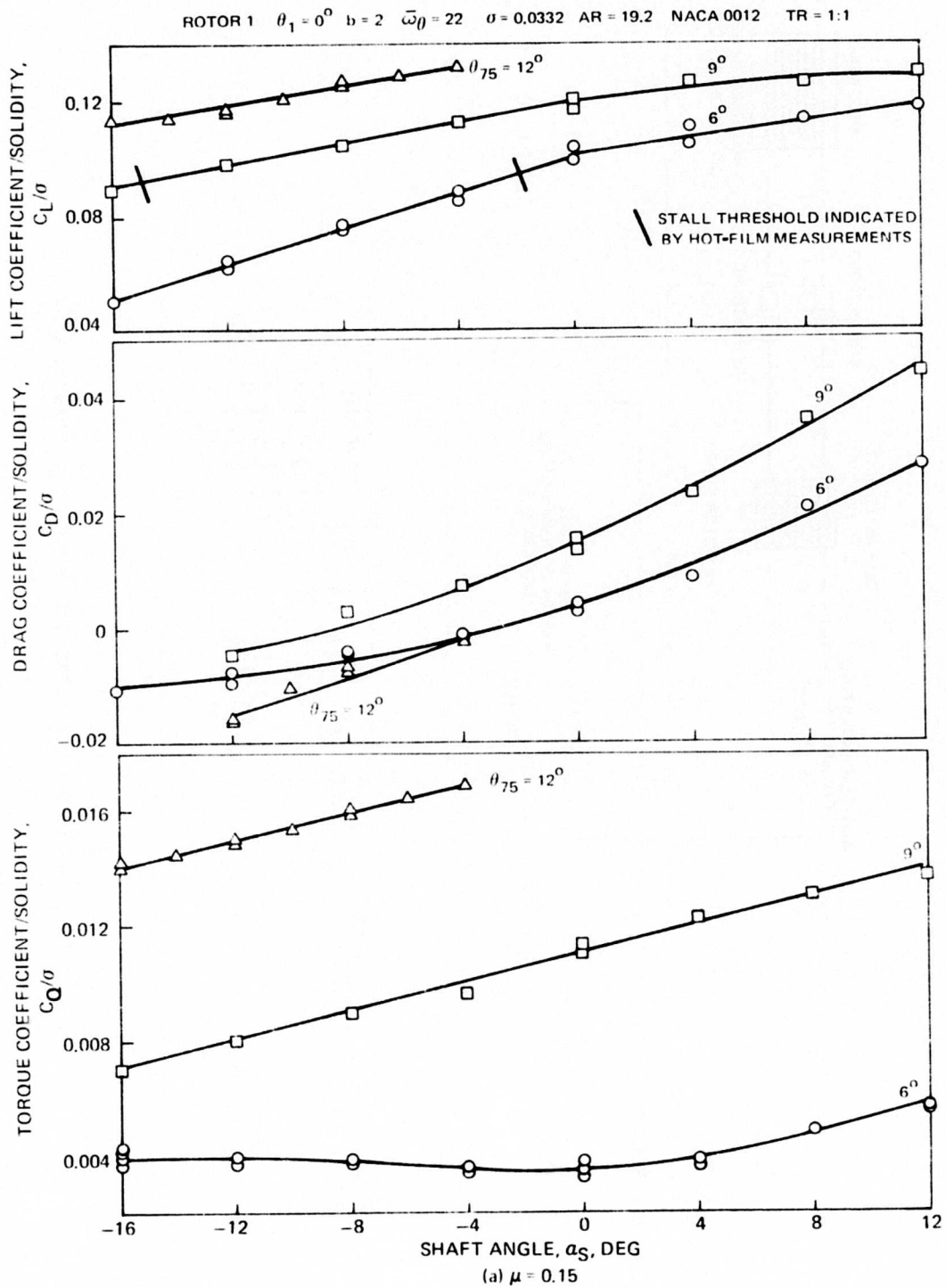
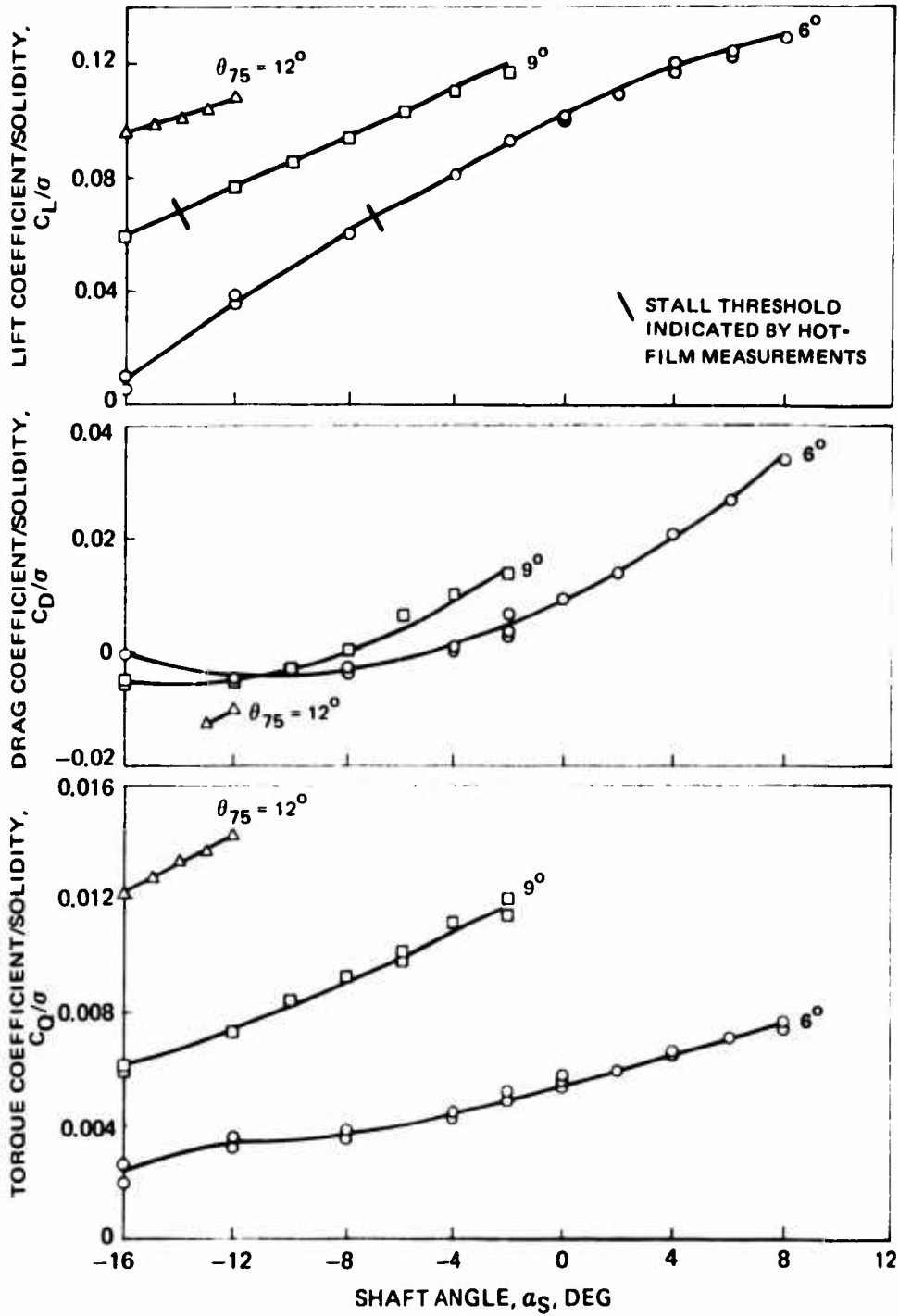


Figure 8. Rotor Number 1 Performance Data (Reference Rotor).



(b) $\mu = 0.30$

Figure 8. Continued.

ROTOR 1 $\theta_1 = 0^\circ$ $b = 2$ $\bar{\omega}_\theta = 22$ $\sigma = 0.0332$ $AR = 19.2$ $NACA 0012$ $TR = 1:1$

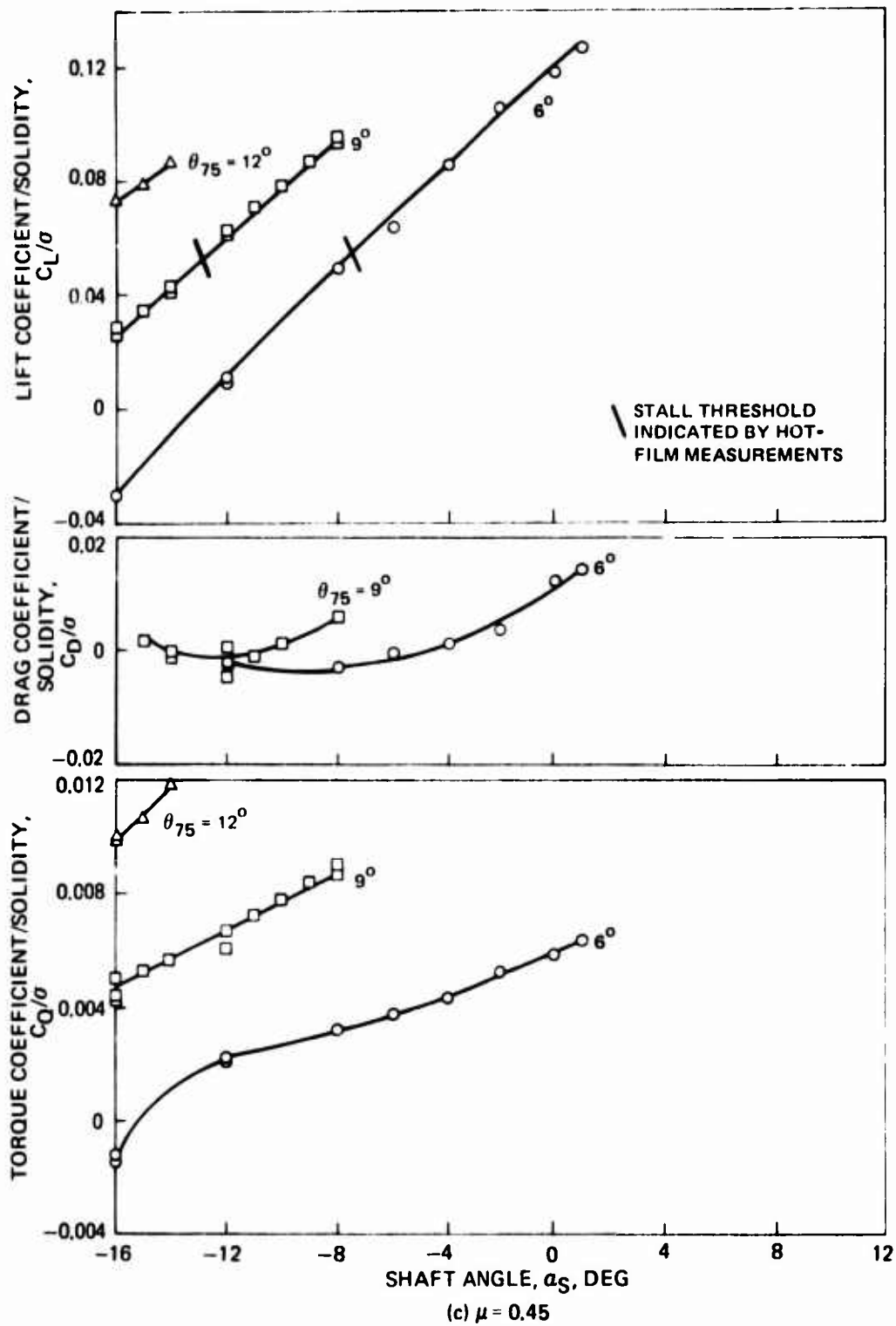


Figure 8. Concluded.

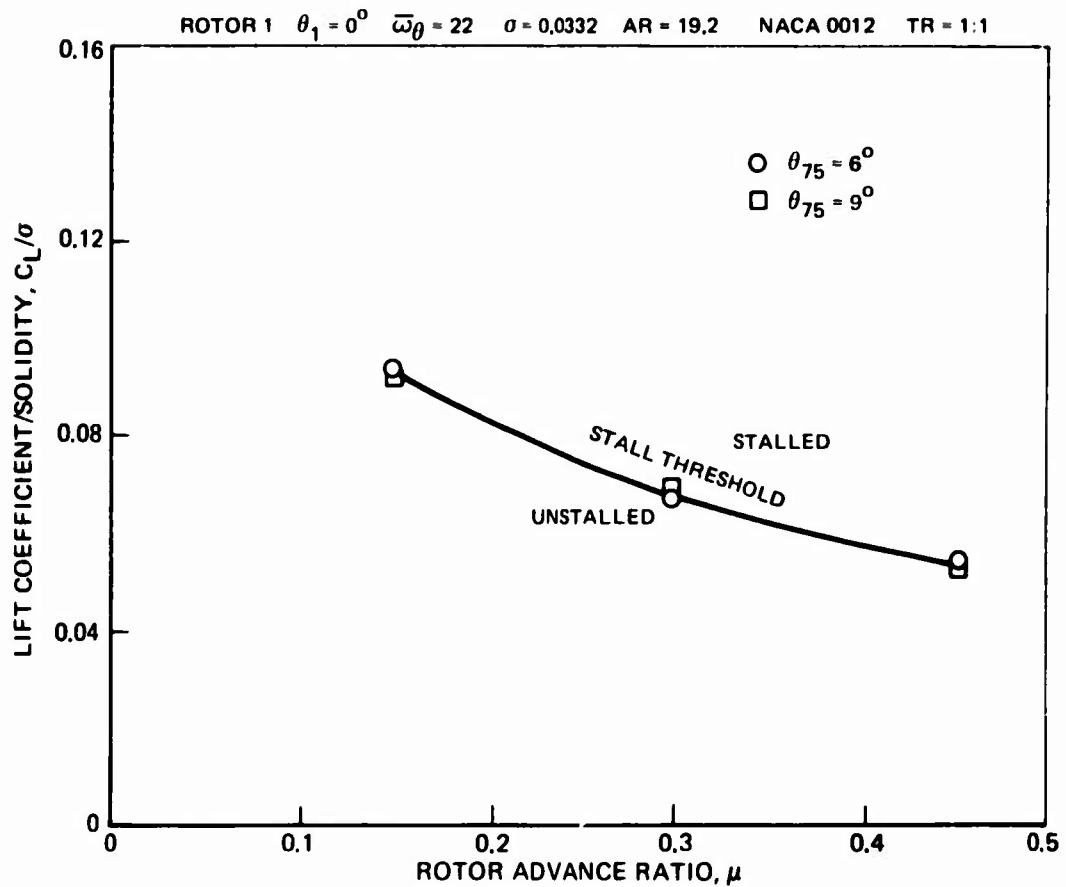


Figure 9. Effect of Collective Pitch on Rotor Lift at Stall Threshold Determined From Hot-Film Measurements for Rotor Number 1.

ROTOR 1 $\theta_1 = 0^\circ$ $b = 2$ $\omega\beta = 22$ $\sigma = 0.0332$ $AR = 19.2$ $NACA 0012$ $TR = 1:1$

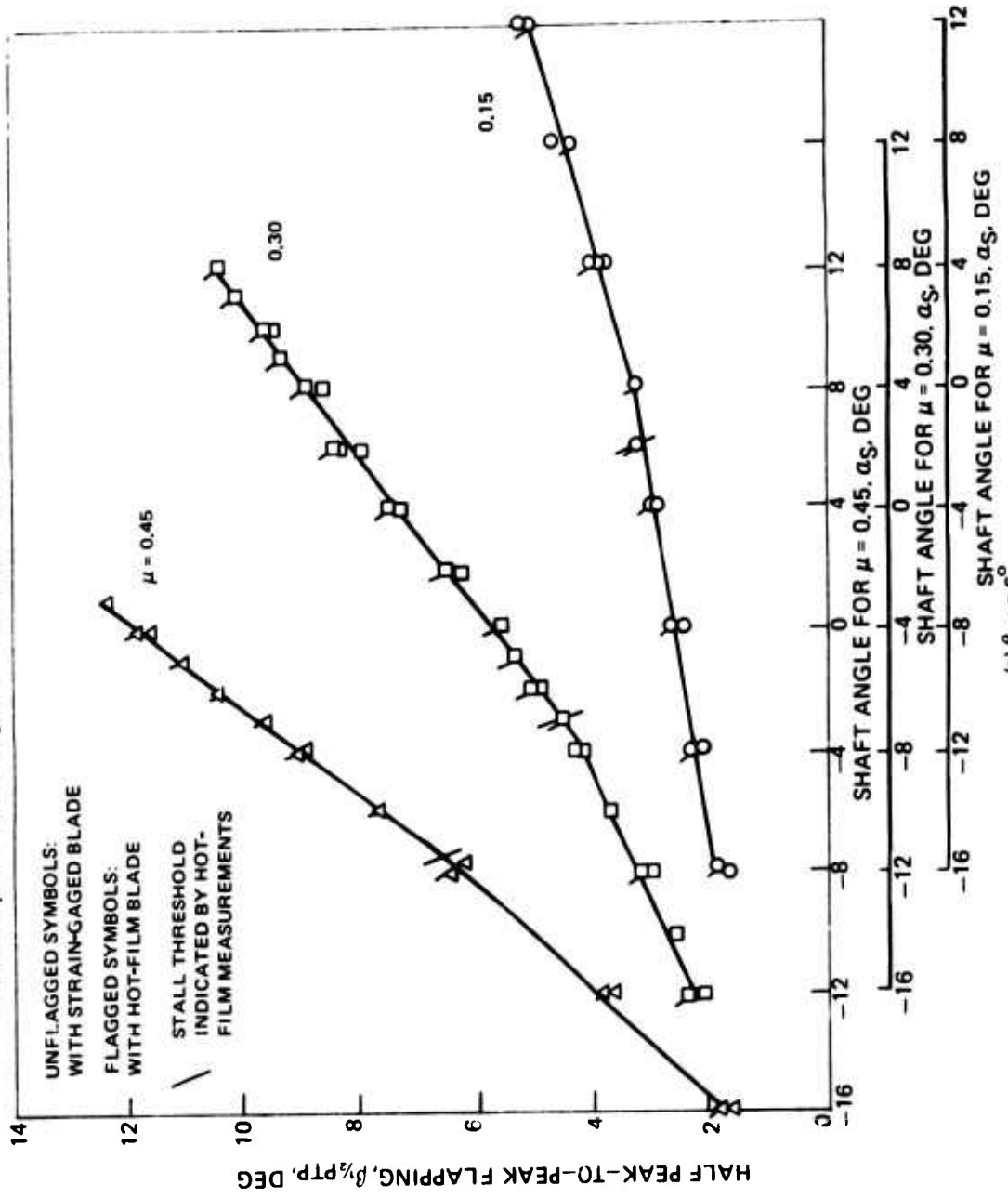
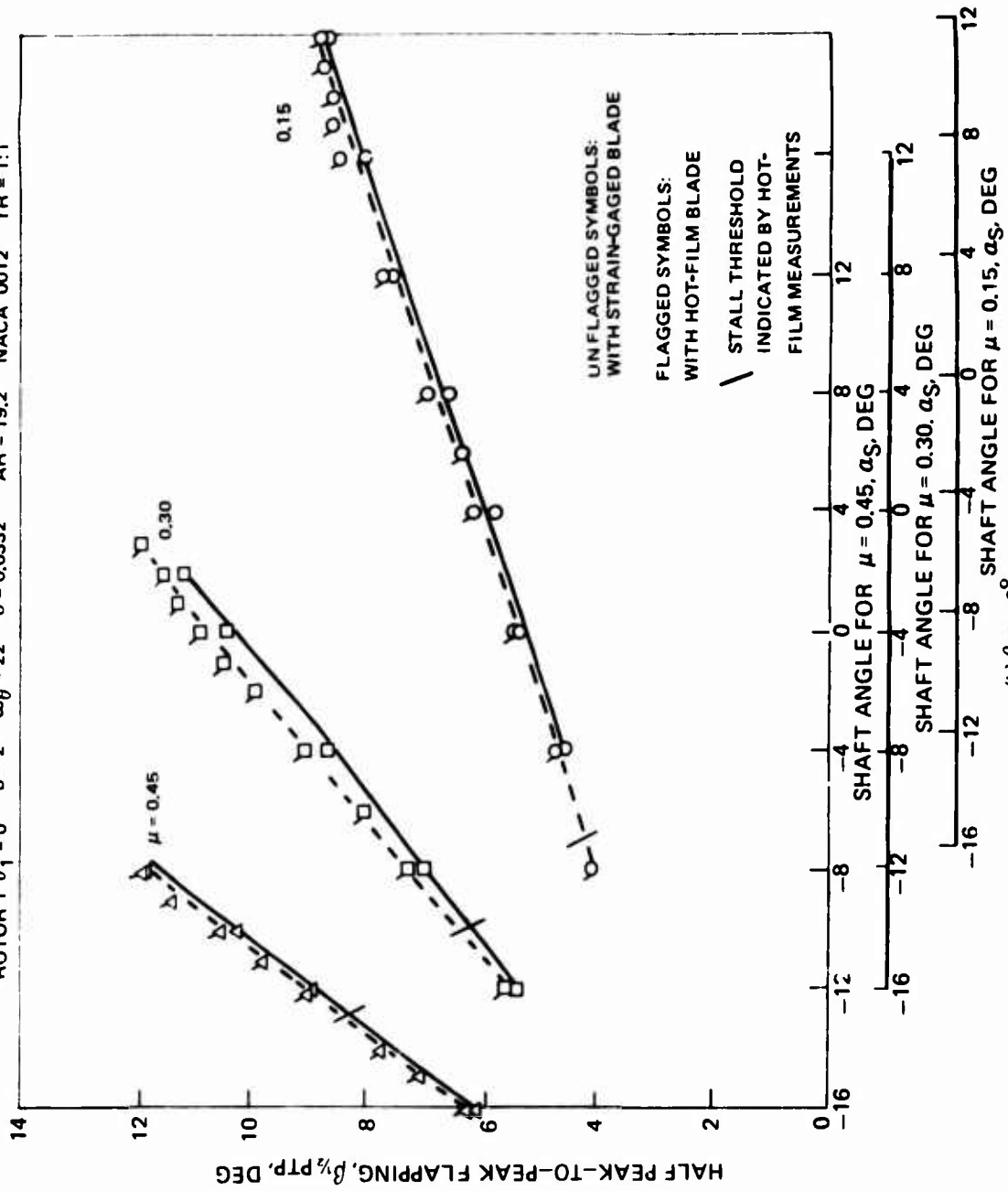


Figure 10. Vibratory Flapping Data for Rotor Number 1.

ROTOR 1 $\theta_1 = 0^\circ$ $b = 2$ $\omega\theta = 22$ $\sigma = 0.0332$ $AR = 19.2$ $NACA 0012$ $TR = 1:1$



(b) $\theta_{75} = 9^\circ$

Figure 10. Concluded.

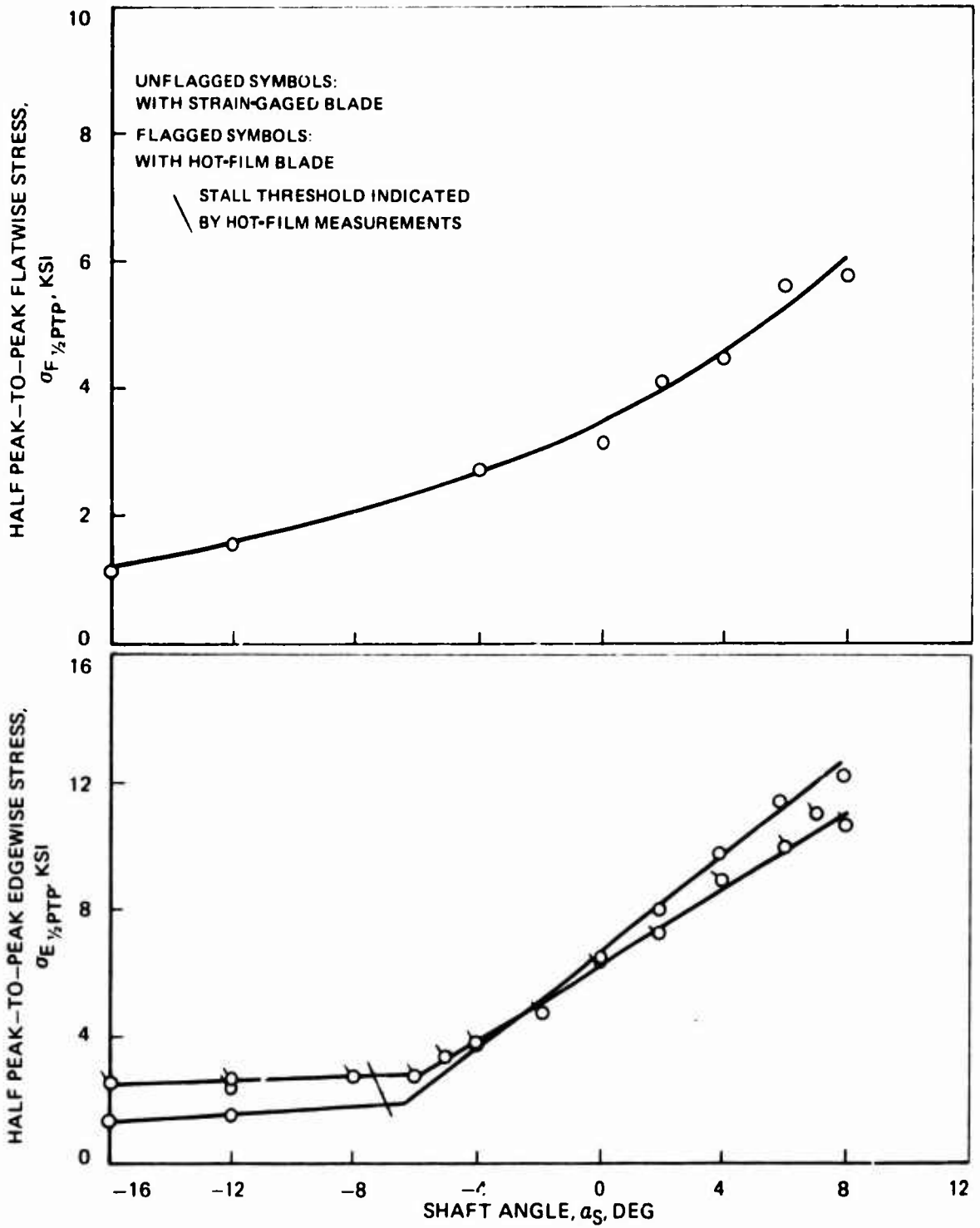


Figure 11. Vibratory Flatwise and Edgewise Stress Data for Rotor Number 1.

ROTOR 1 $\theta_1 = 0^\circ$ $b = 2$ $\bar{\omega}_\theta = 22$ $\sigma = 0.0332$ $AR = 19.2$ $NACA 0012$ $TR = 1:1$

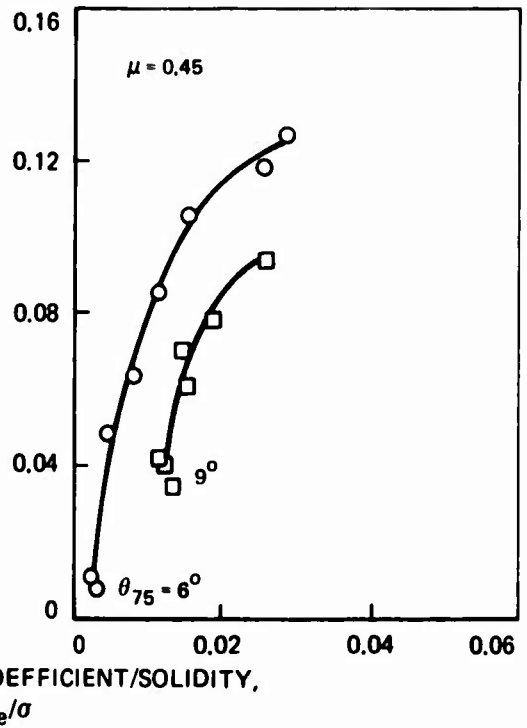
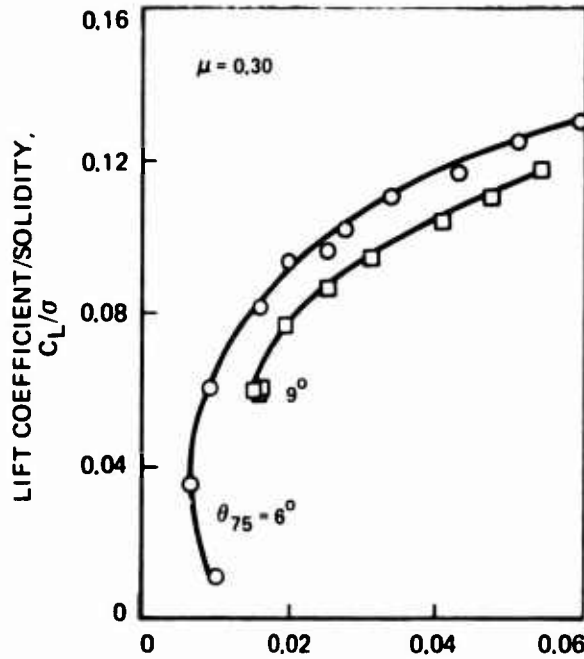
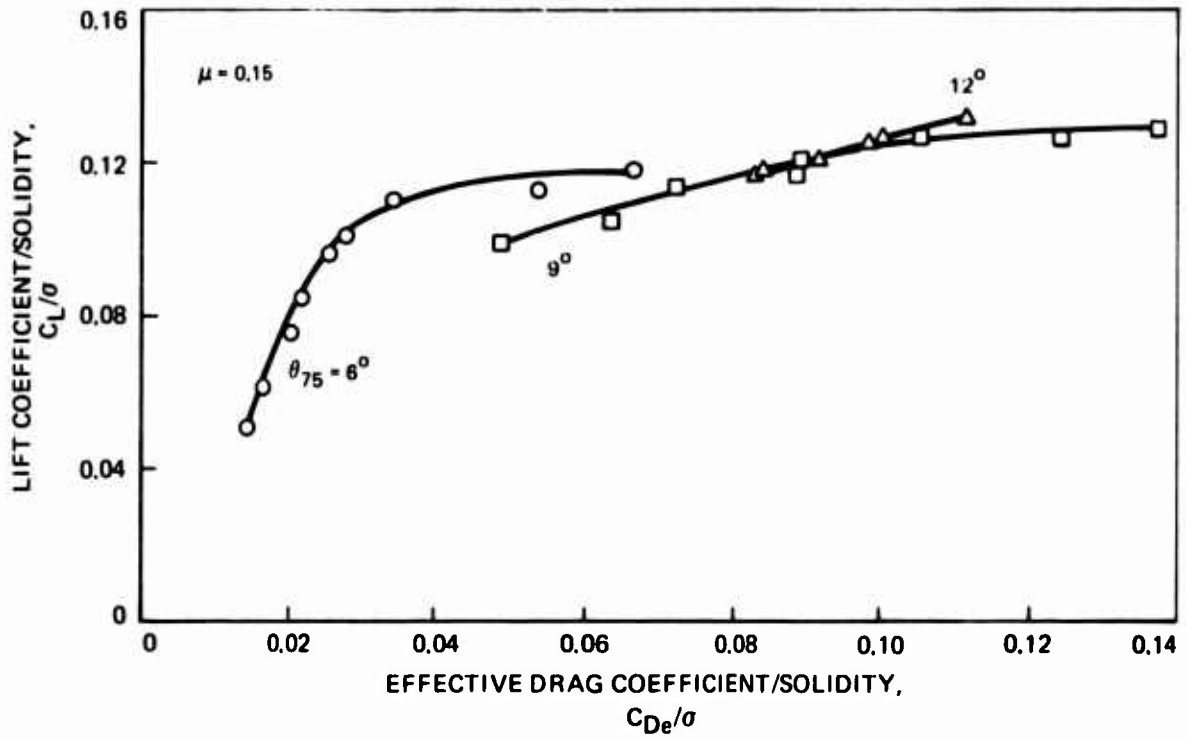


Figure 12. Rotor Performance Based on Effective Drag for Rotor Number 1.

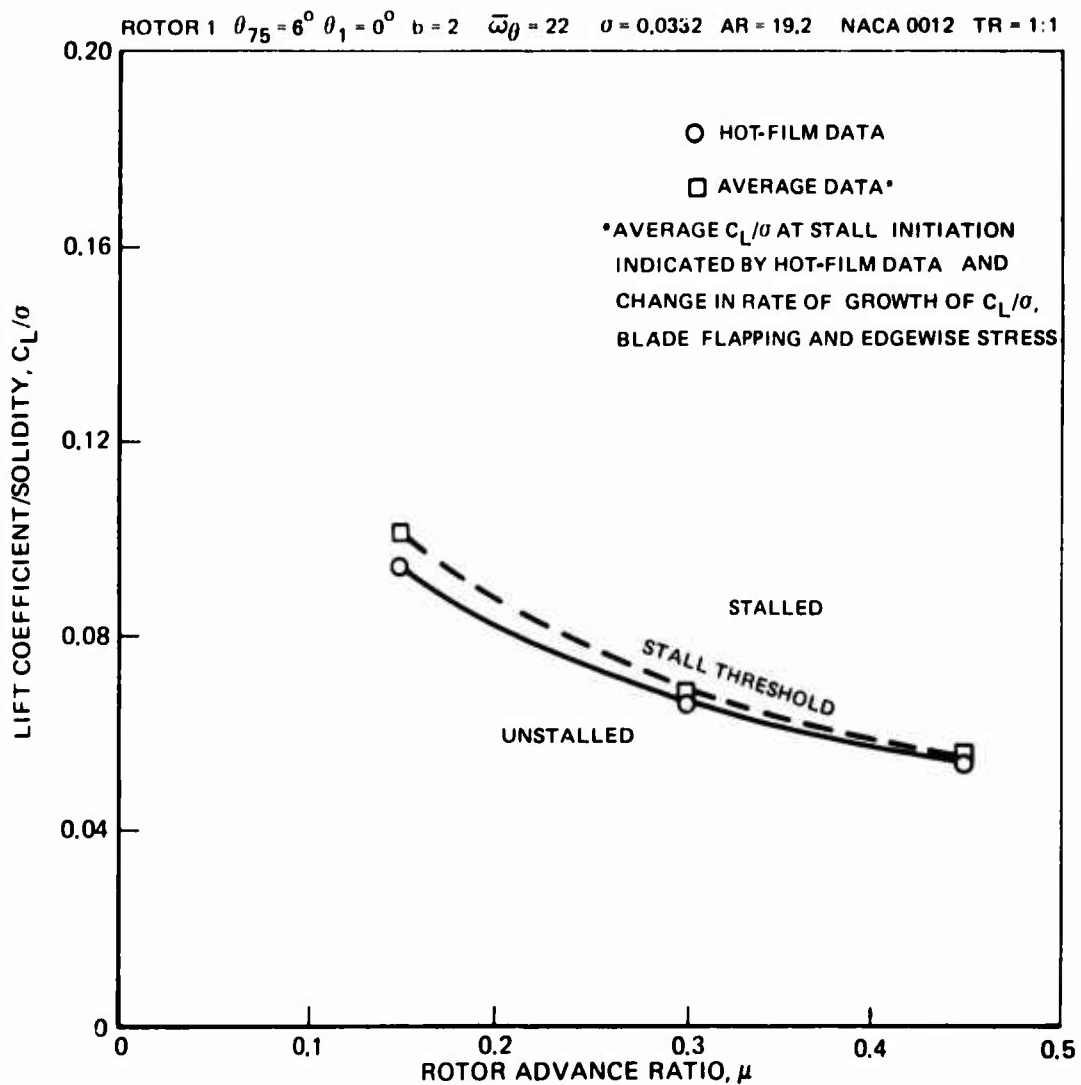


Figure 13. Comparison of Rotor Lift at Stall Threshold Indicated by Hot-Film and Average Data for Rotor Number 1.

$b = 2$ $\omega\theta = 23$ $\sigma = 0.0332$ $AR = 19.2$ $NACA 0012$ $TR = 1:1$

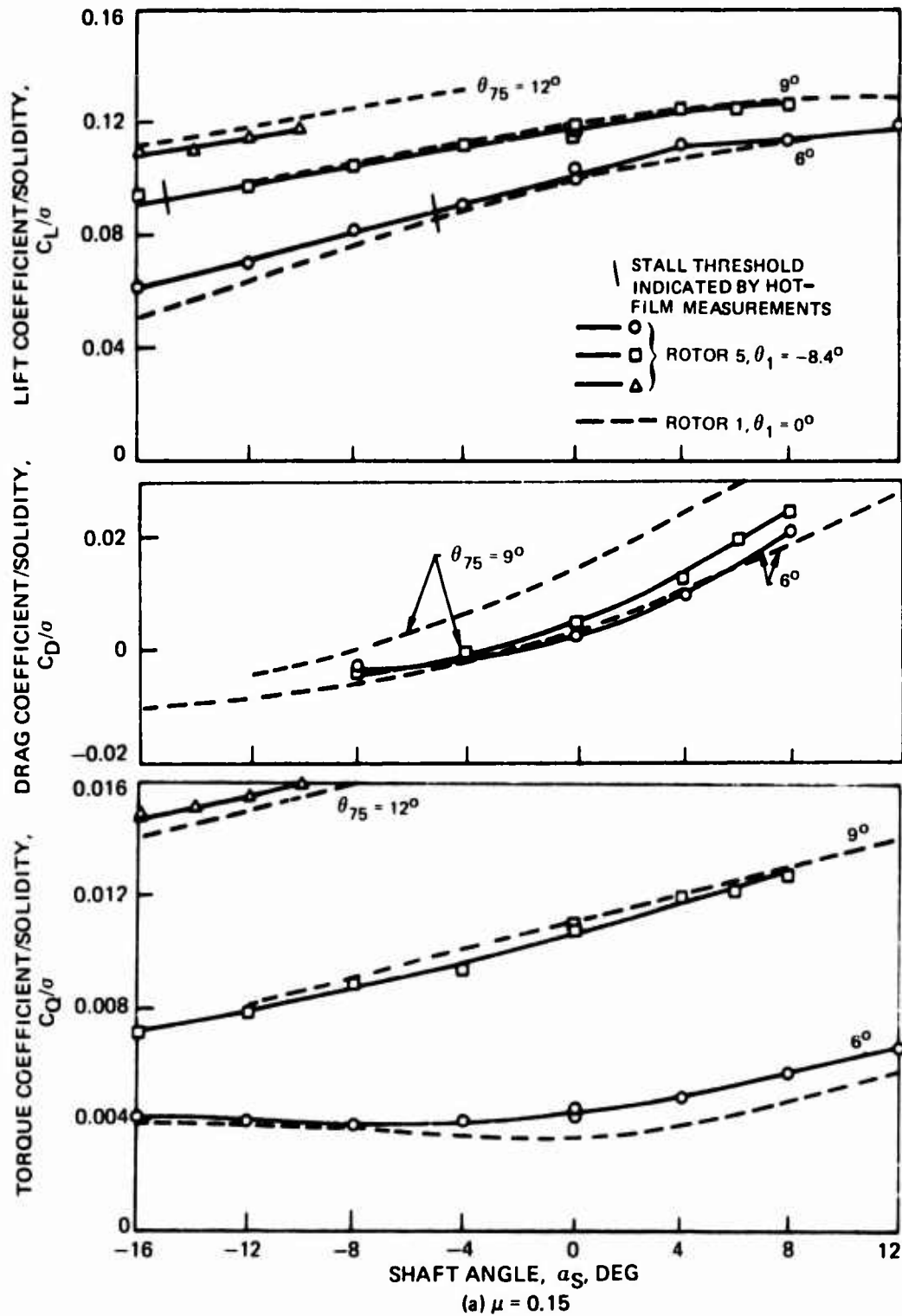


Figure 14. Effect of Blade Twist on Rotor Performance.

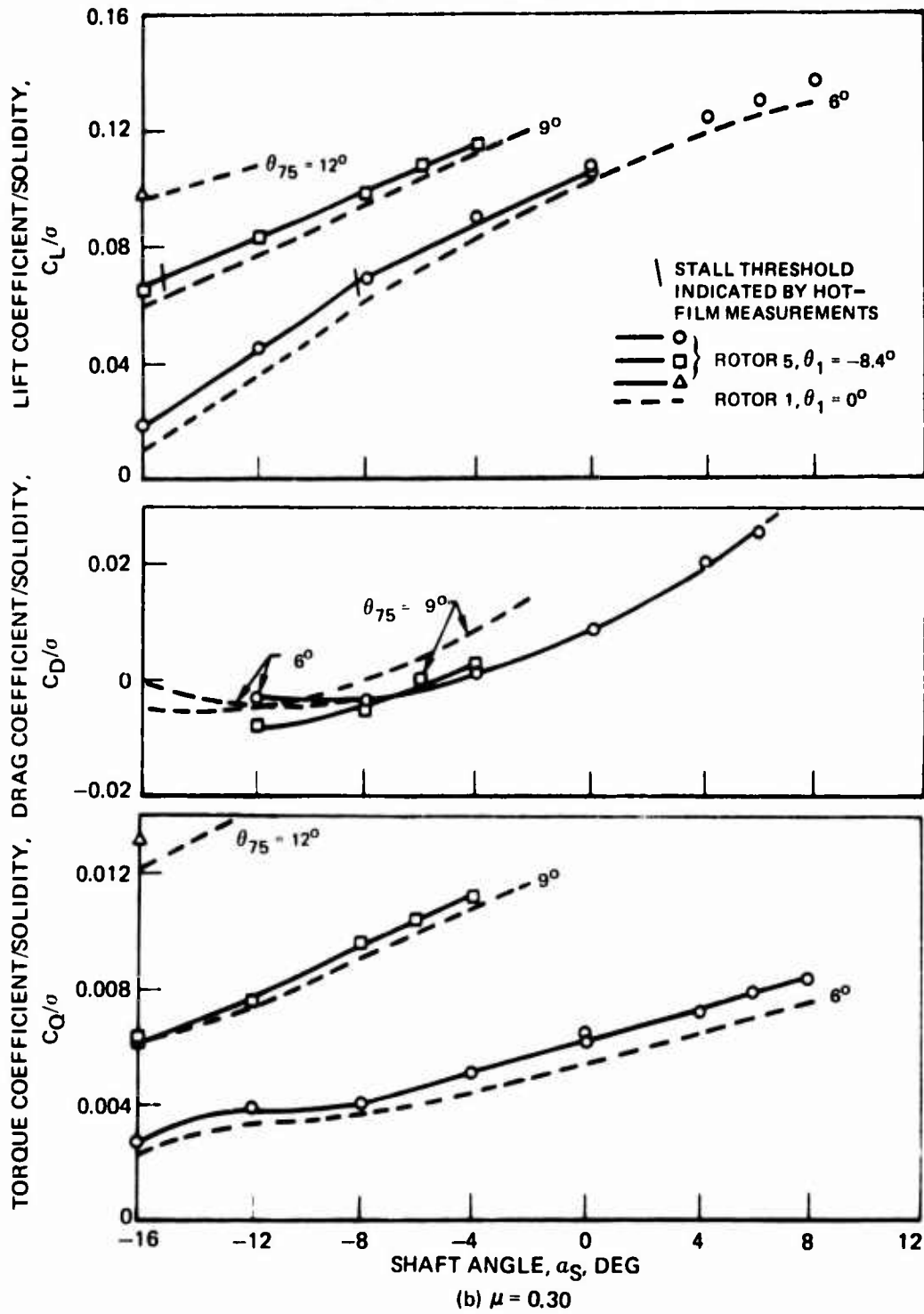


Figure 14. Continued.

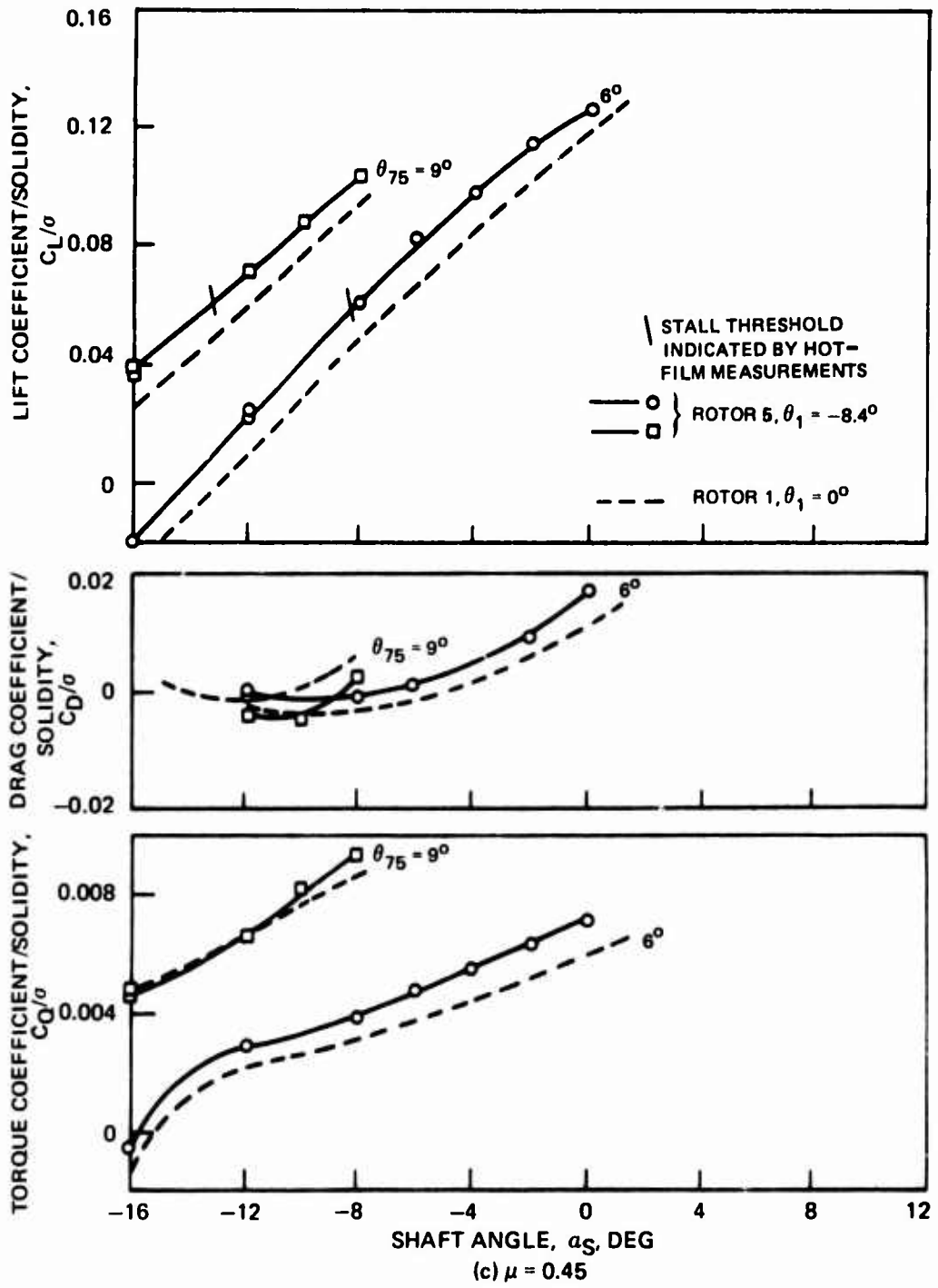


Figure 14. Co. cluded.

$b = 2$ $\omega/\theta = 23$ $\sigma = 0.0332$ $AR = 19.2$ $NACA 0012$ $TR = 1:1$

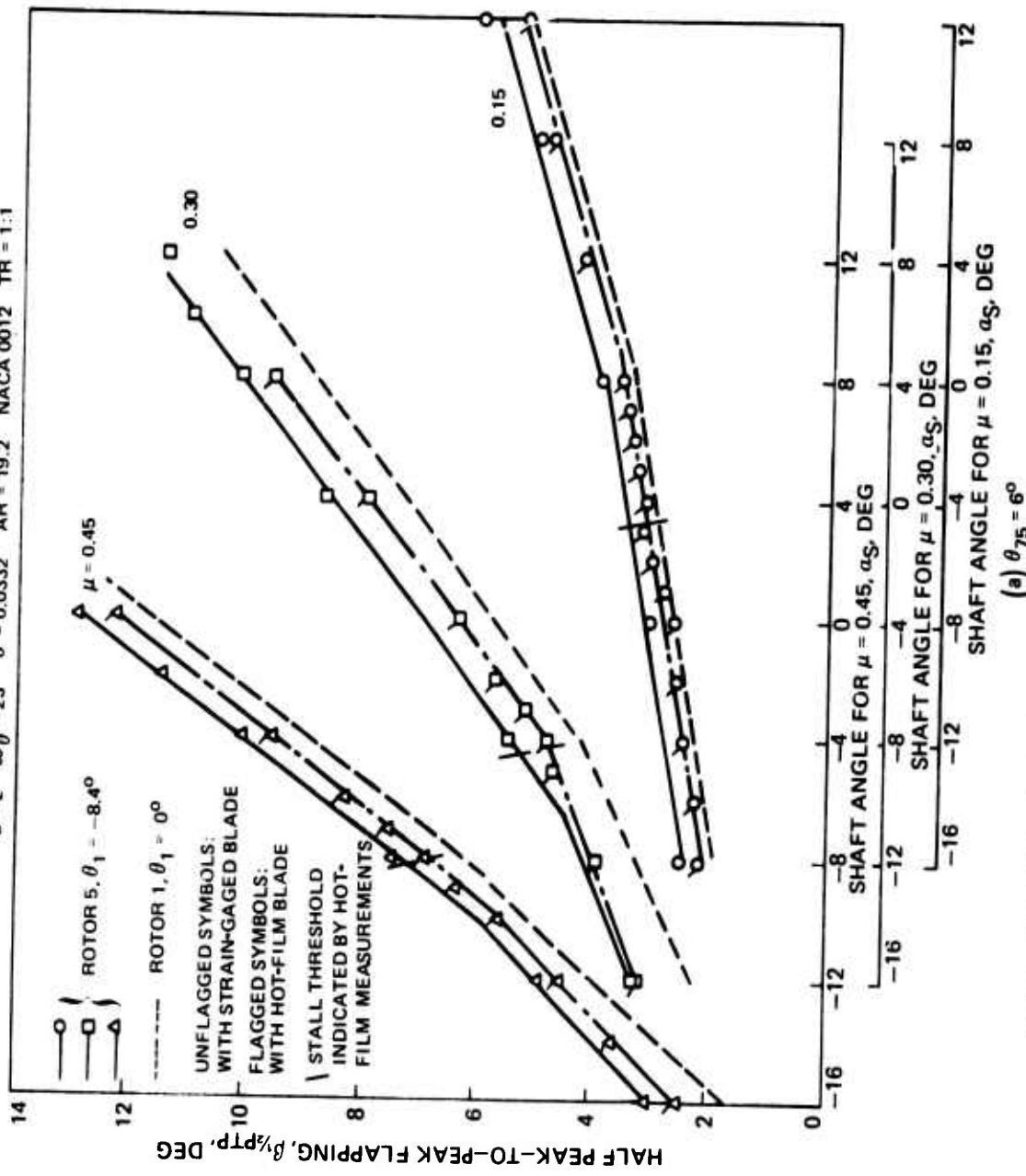


Figure 15. Effect of Blade Twist on Blade Flapping Response.
(a) $\theta_{75} = 6^\circ$

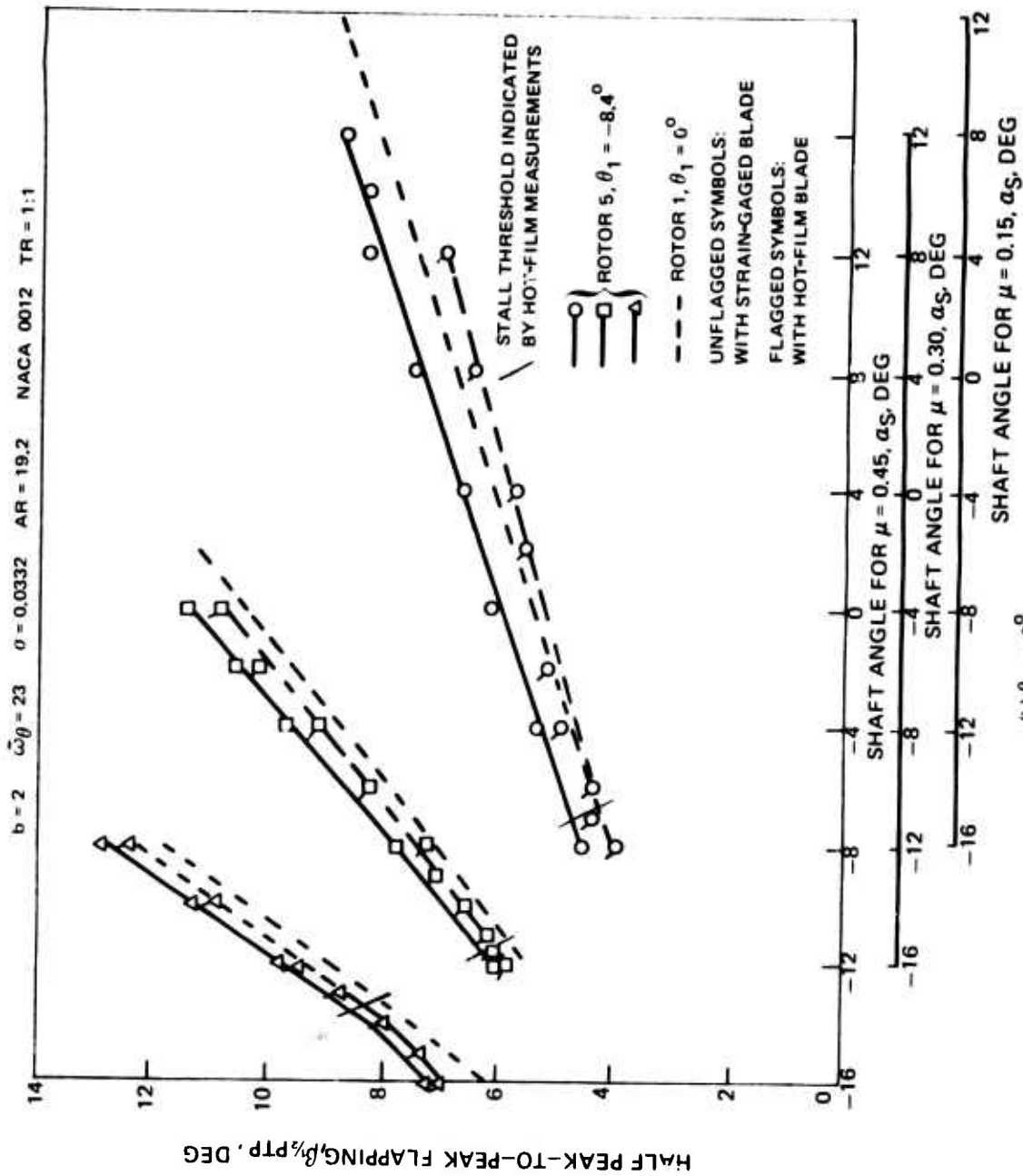


Figure 15. Concluded.

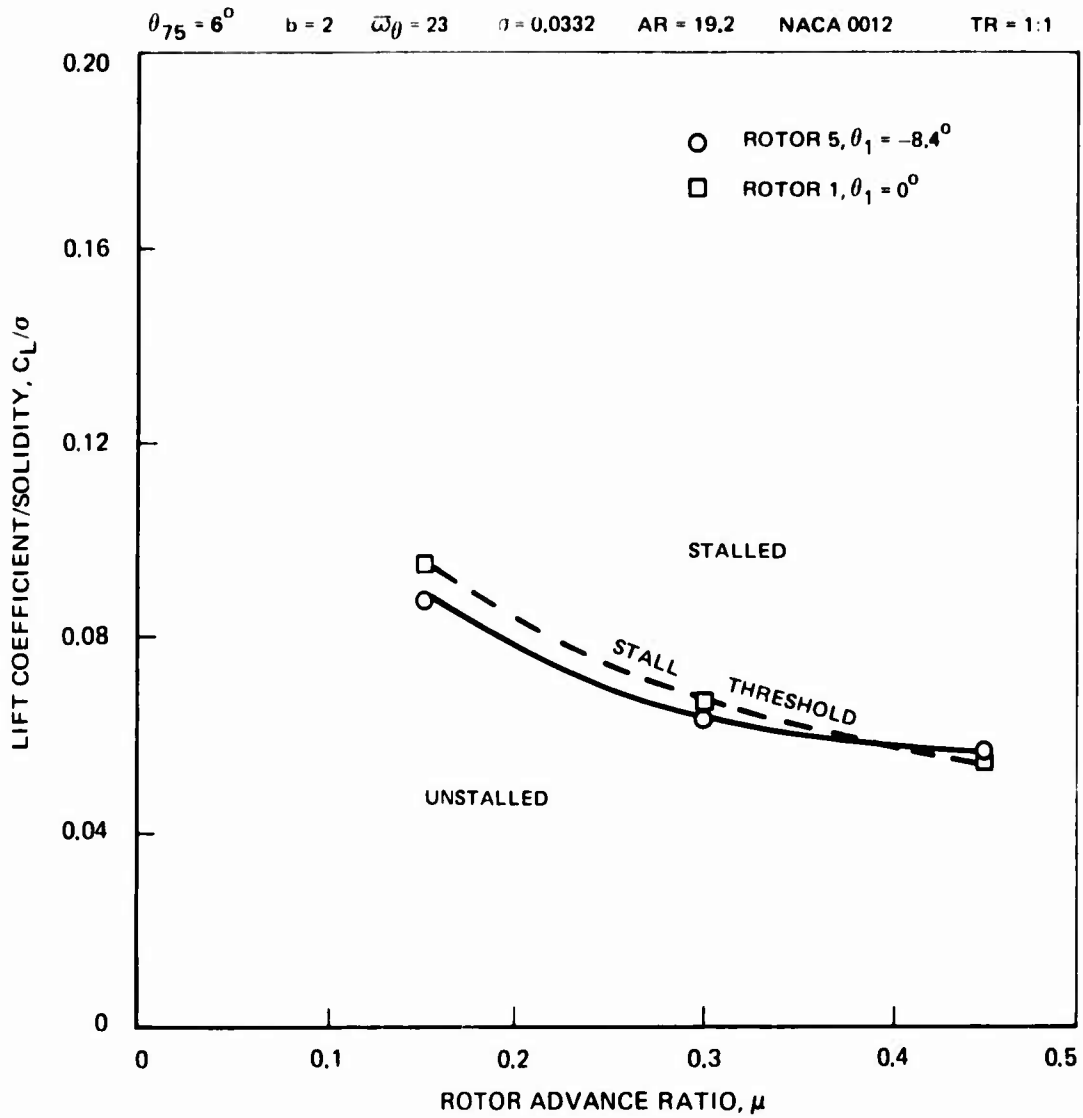


Figure 16. Effect of Twist on Rotor Lift at Stall Threshold Indicated by Hot-Film Measurements

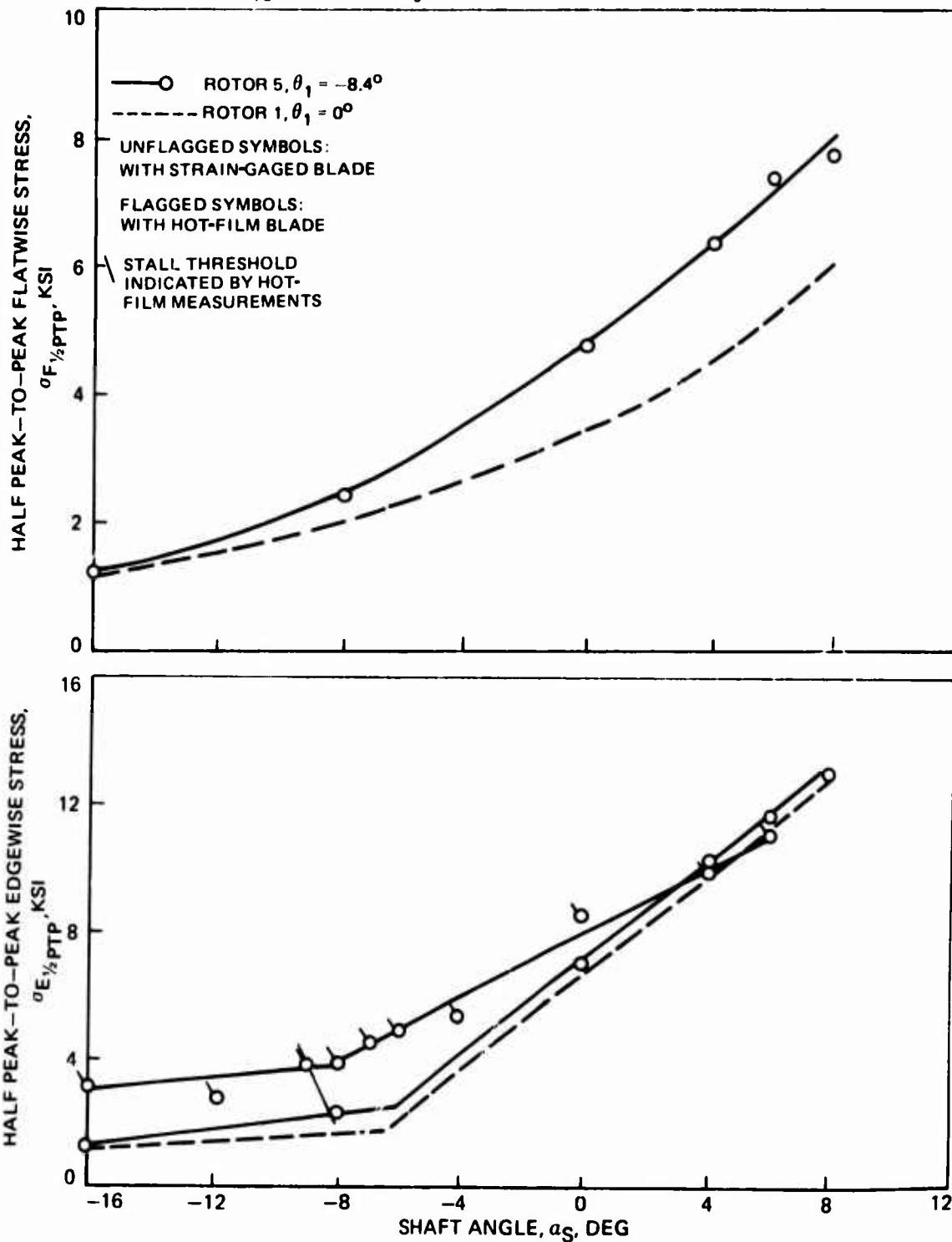


Figure 17. Effect of Blade Twist on Vibratory Flatwise and Edgewise Stress.

$\theta_{75} = 6^\circ$ $b = 2$ $\bar{\omega}_\theta = 23$ $u = 0.0332$ $AR = 19.2$ $NACA\ 0012$ $TR = 1:1$

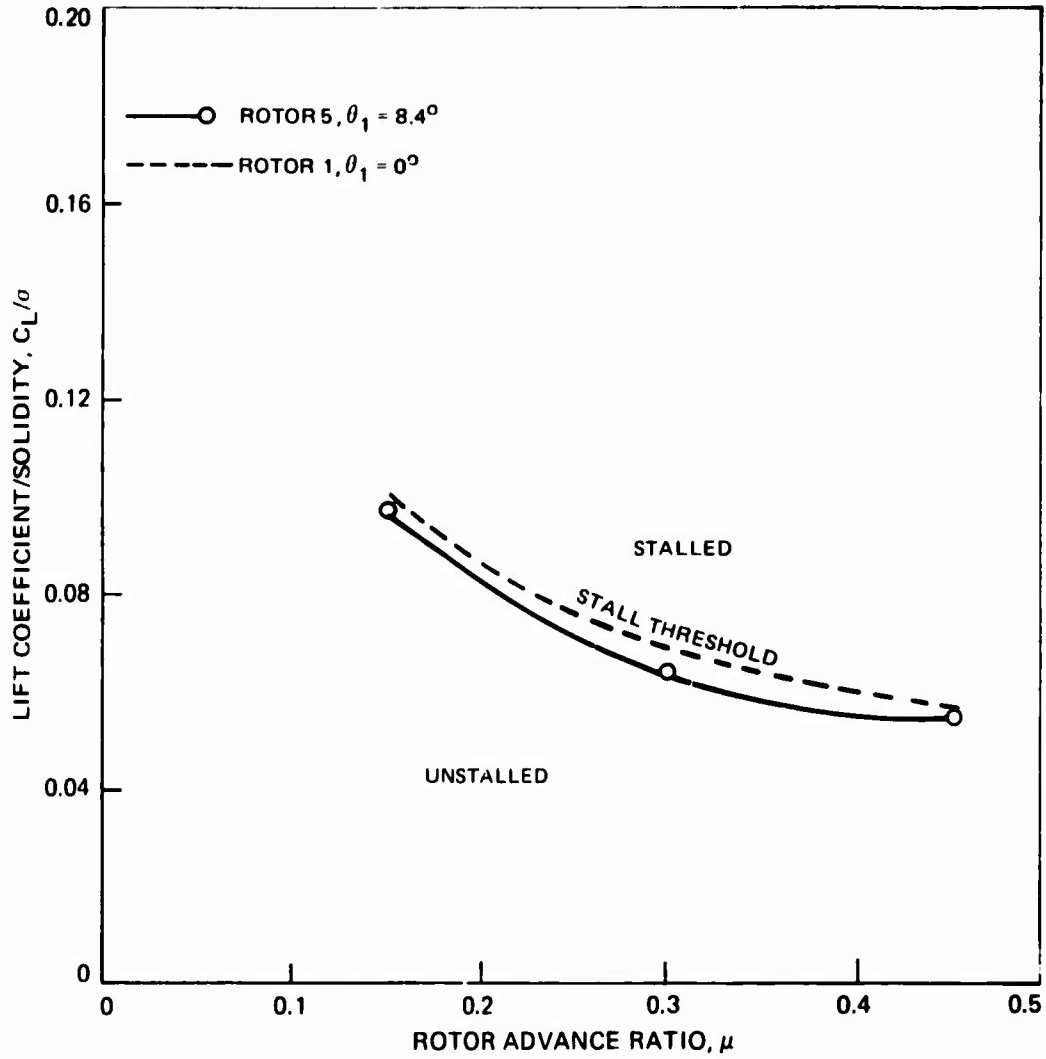


Figure 18 . Effect of Blade Twist on Rotor Lift at Stall
Threshold -- Average of All Stall Indicators.

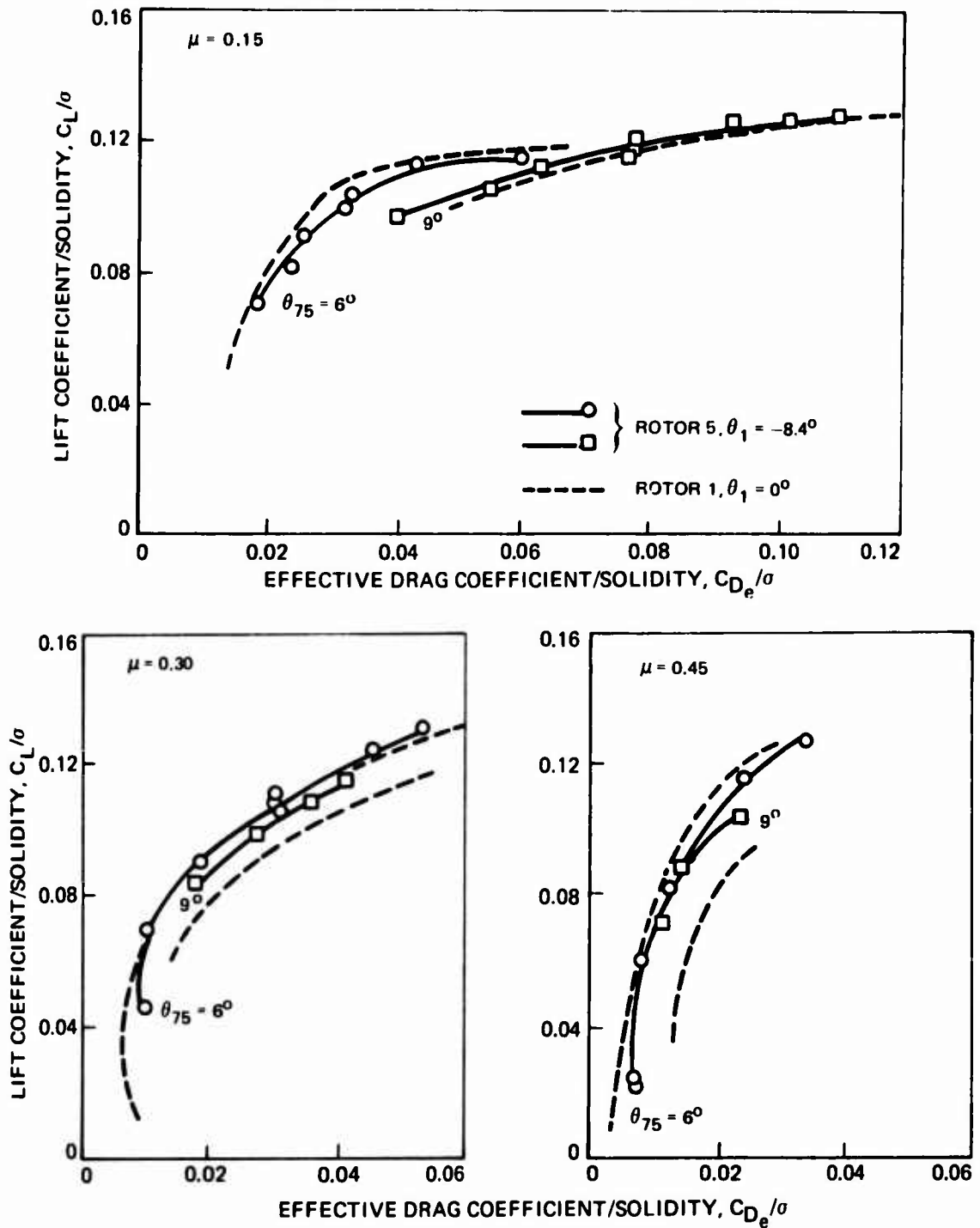


Figure 19. Effect of Blade Twist on Rotor Performance Compared on a Lift-Effective Drag Basis.

ROTOR 5 $\theta_{75} = 6^\circ$ $\theta_1 = -8.4^\circ$ $b = 2$ $\bar{\omega} = 23$ $\sigma = 0.0332$ $AR = 19.2$ $NACA 0012$ $TR = 1:1$

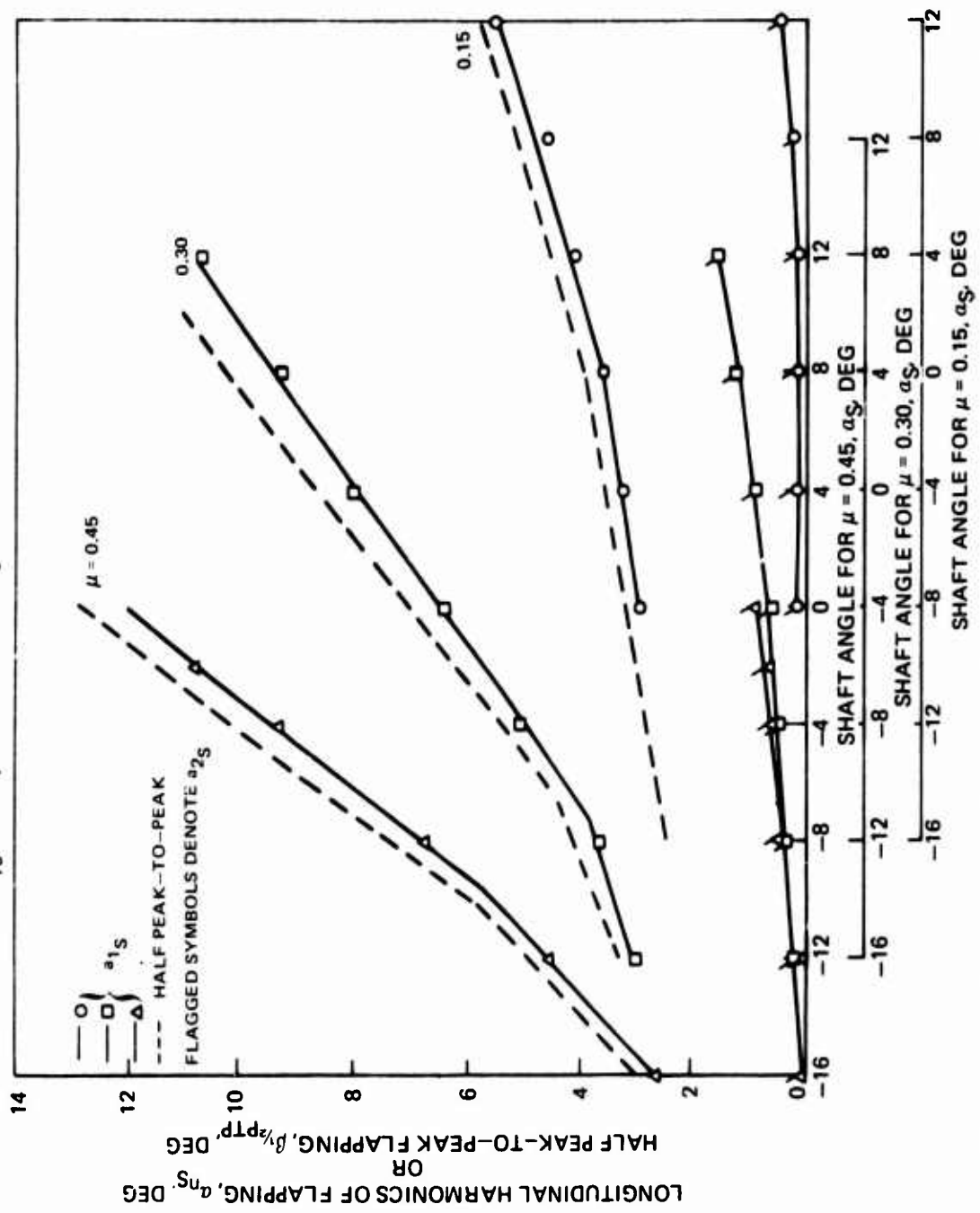


Figure 20 . Comparison of Vibratory Amplitudes and Longitudinal Harmonics of Blade Flapping.

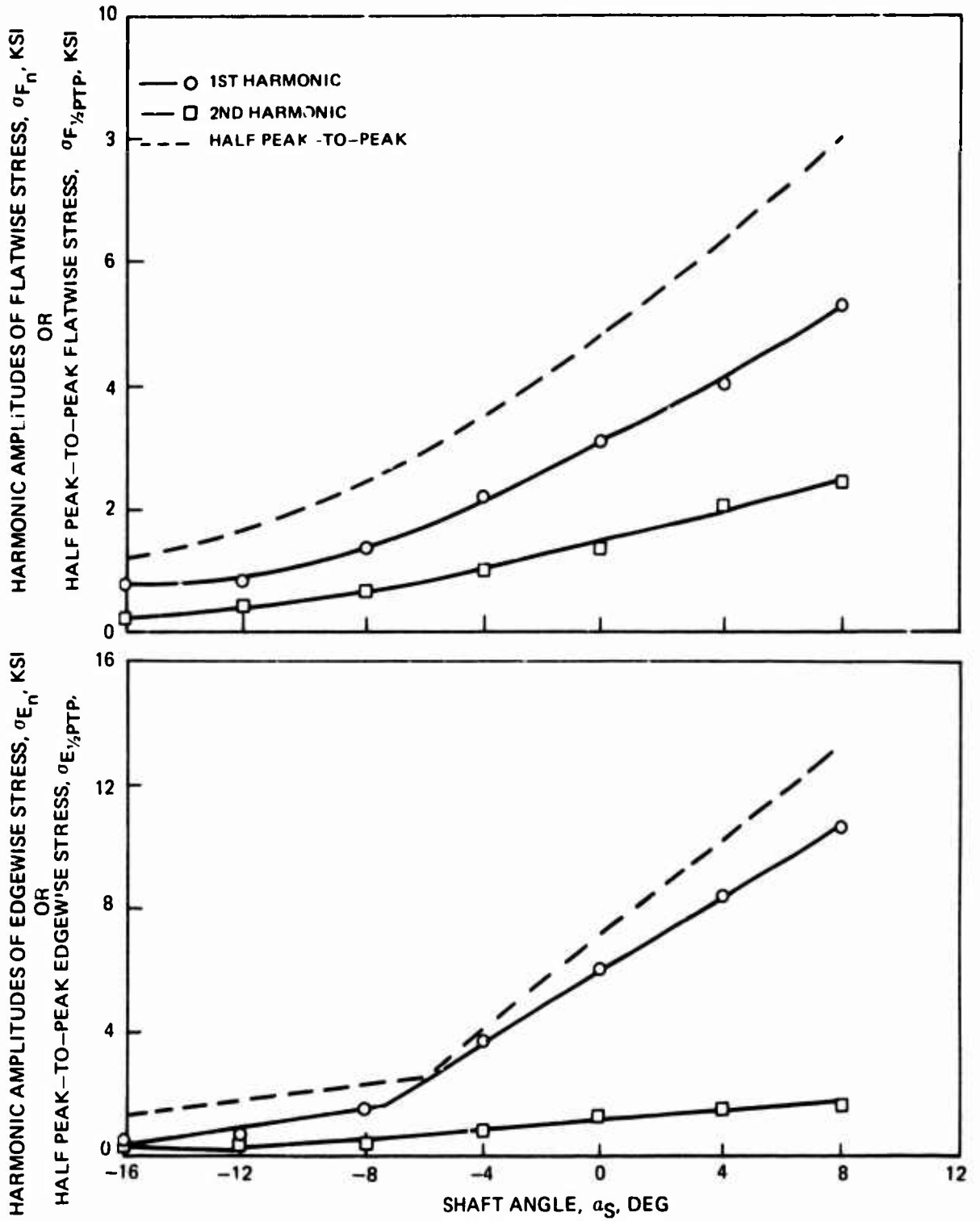


Figure 21 . Comparison of Vibratory and Harmonic Amplitudes of Flatwise and Edgewise Stress.

ROTOR 5 $\mu = 0.3$ $\theta_{75} = 6^\circ$ $\theta_1 = -8.4^\circ$ $b = 2$ $\bar{\omega}_\theta = 23$ $\sigma = 0.0332$ $AR = 19.2$ $NACA\ 0012\ TR = 1:1$

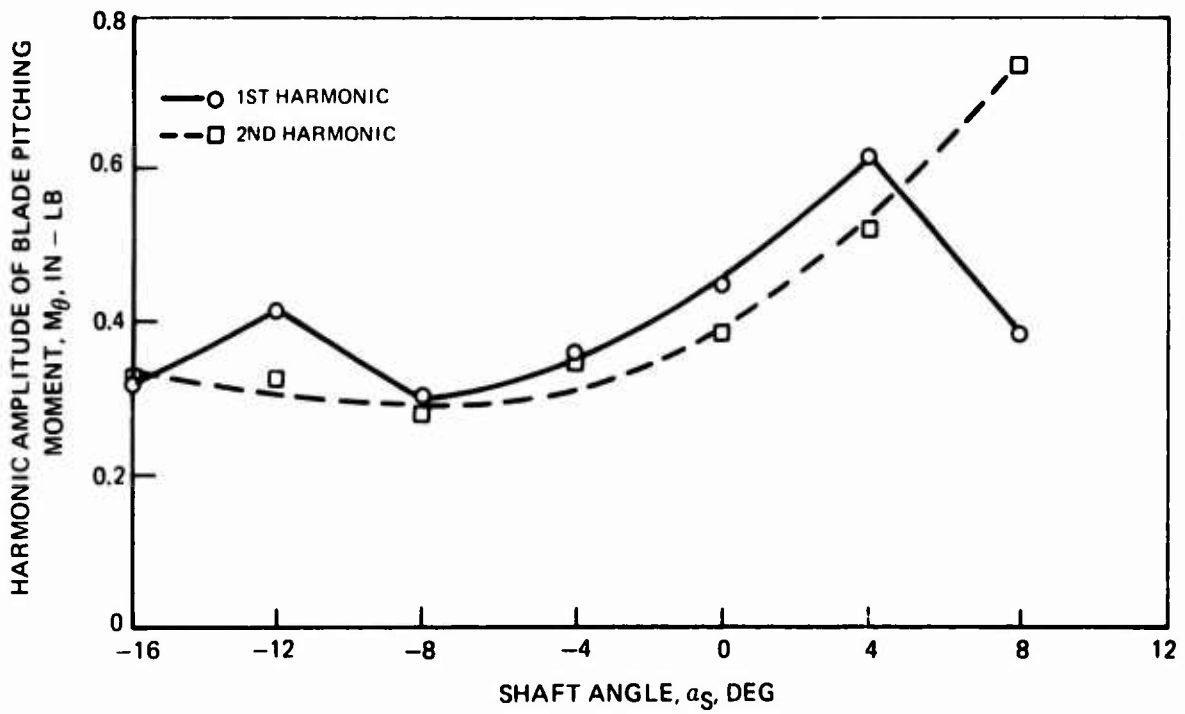


Figure 22. Harmonic Amplitudes of Blade Pitching Moment.

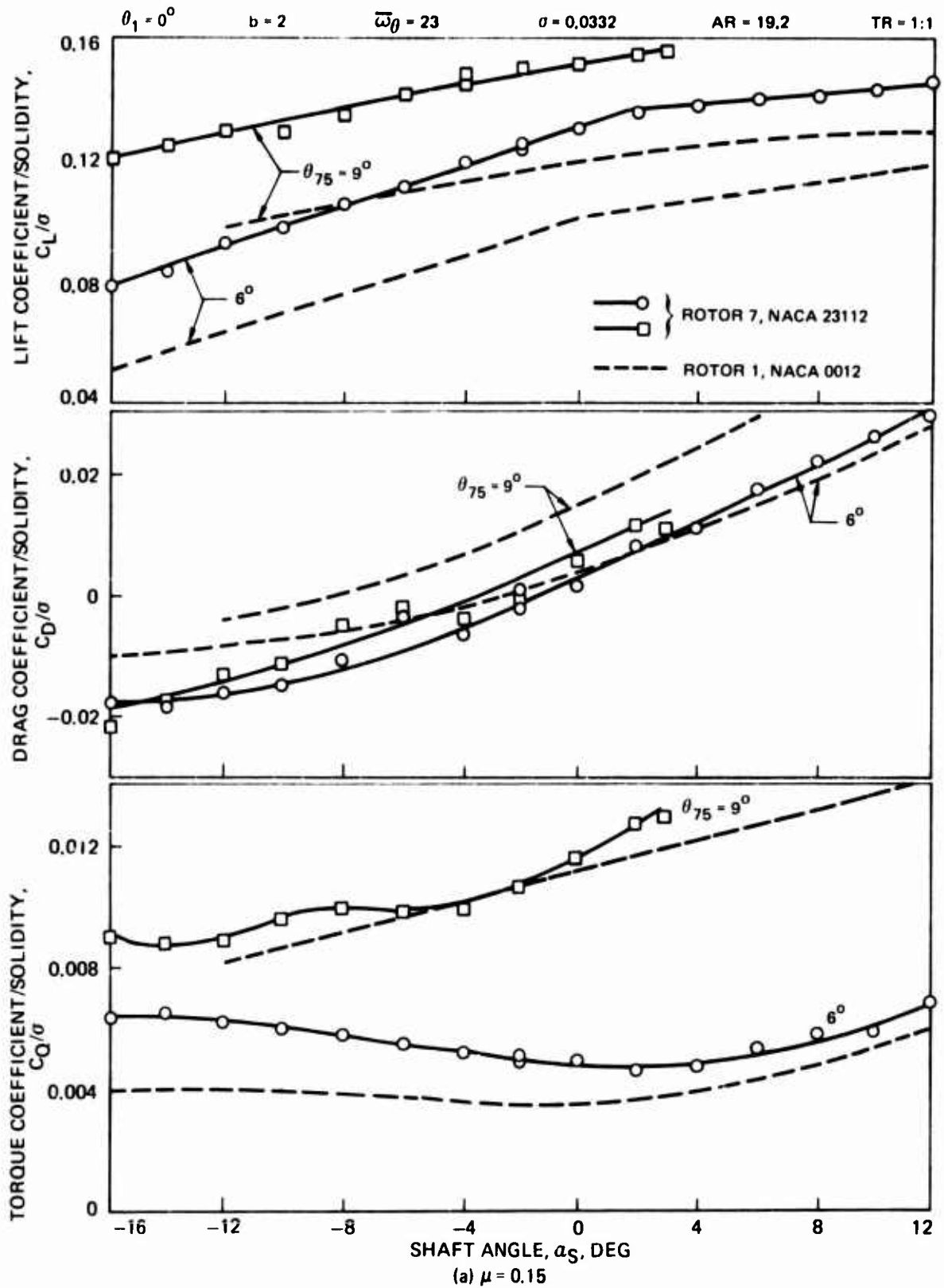


Figure 23. Effect of Blade Section Camber on Rotor Performance.

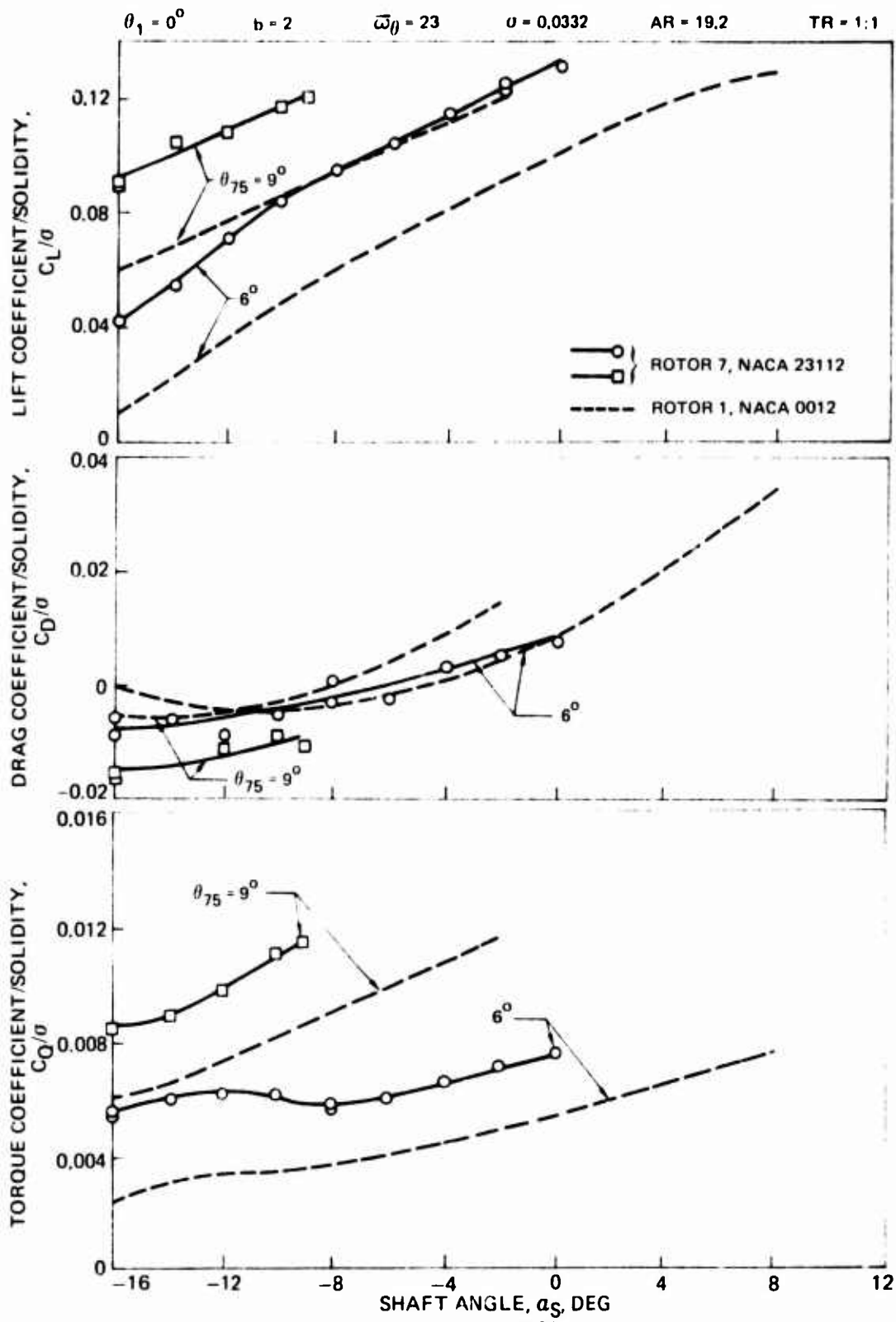


Figure 23. Continued.

$\beta_1 = 0^\circ$ $b = 2$ $\bar{\omega}\theta = 23$ $\alpha = 0.0332$ $AR = 19.2$ $TR = 1.1$

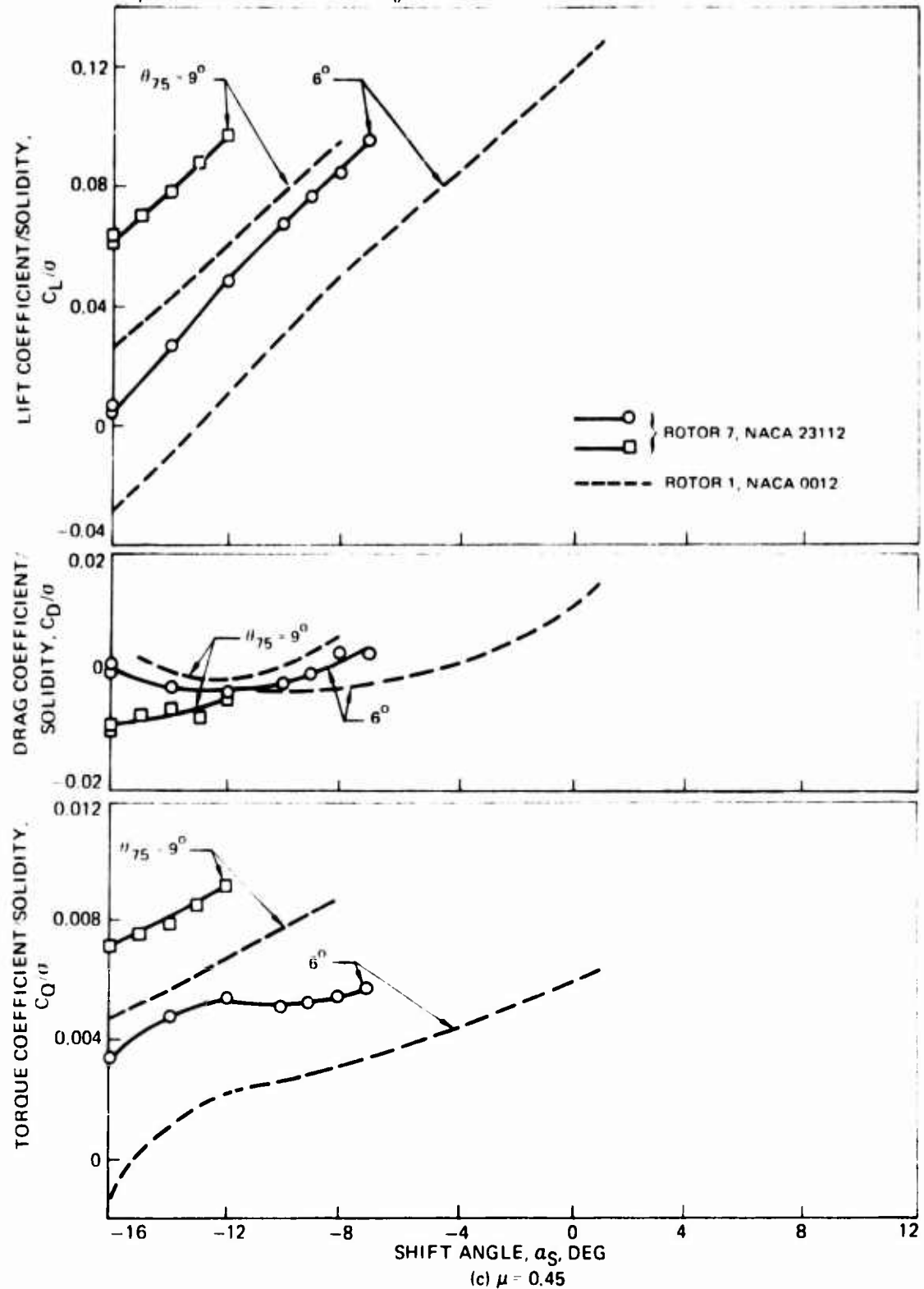


Figure 23. Concluded.

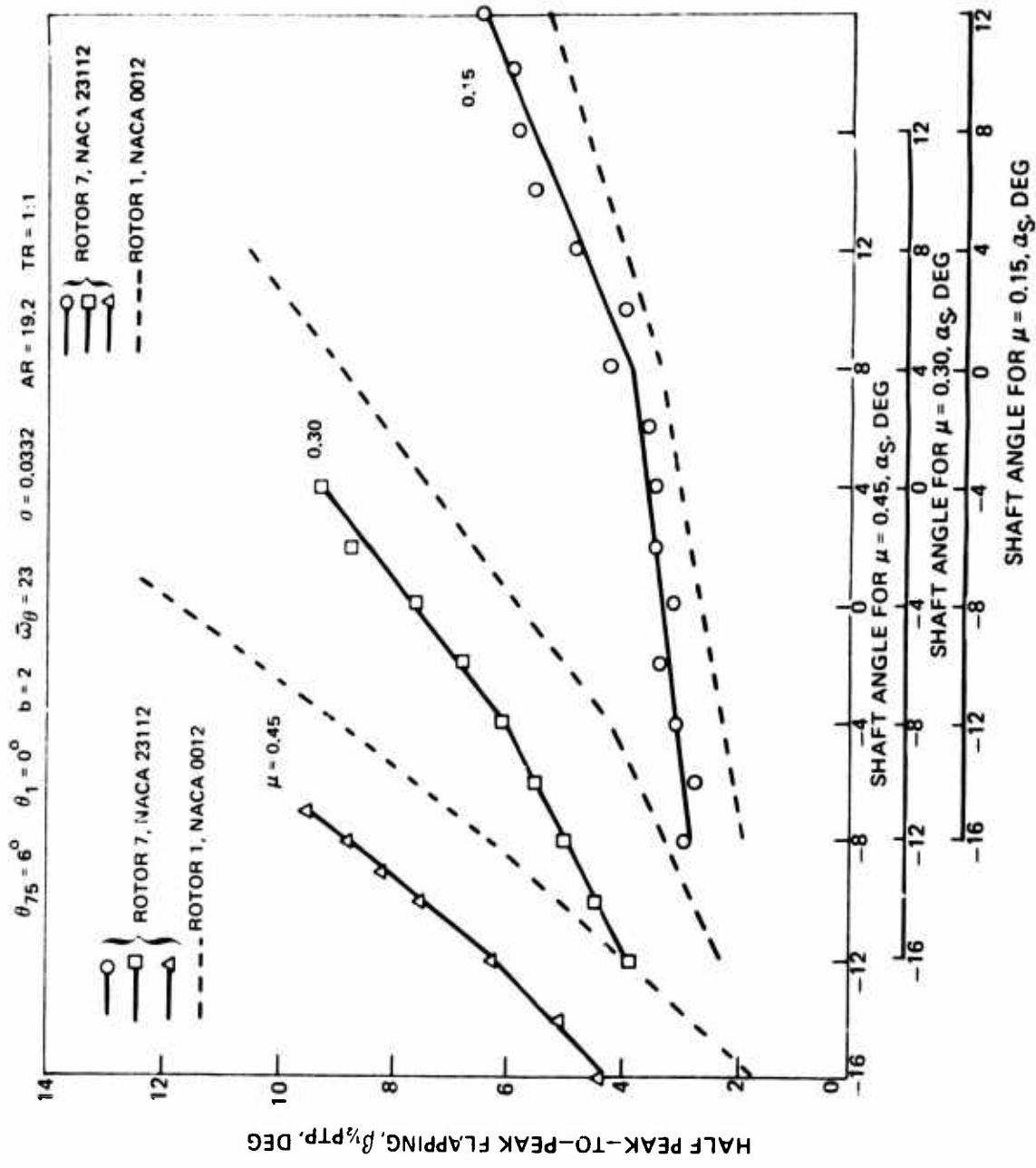


Figure 24. Effect of Blade Section Camber on Blade Flapping Response.

$\mu = 0.3$ $\theta_{75} = 6^\circ$ $\theta_1 = 0^\circ$ $\bar{\omega}_\theta = 23$ $\nu = 0.0332$ $AR = 19.2$ $TR = 1:1$

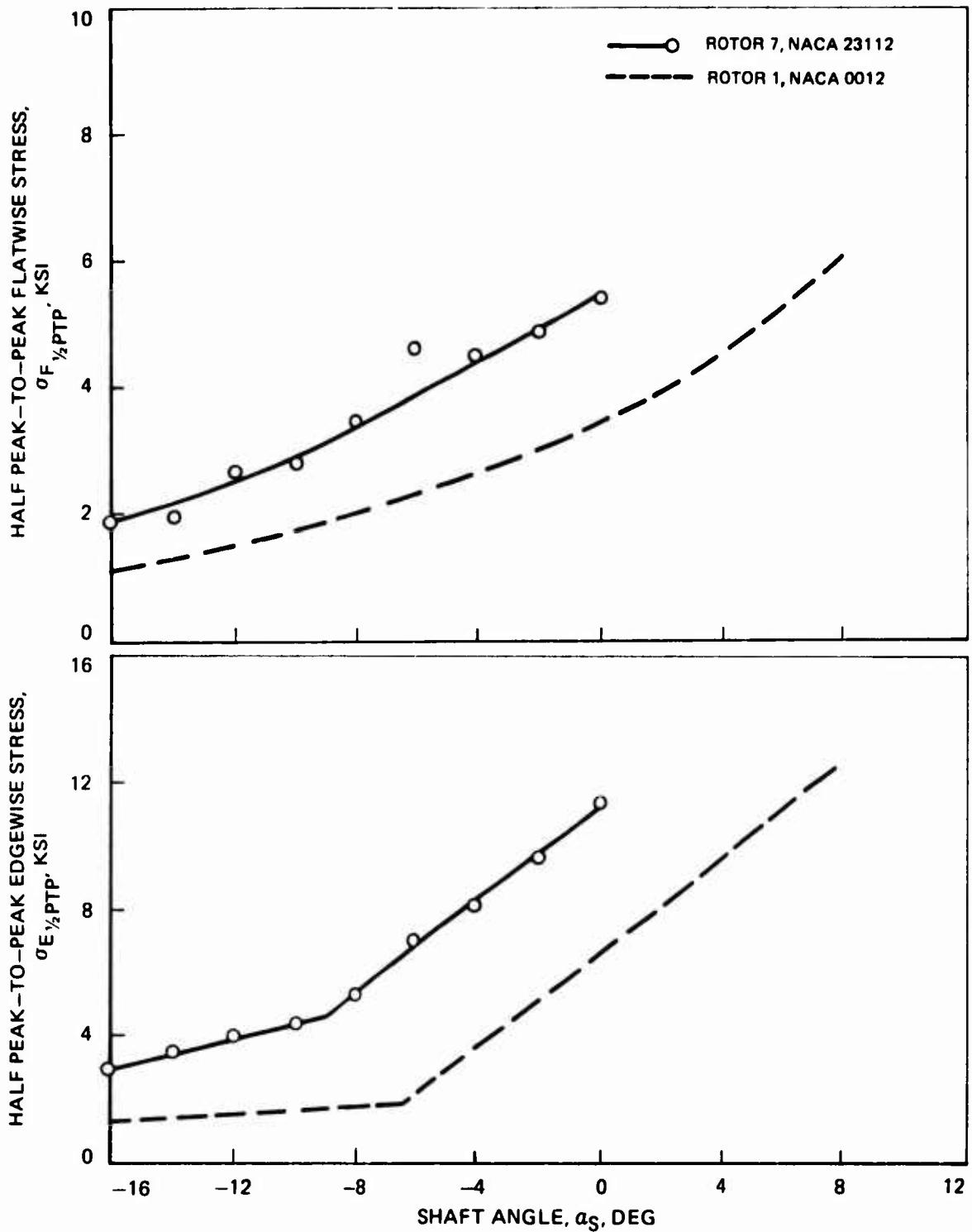


Figure 25. Effect of Blade Section Camber on Vibratory Flatwise and Edgewise Stress Data.

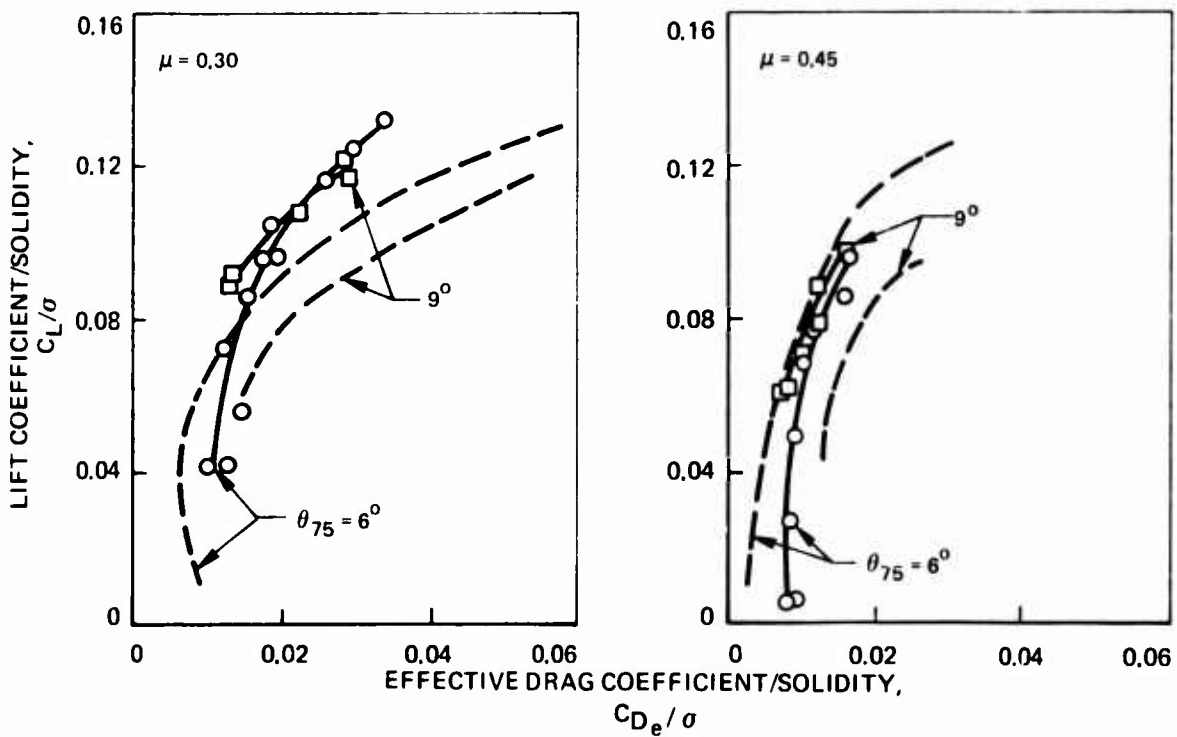
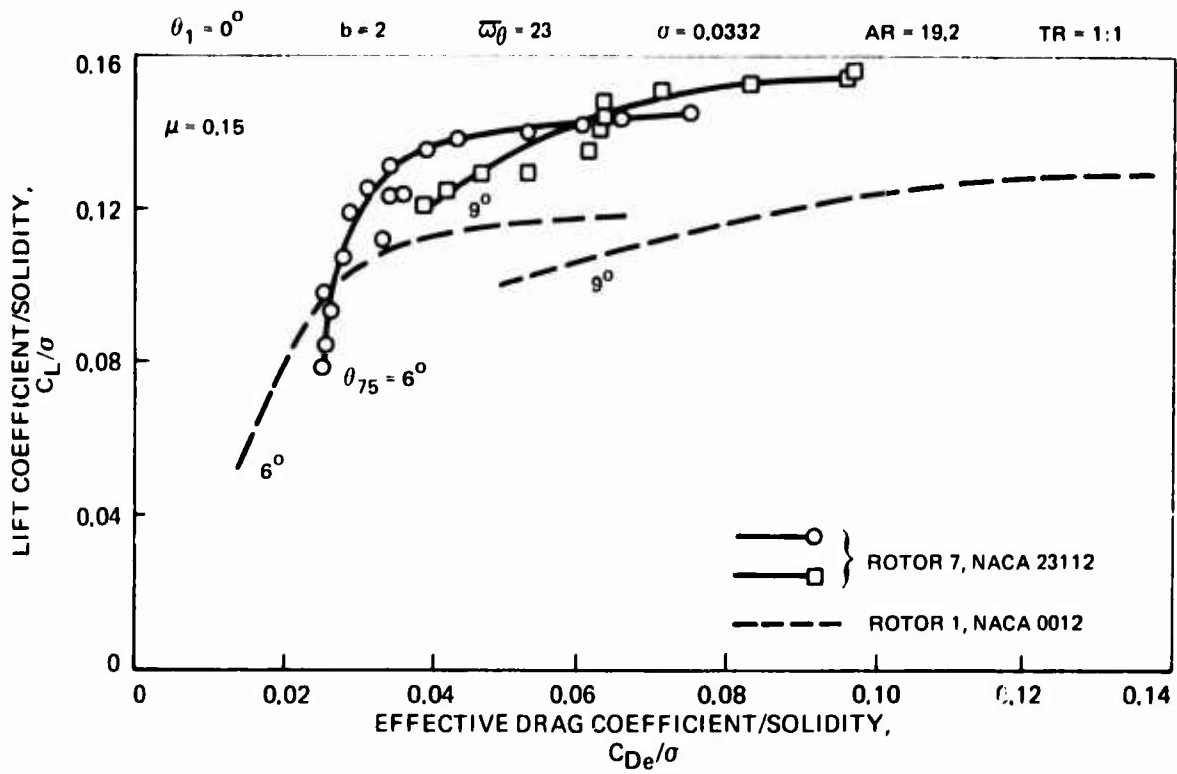


Figure 26. Effect of Blade Section Camber on Rotor Performance Compared on a Lift-Effective Drag Basis.

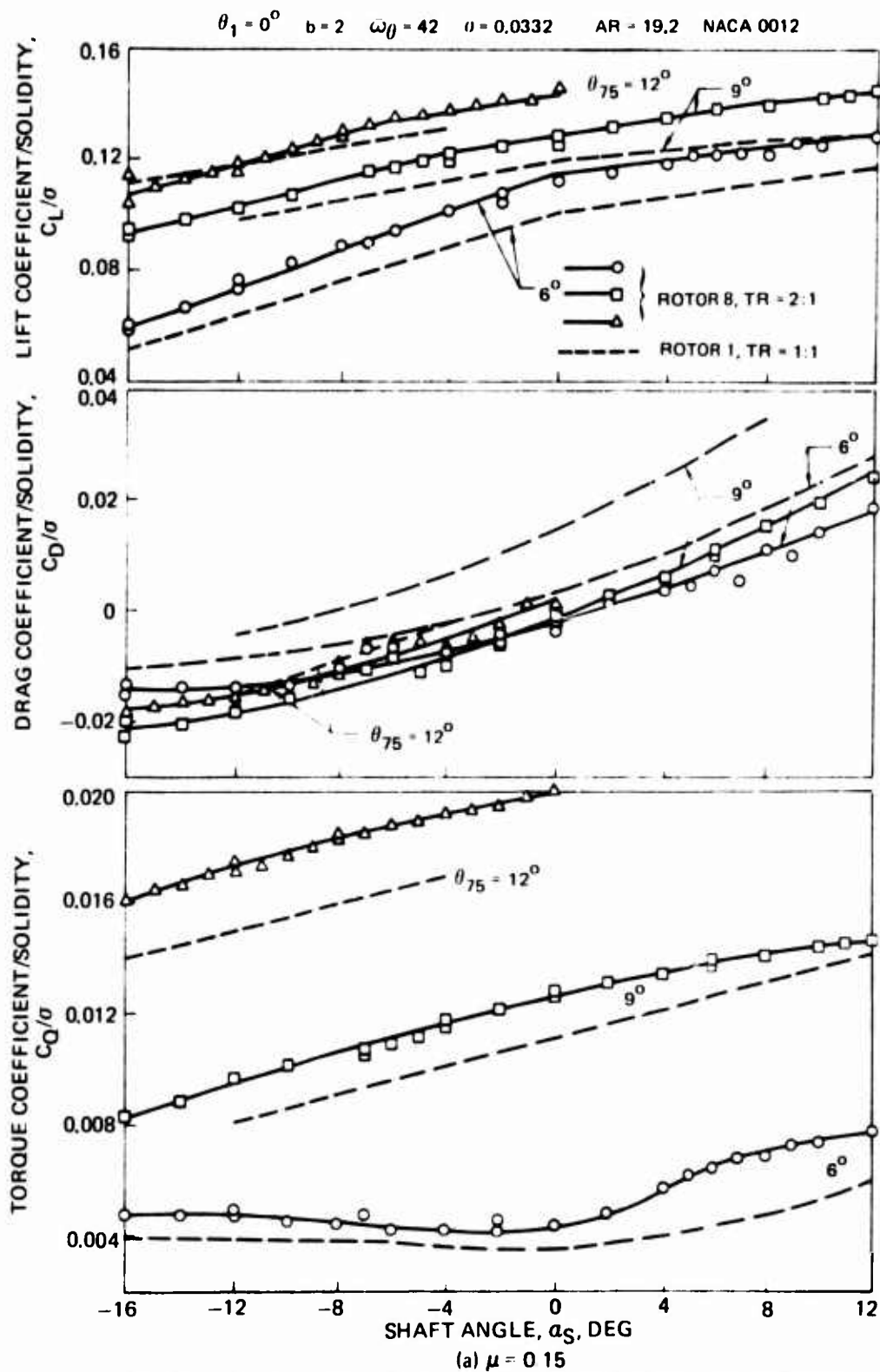


Figure 27. Effect of Taper Ratio on Rotor Performance.

$\theta_1 = 0^\circ$ $b = 2$ $\omega\theta = 42$ $\sigma = 0.0332$ $AR = 19.2$ $NACA\ 0012$

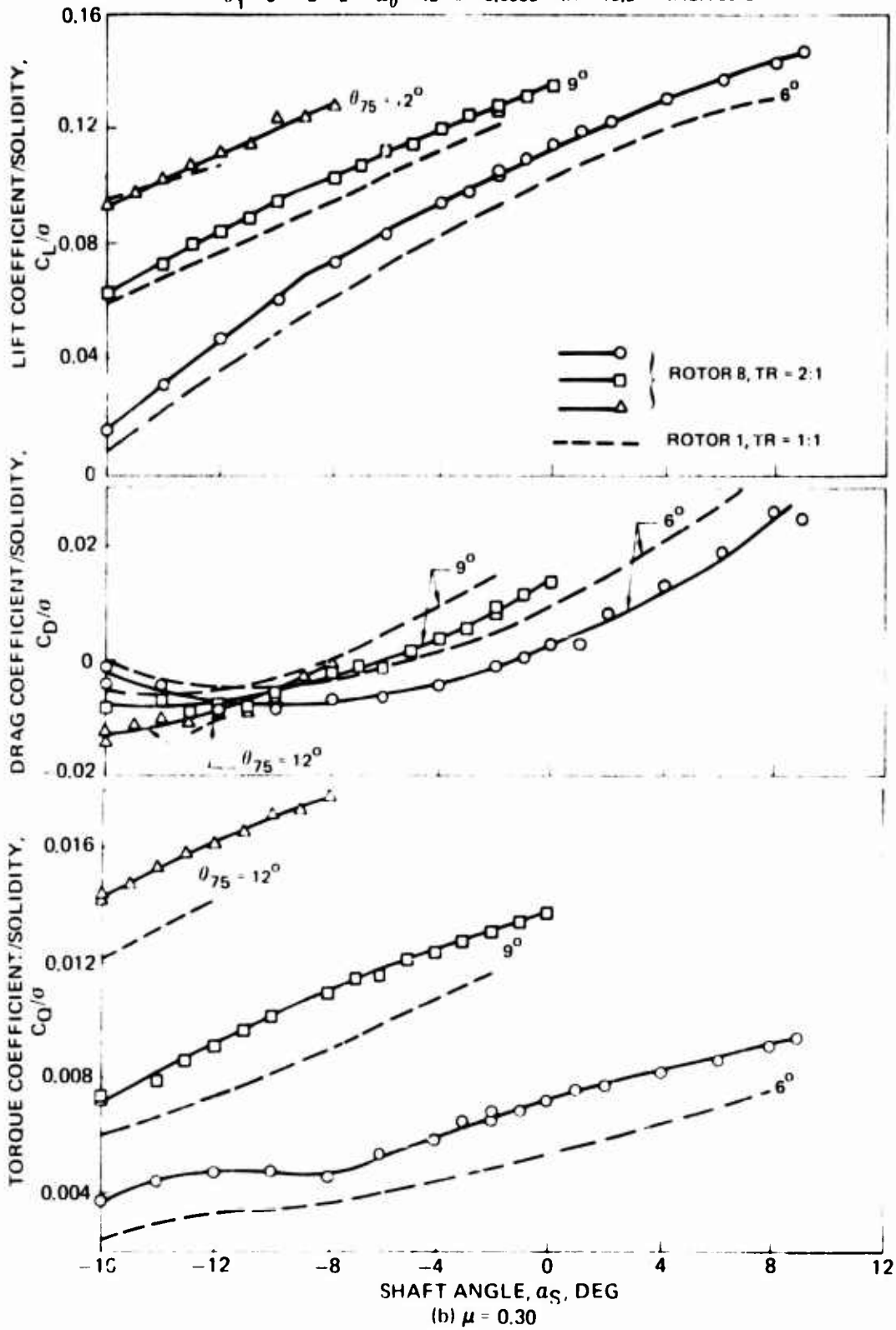


Figure 27. Continued.

$\theta_1 = 0^\circ$ $b = 2$ $\bar{\omega}_\theta = 42$ $\sigma = 0.0332$ $AR = 19.2$ $NACA 0012$

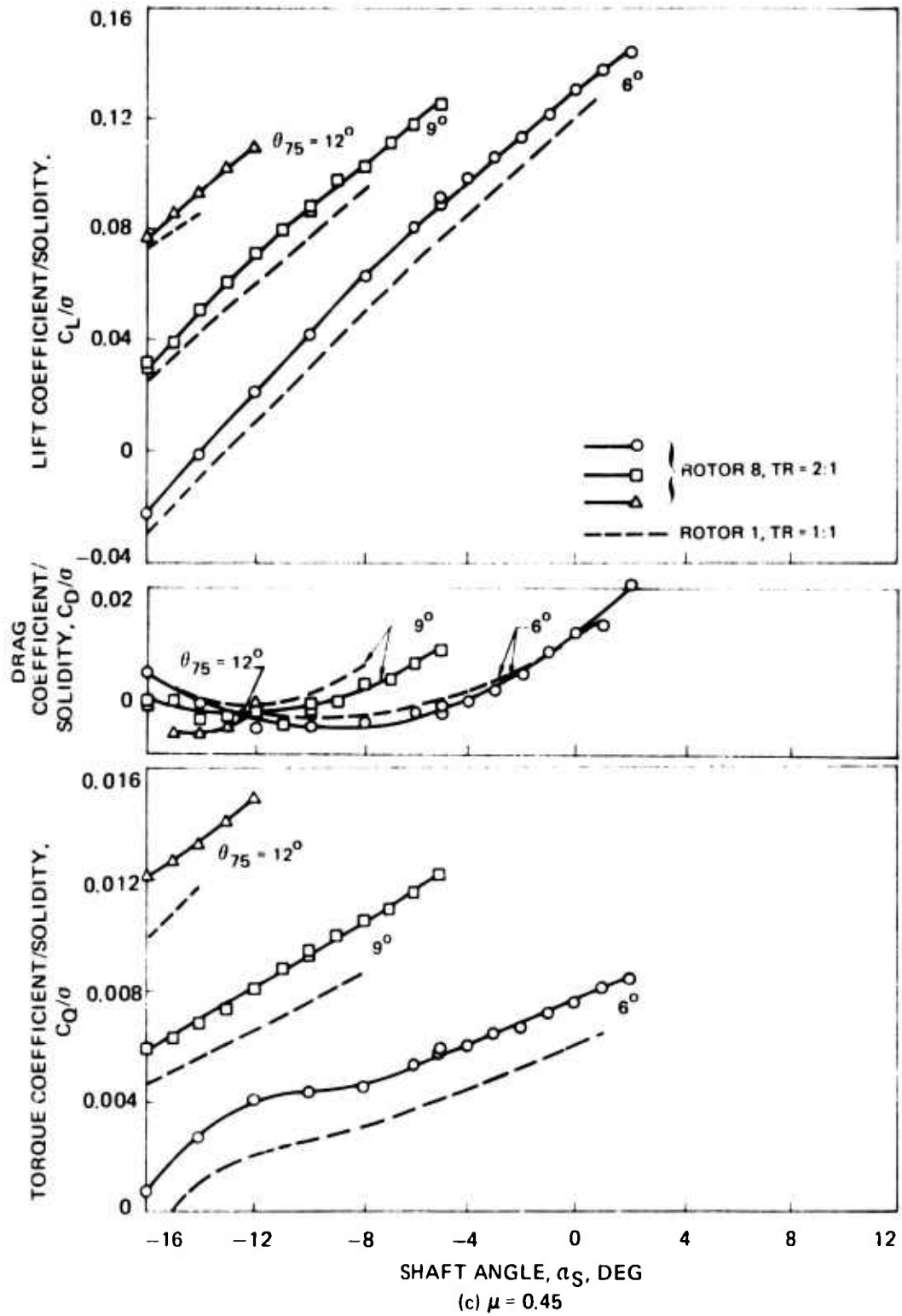


Figure 27. Concluded.

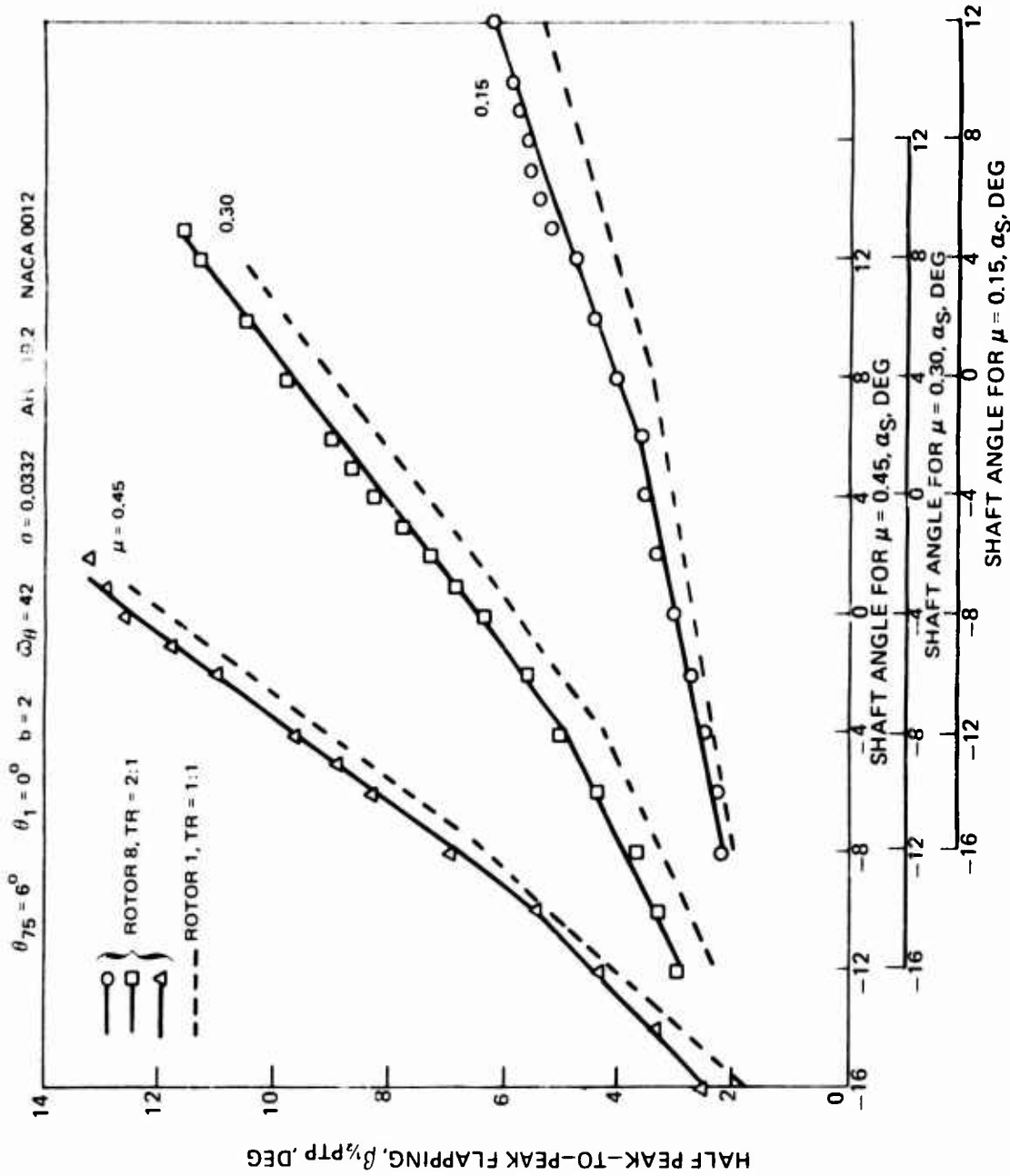


Figure 28. Effect of Taper Ratio on Blade Flapping Response.

$\mu = 0.3$ $\theta_{75} = 6^\circ$ $\theta_1 = 0^\circ$ $b = 2$ $\bar{\omega}_\theta = 42$ $\nu = 0.0332$ $AR = 19.2$ $NACA\ 0012$

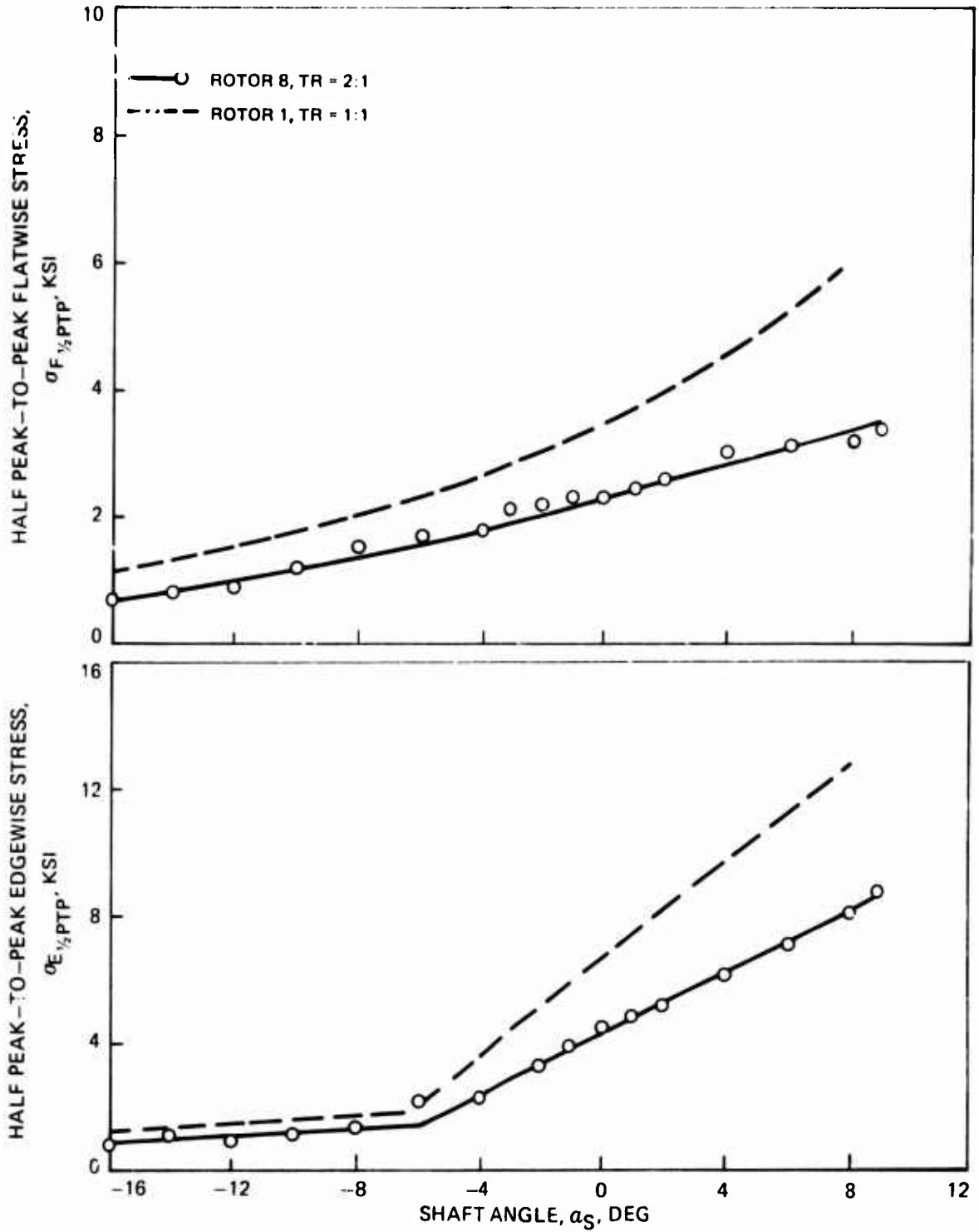


Figure 29. Effect of Taper Ratio on Vibratory Flatwise and Edgewise Stress.

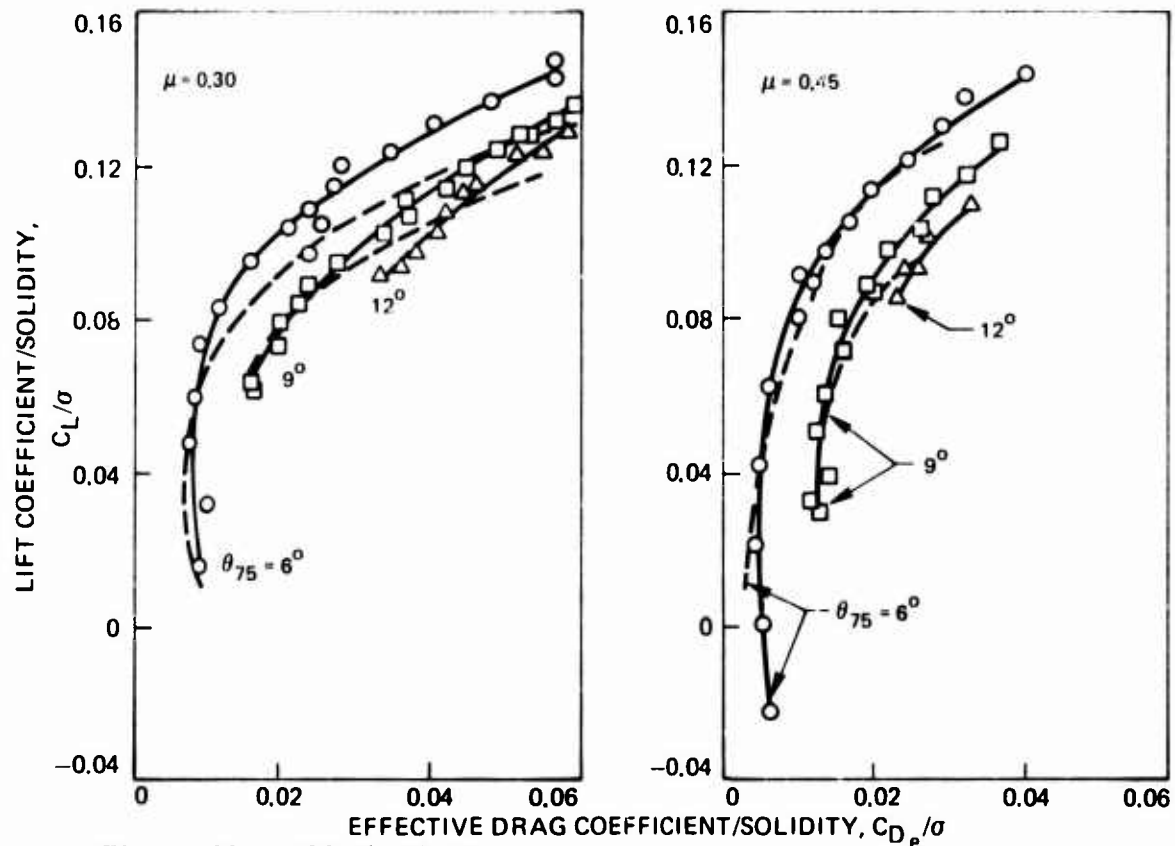
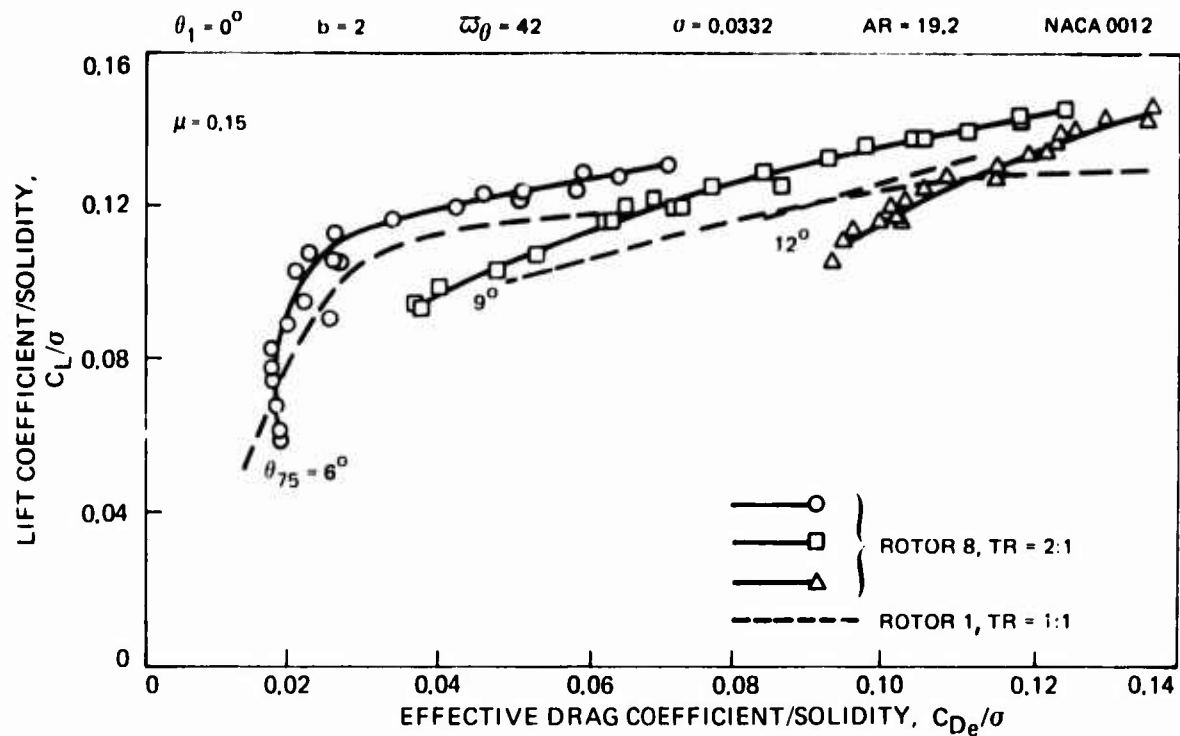


Figure 30. Effect of Taper Ratio on Rotor Performance Compared on a Lift-Effective Drag Basis.

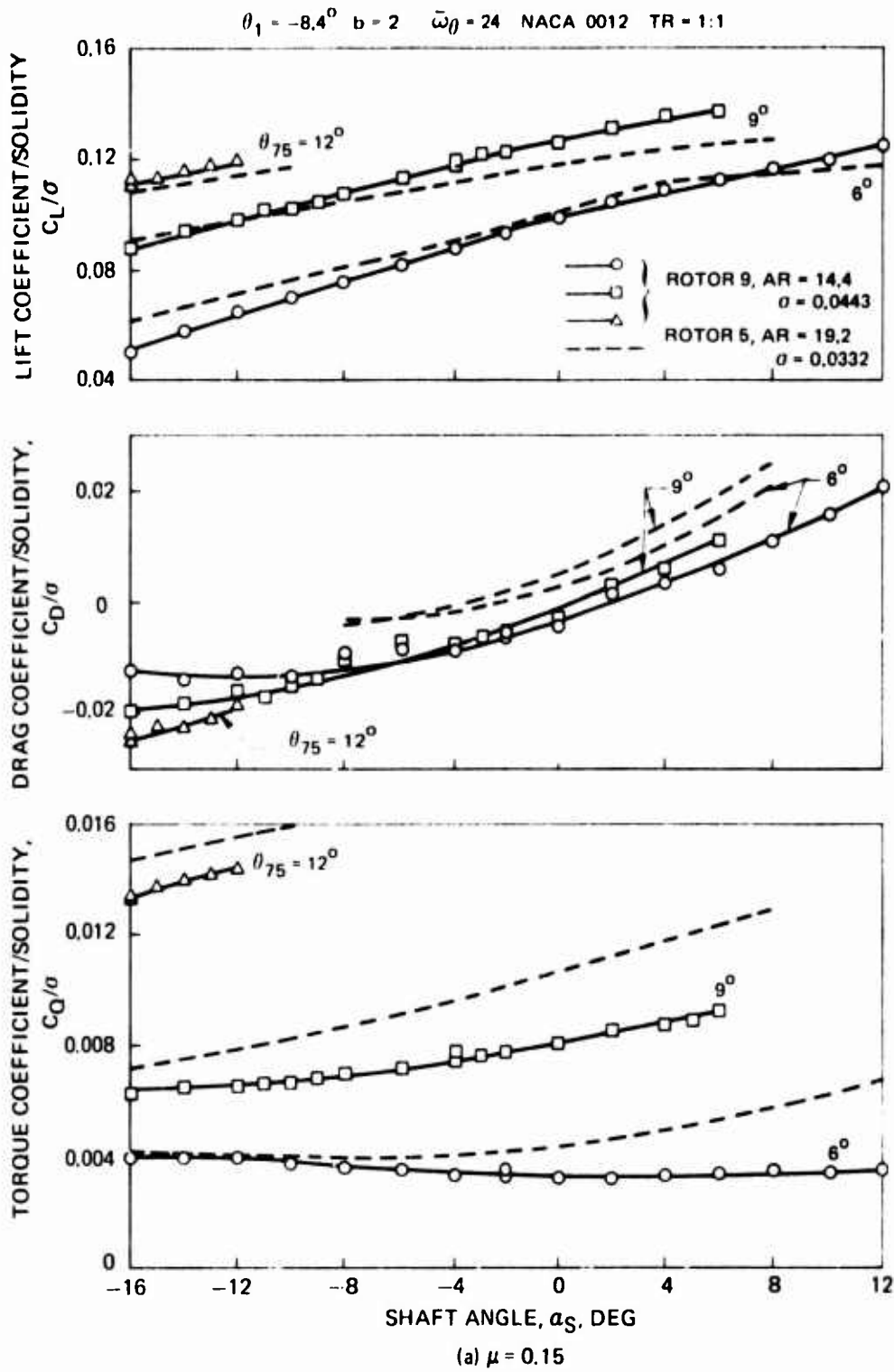


Figure 31. Effect of Aspect Ratio on Rotor Performance.

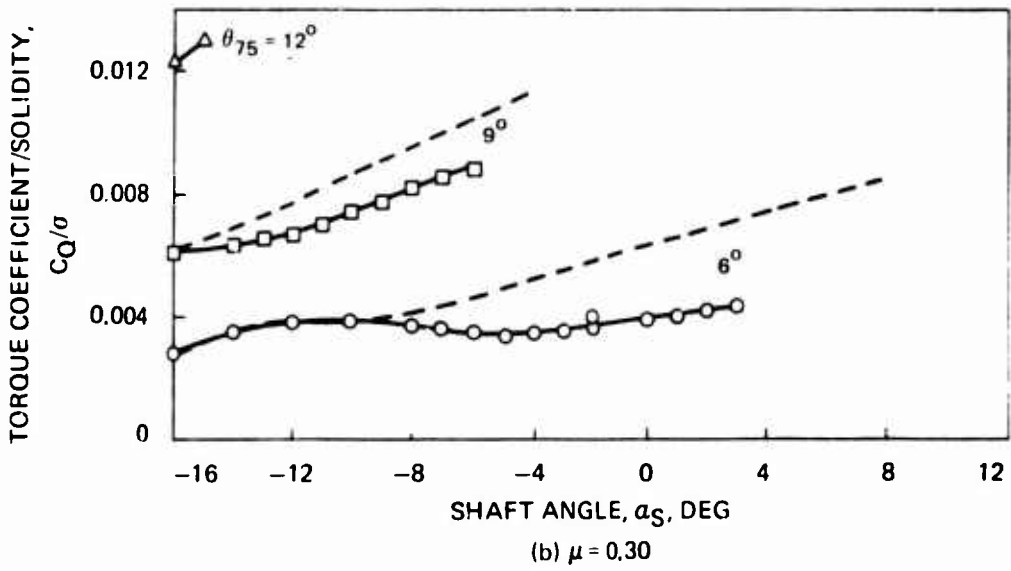
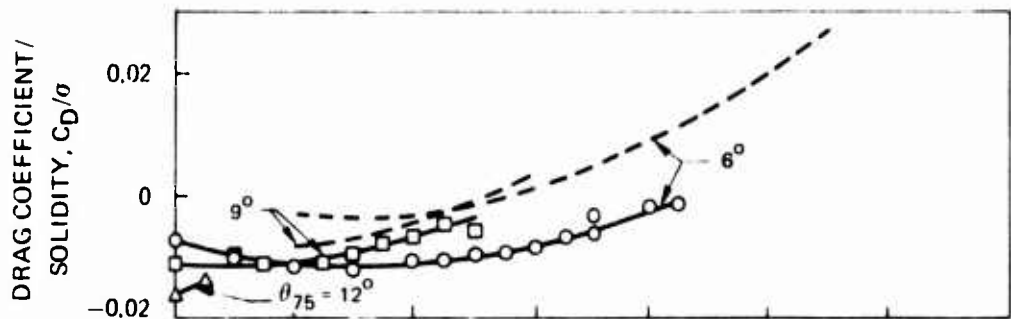
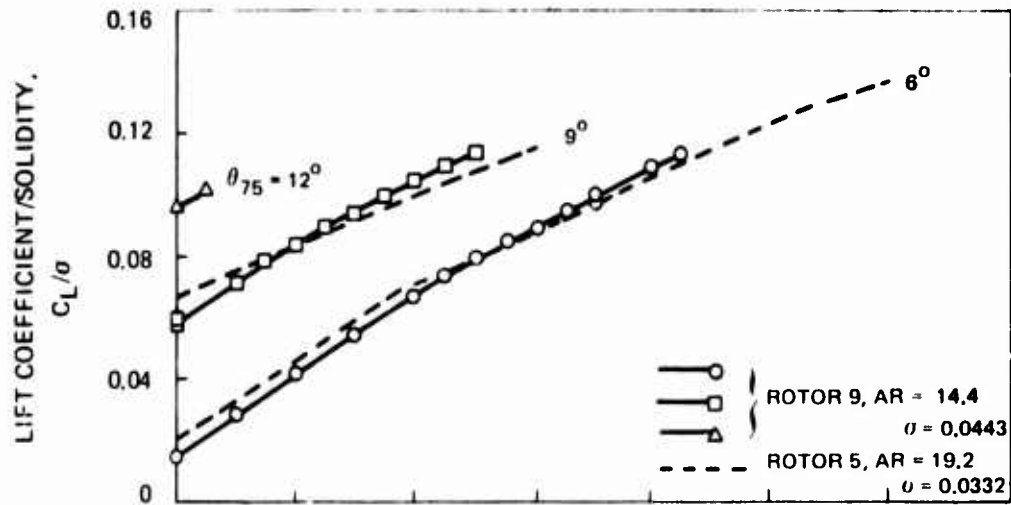


Figure 31. Continued.

$\theta_1 = -8.4^\circ$ $b = 2$ $\bar{\omega} = 24$ NACA 0012 TR = 1:1

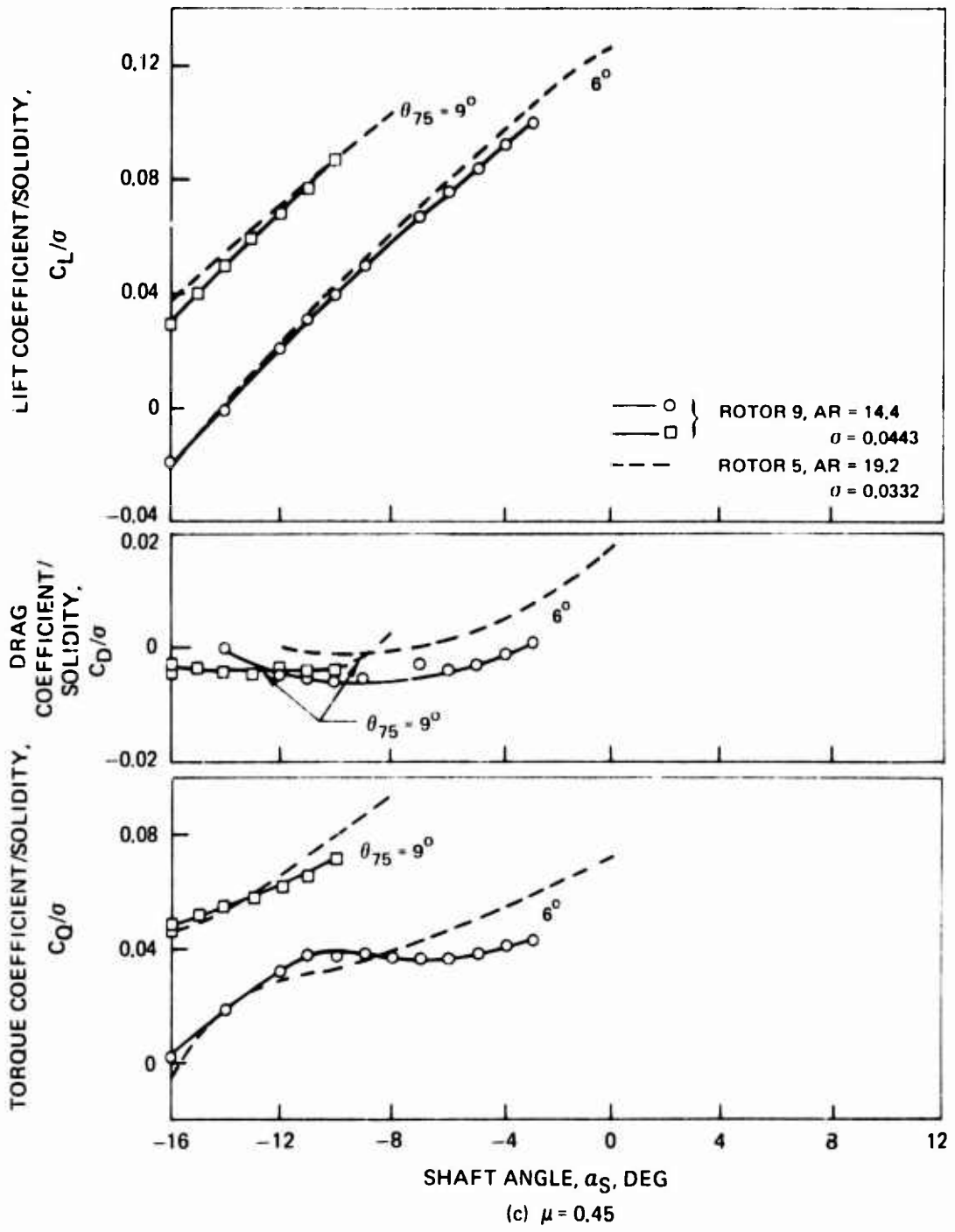


Figure 31. Concluded.

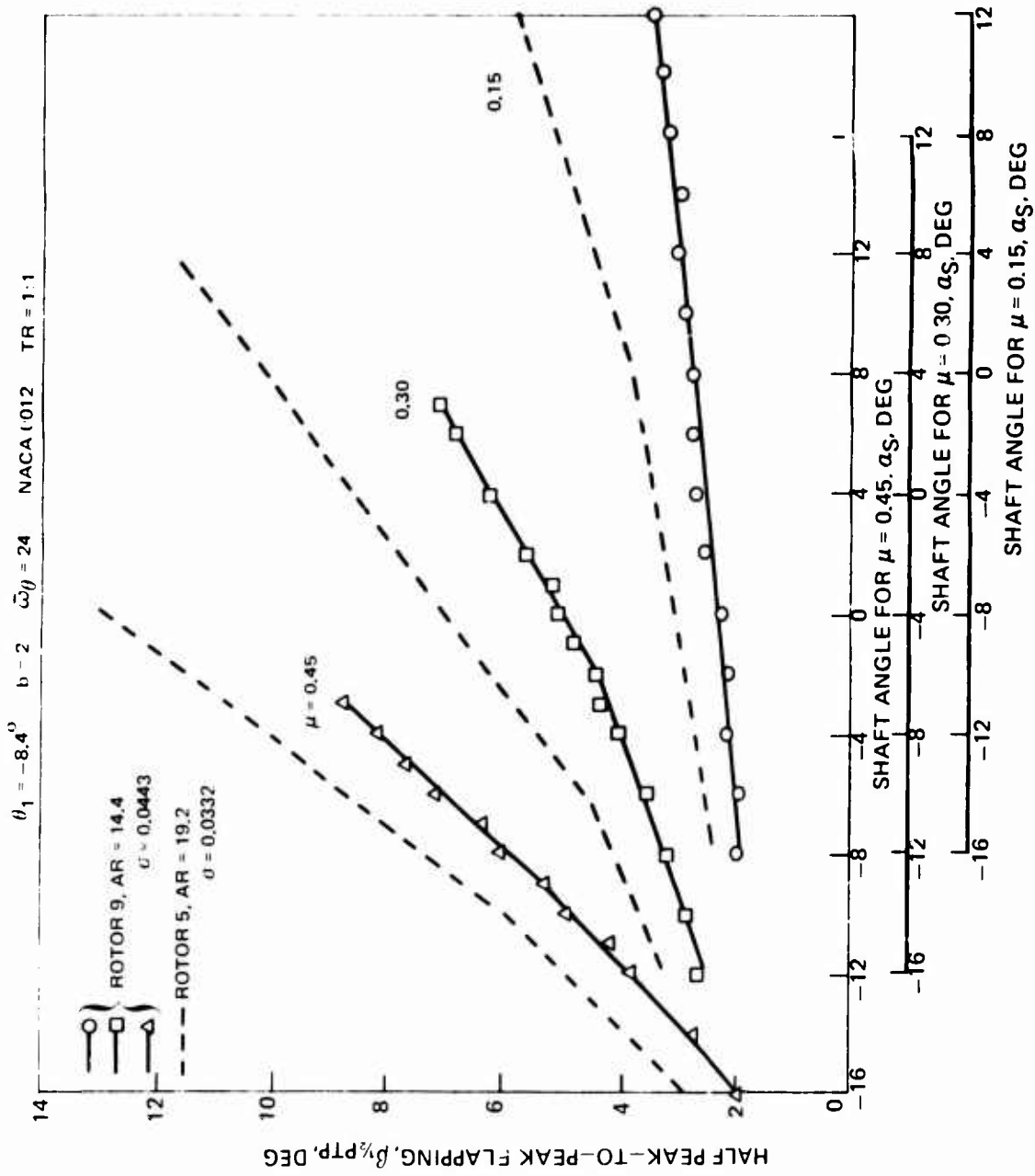


Figure 32. Effect of Aspect Ratio on Blade Flapping Response.

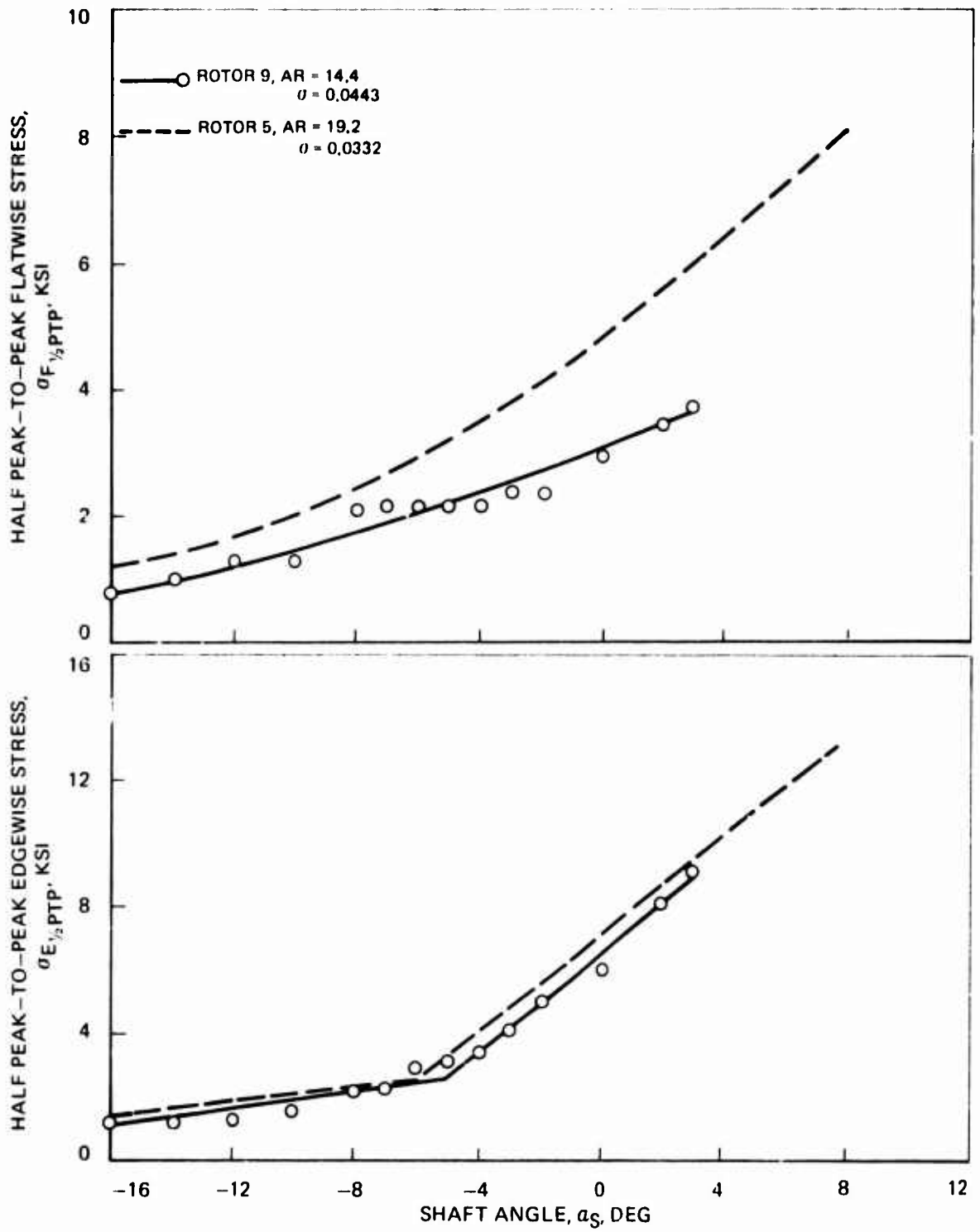


Figure 33. Effect of Aspect Ratio on Vibratory Flatwise and Edgewise Stress.

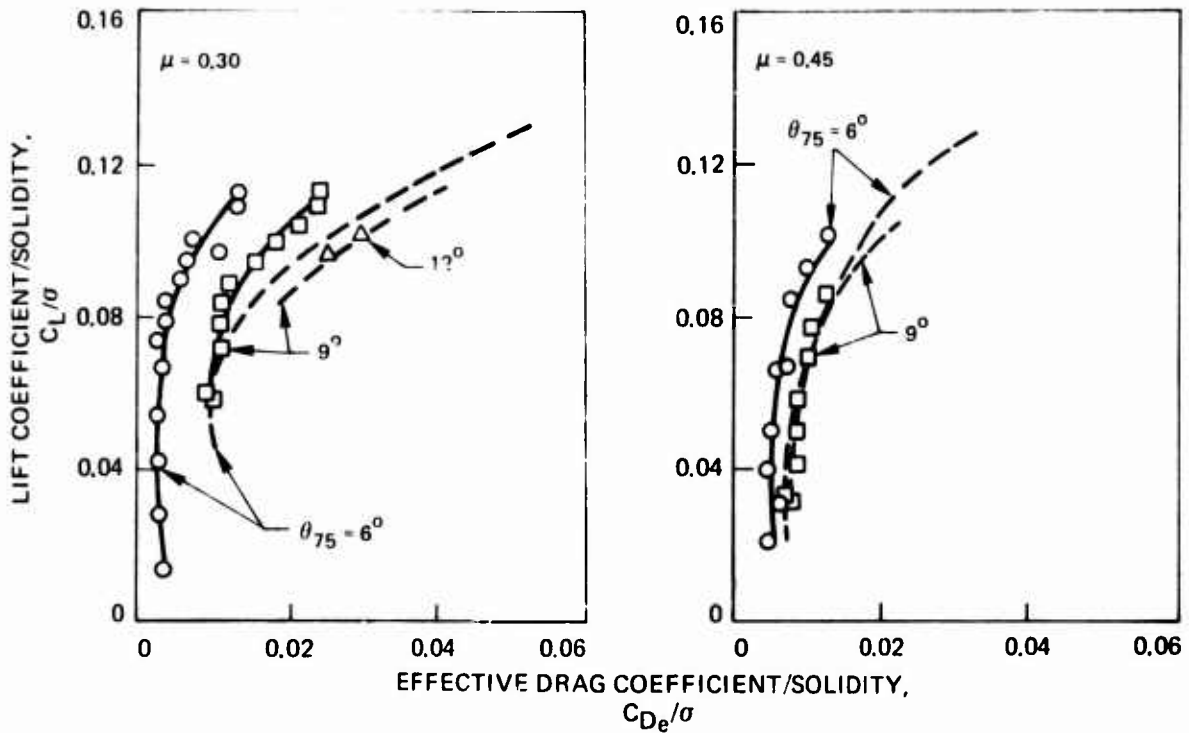
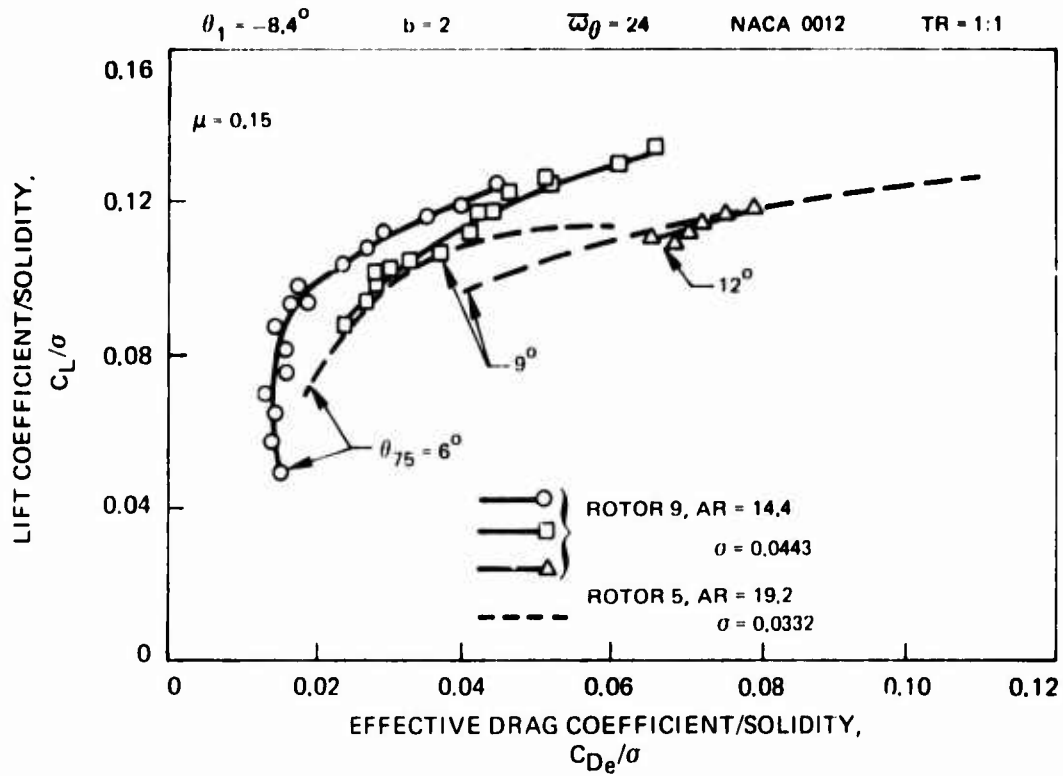


Figure 34. Effect of Aspect Ratio on Rotor Performance Compared on a Lift-Effective Drag Basis.

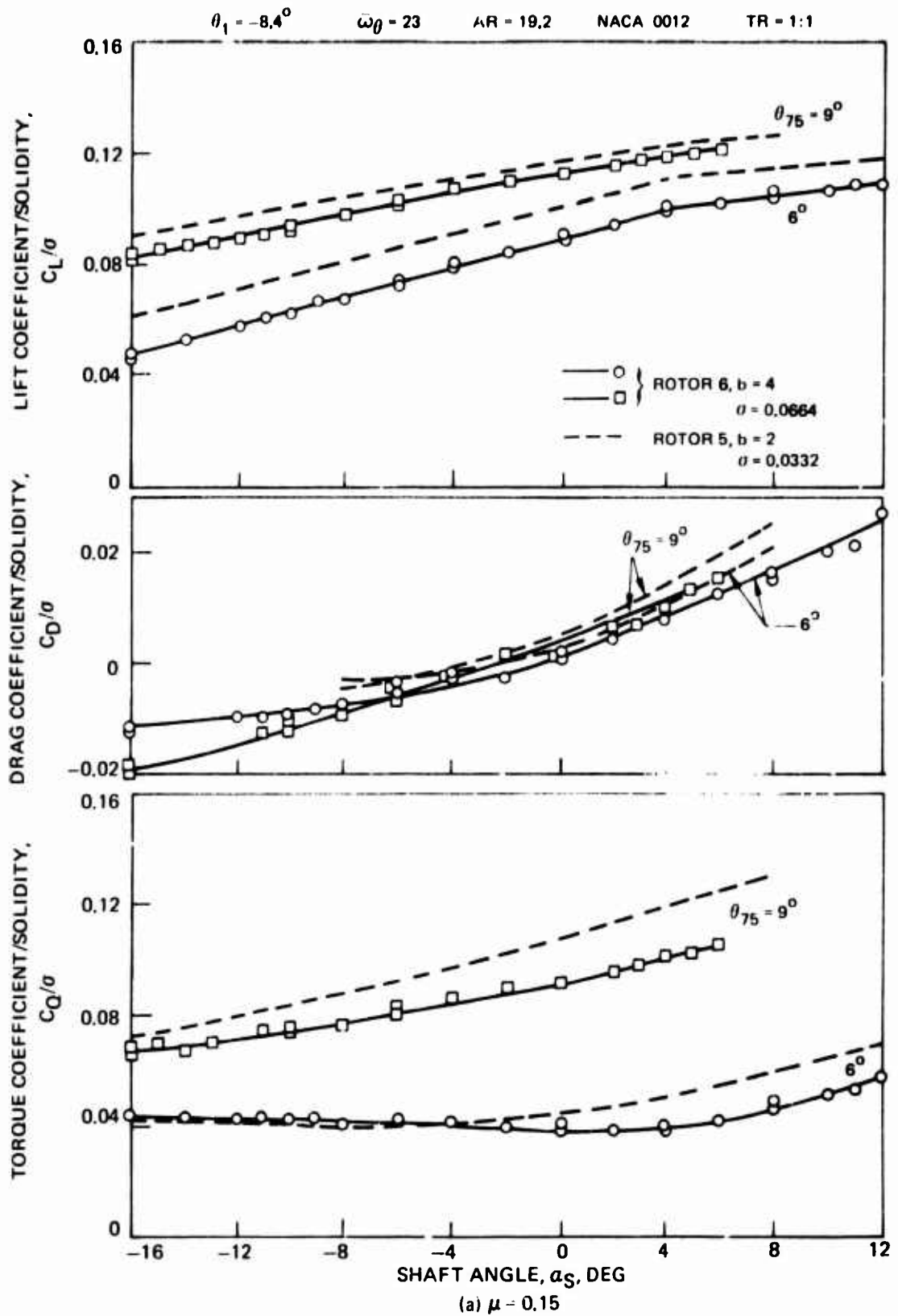


Figure 35. Effect of Number of Blades on Rotor Performance.

$\theta_1 = -8.4^\circ$ $\omega_0 = 23$ AR = 19.2 NACA 0012 TR = 1:1

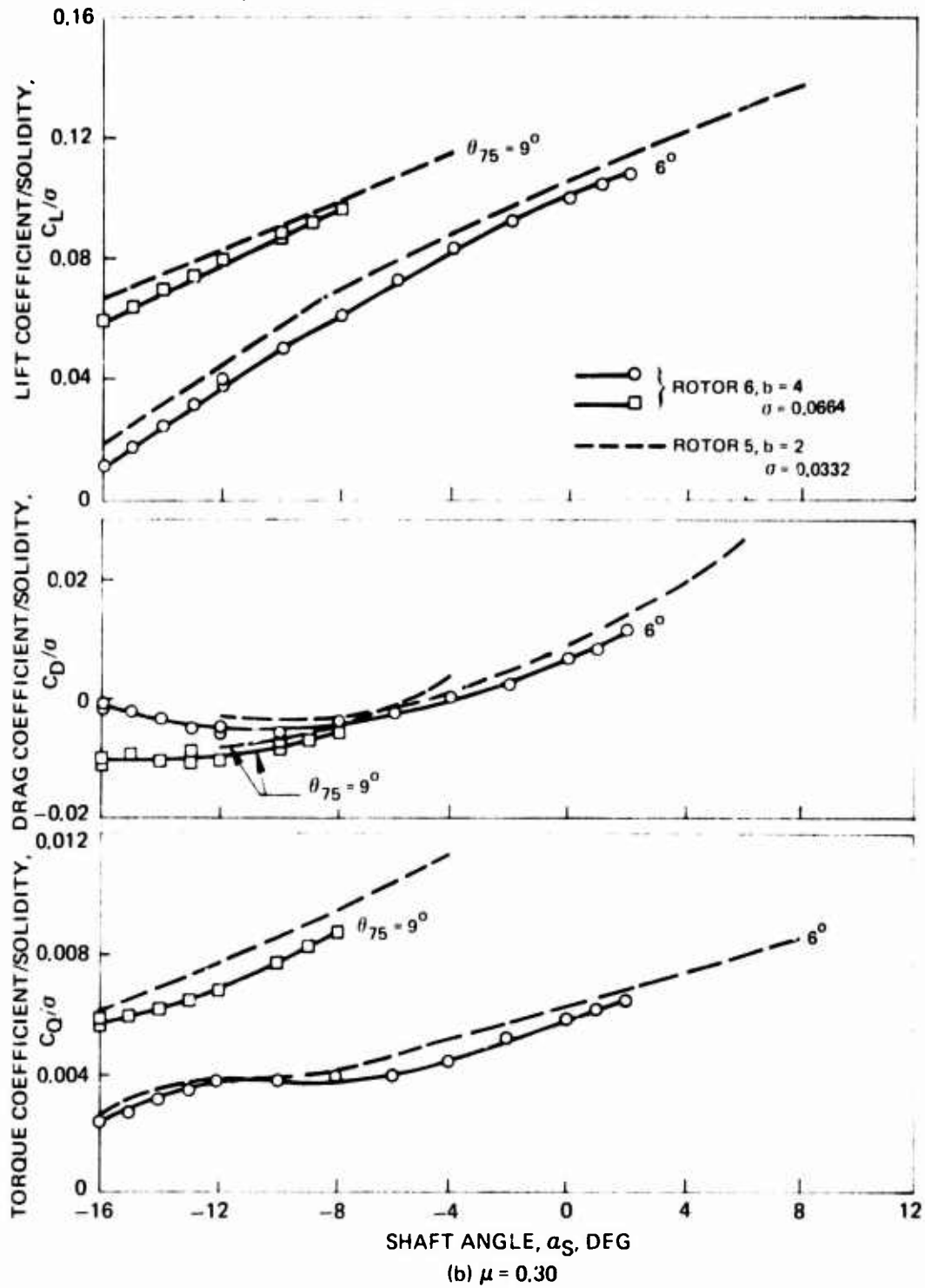


Figure 35. Continued.

$\theta_1 = -8.4^\circ$

$\bar{\omega}_\theta = 23$

AR = 19.2

NACA 0012

TR = 1:1

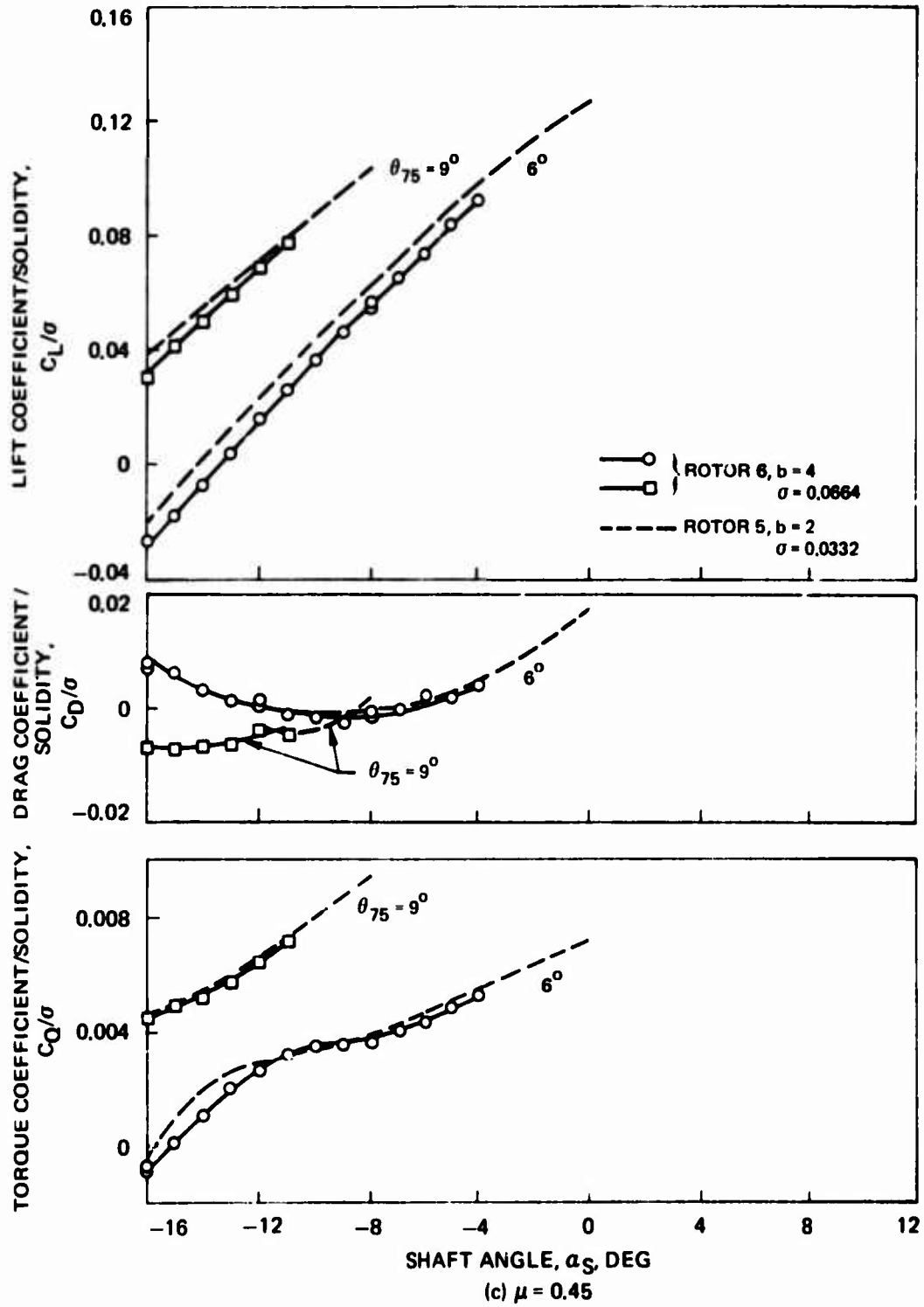


Figure 35. Concluded.

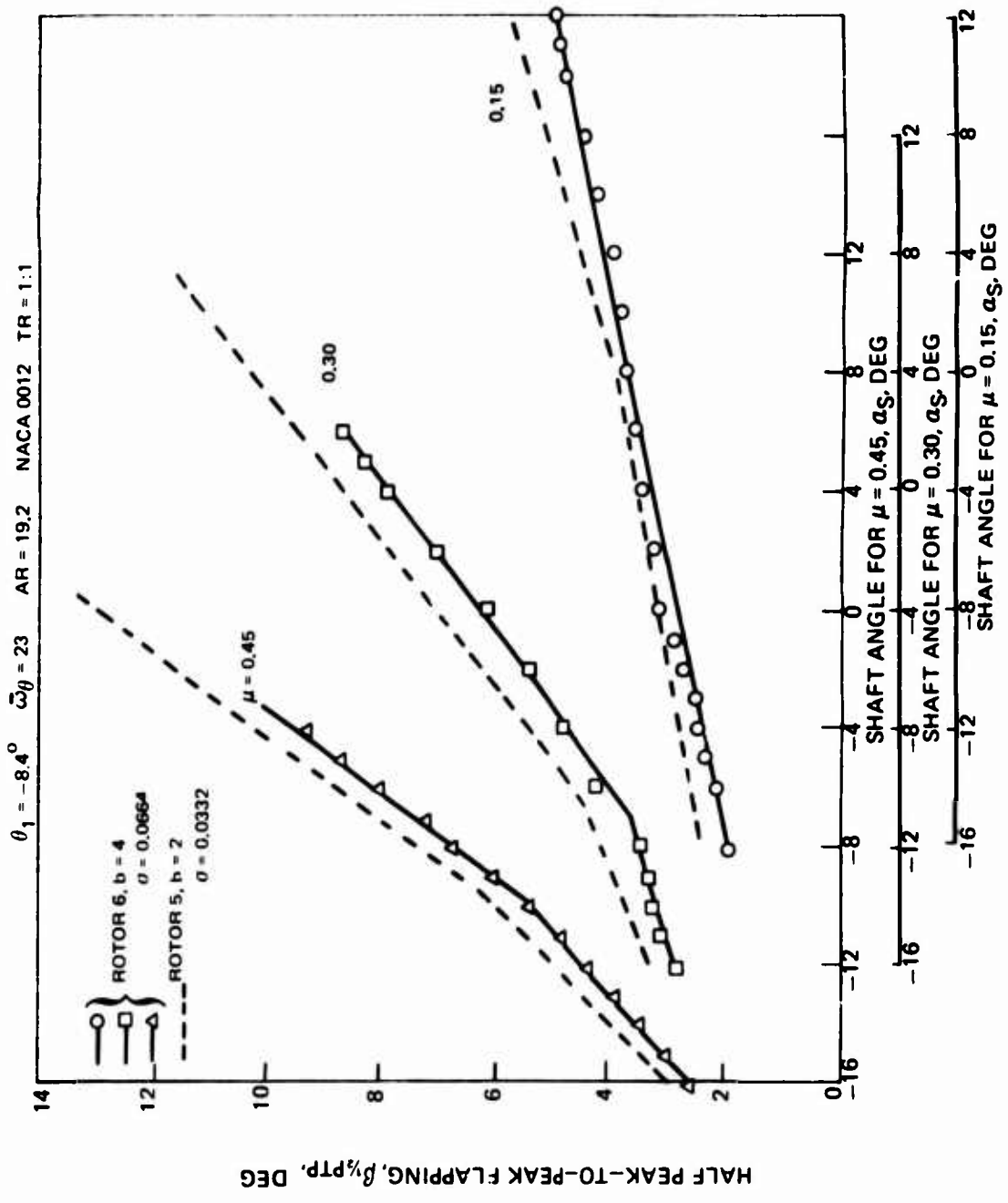


Figure 36. Effect of Number of Blades on Blade Flapping Response.

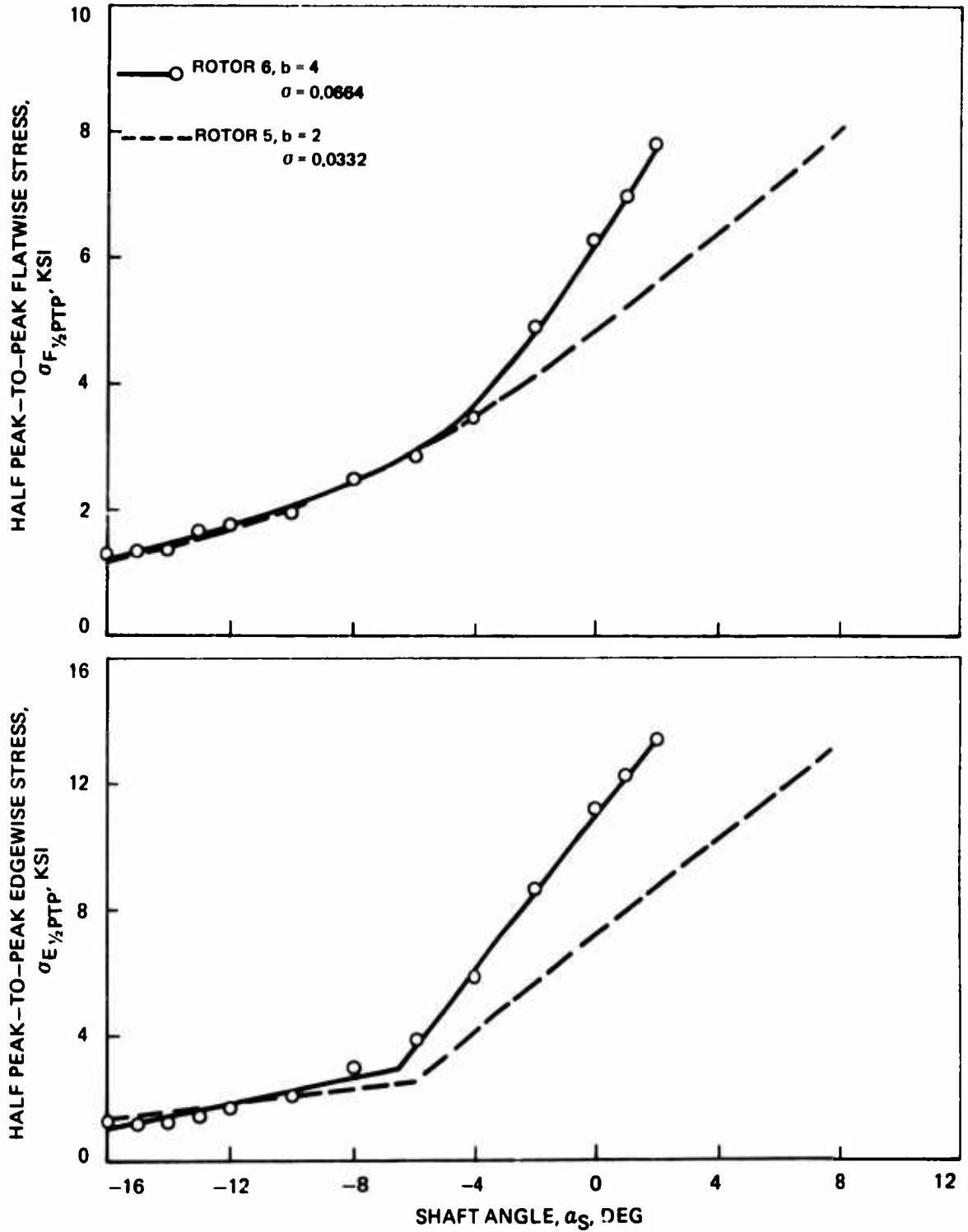


Figure 37. Effect of Number of Blades on Vibratory Flatwise and Edgewise Stress.

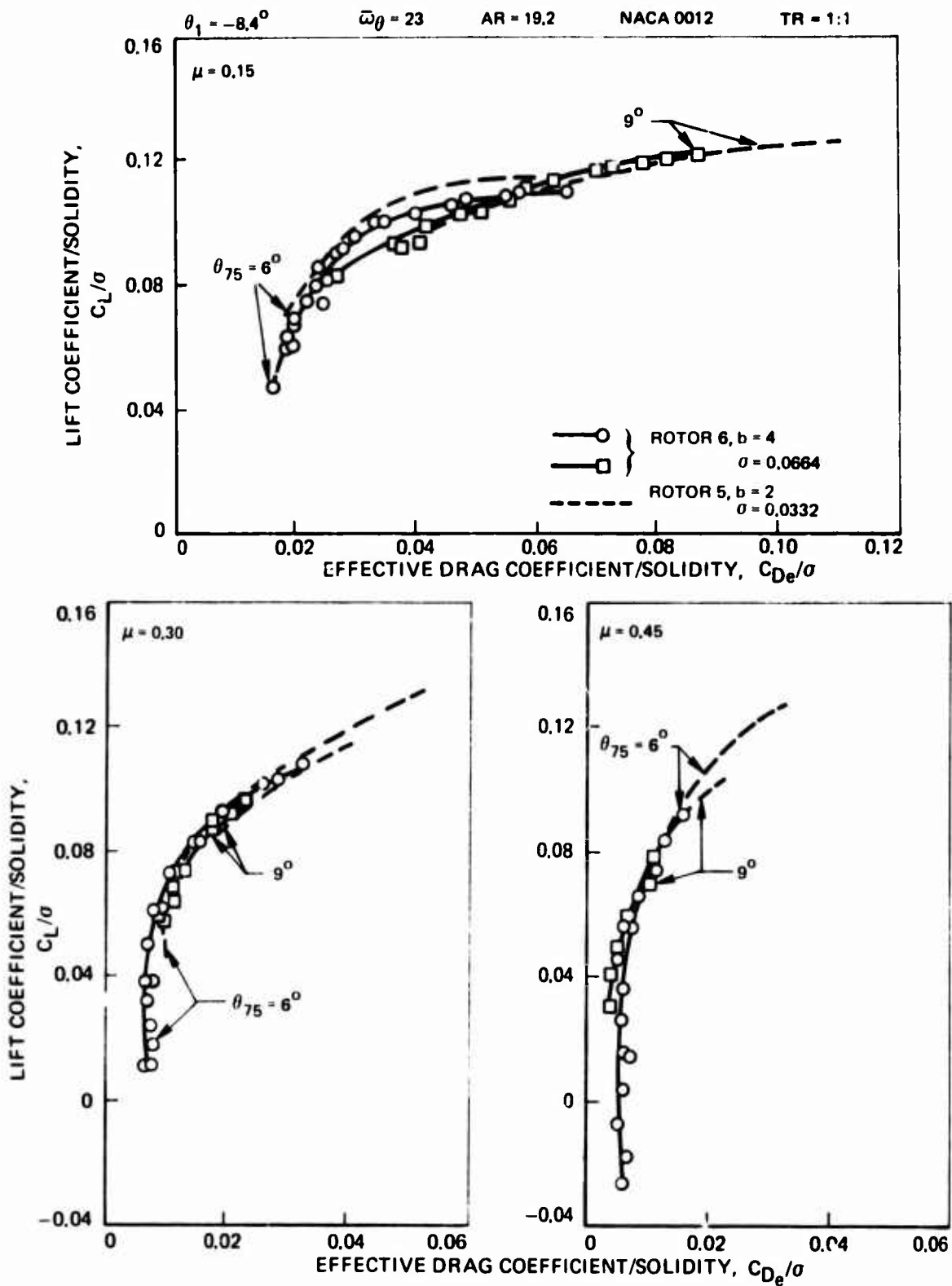


Figure 38. Effect of Number of Blades on Rotor Performance Compared on a Lift-Effective Drag Basis.

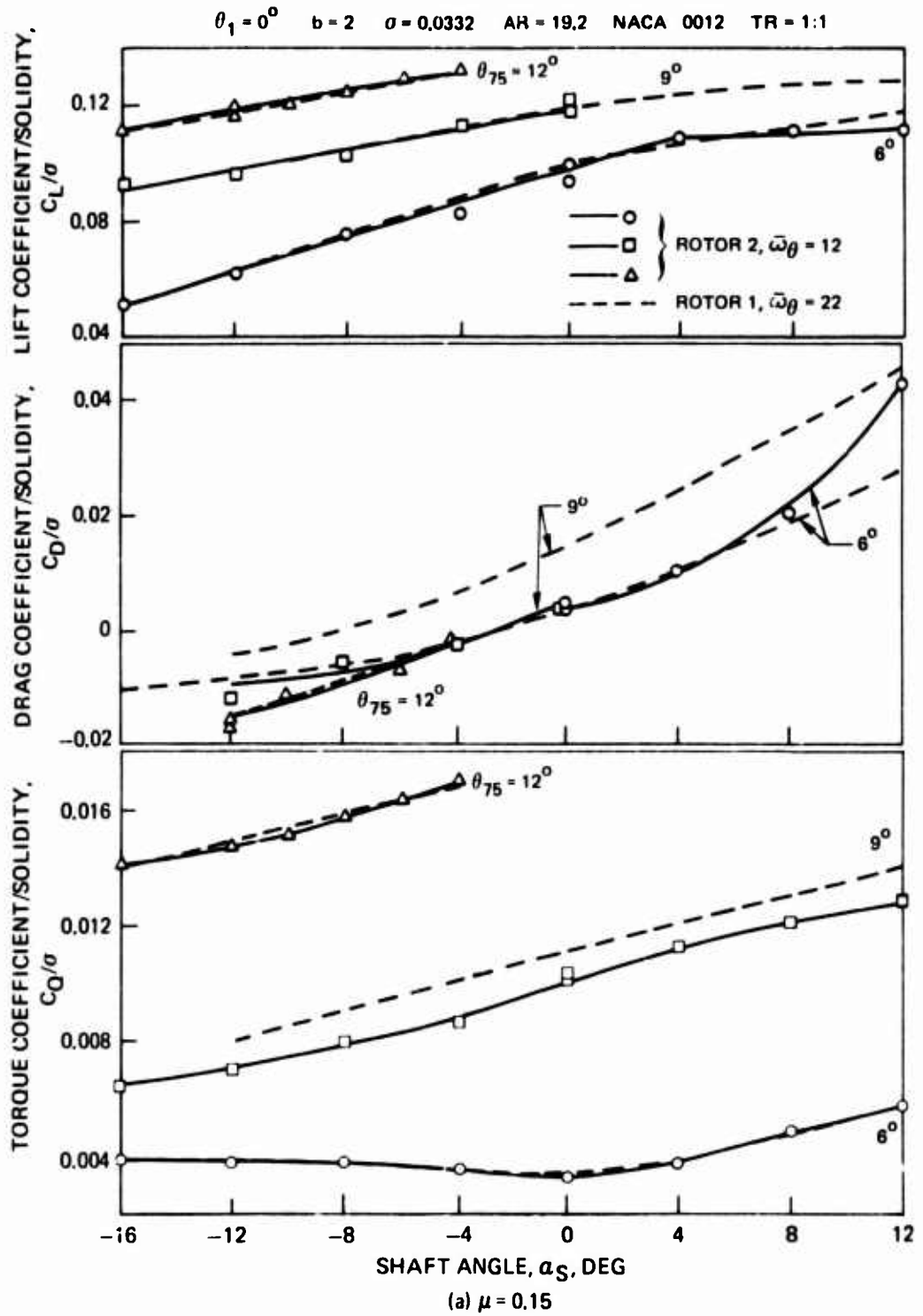
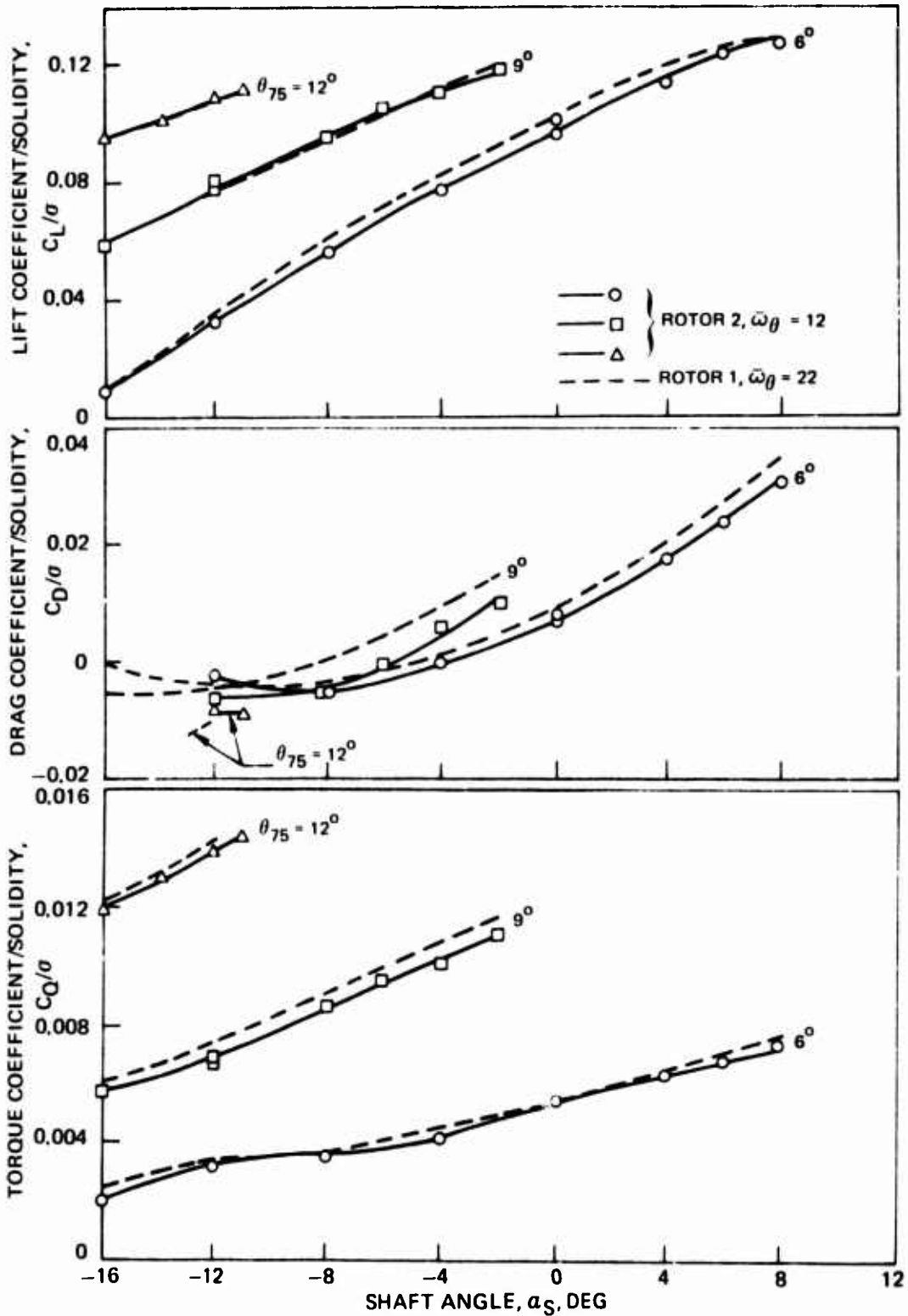


Figure 39. Effect of Torsional Frequency on Rotor Performance - $\bar{\omega}_\theta = 12$.



(b) $\mu = 0.30$
Figure 39. Continued.

$\theta_1 = 0^\circ$ $b = 2$ $\sigma = 0.0332$ $AR = 19.2$ $NACA\ 0012$ $TR = 1:1$

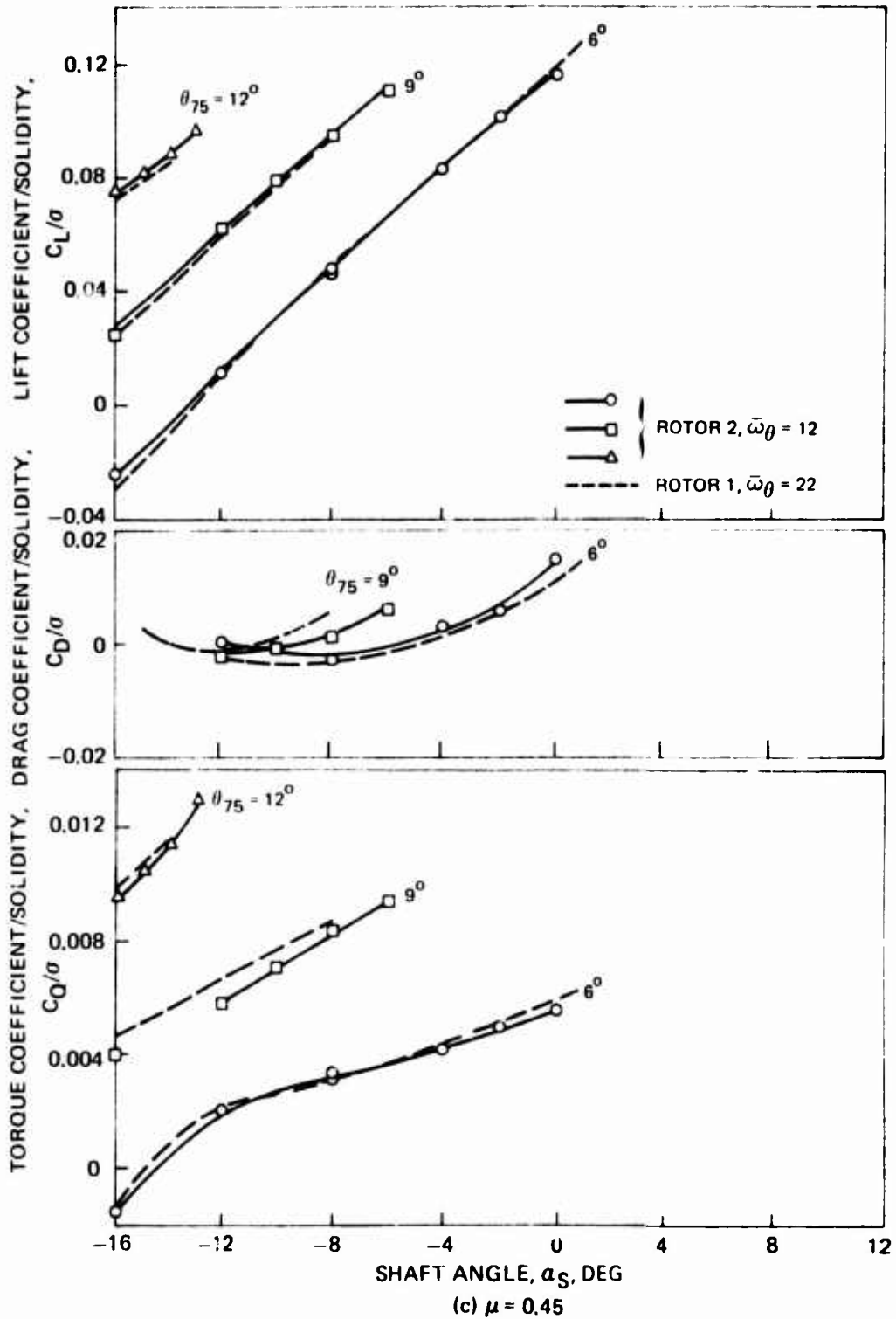


Figure 39. Concluded.

$\theta_1 = 0^\circ$ $b = 2$ $\sigma = 0.0332$ $AR = 19.2$ $NACA\ 0012$ $TR = 1:1$

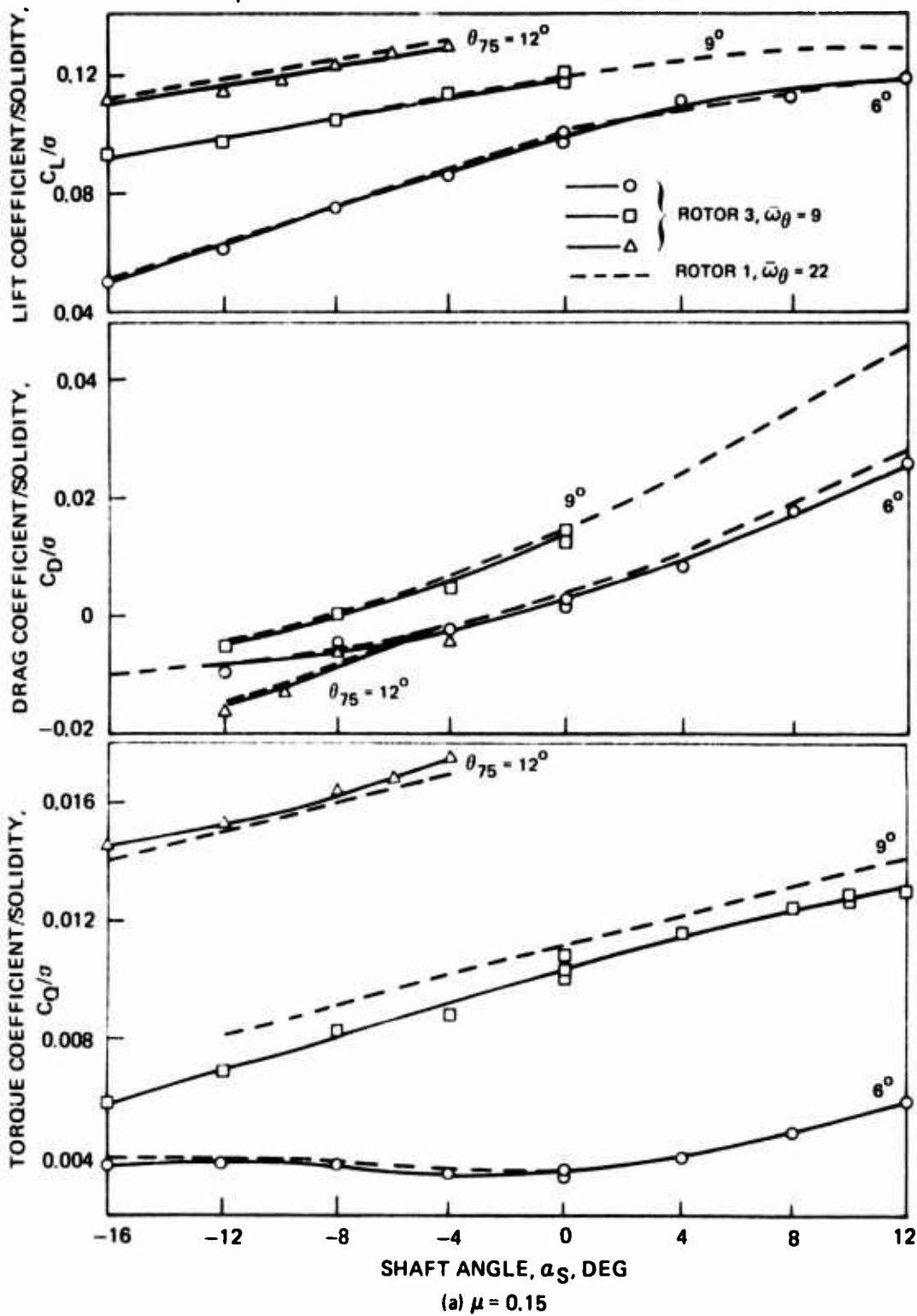
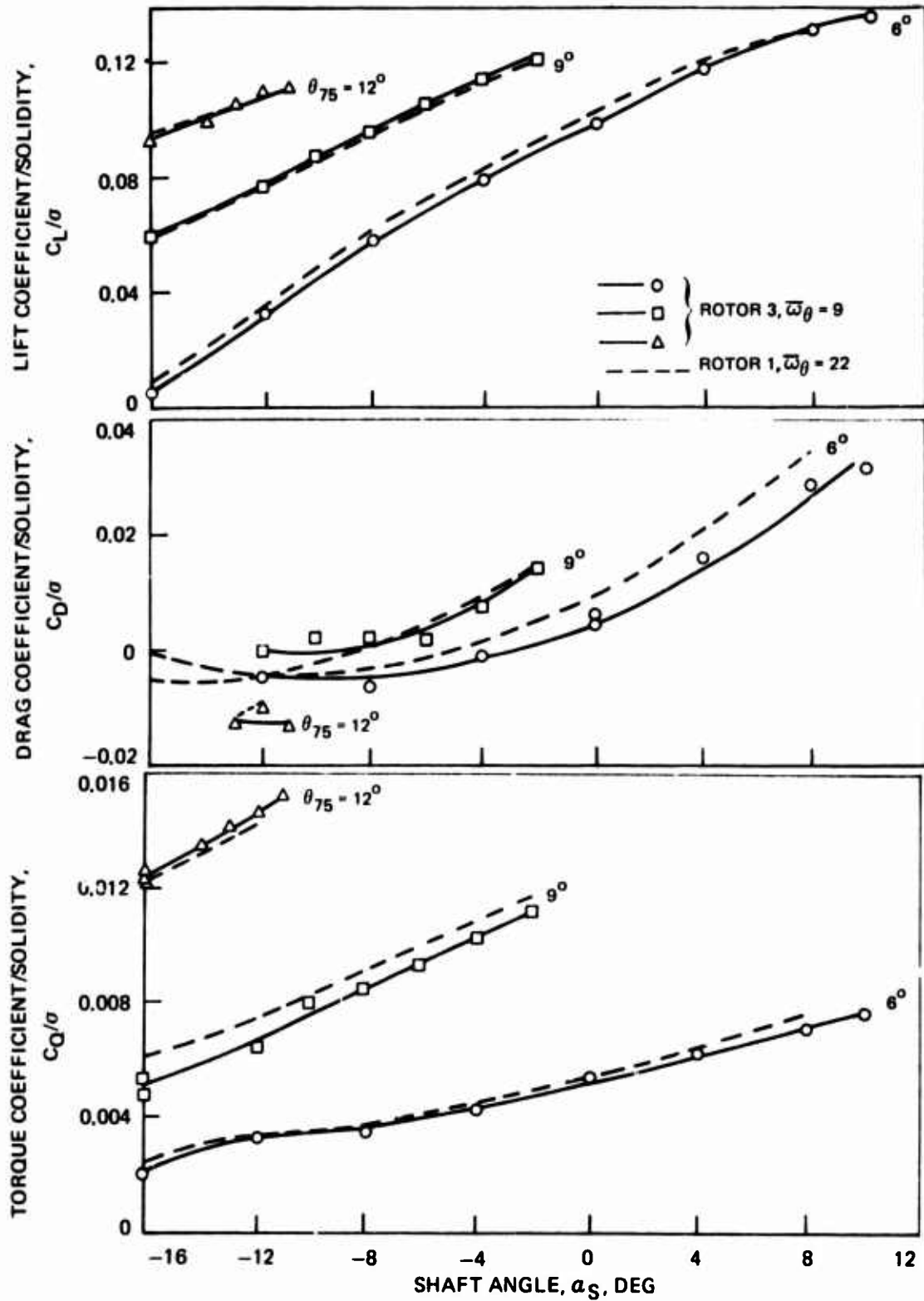


Figure 40. Effect of Torsional Frequency on Rotor Performance - $\bar{\omega}_\theta = 9$.

$\theta_1 = 0^\circ$ $b = 2$ $\sigma = 0.0332$ $AR = 19.2$ $MAC = 0.012$ $TR = 1:1$



(b) $\mu = 0.30$
Figure 40. Continued.

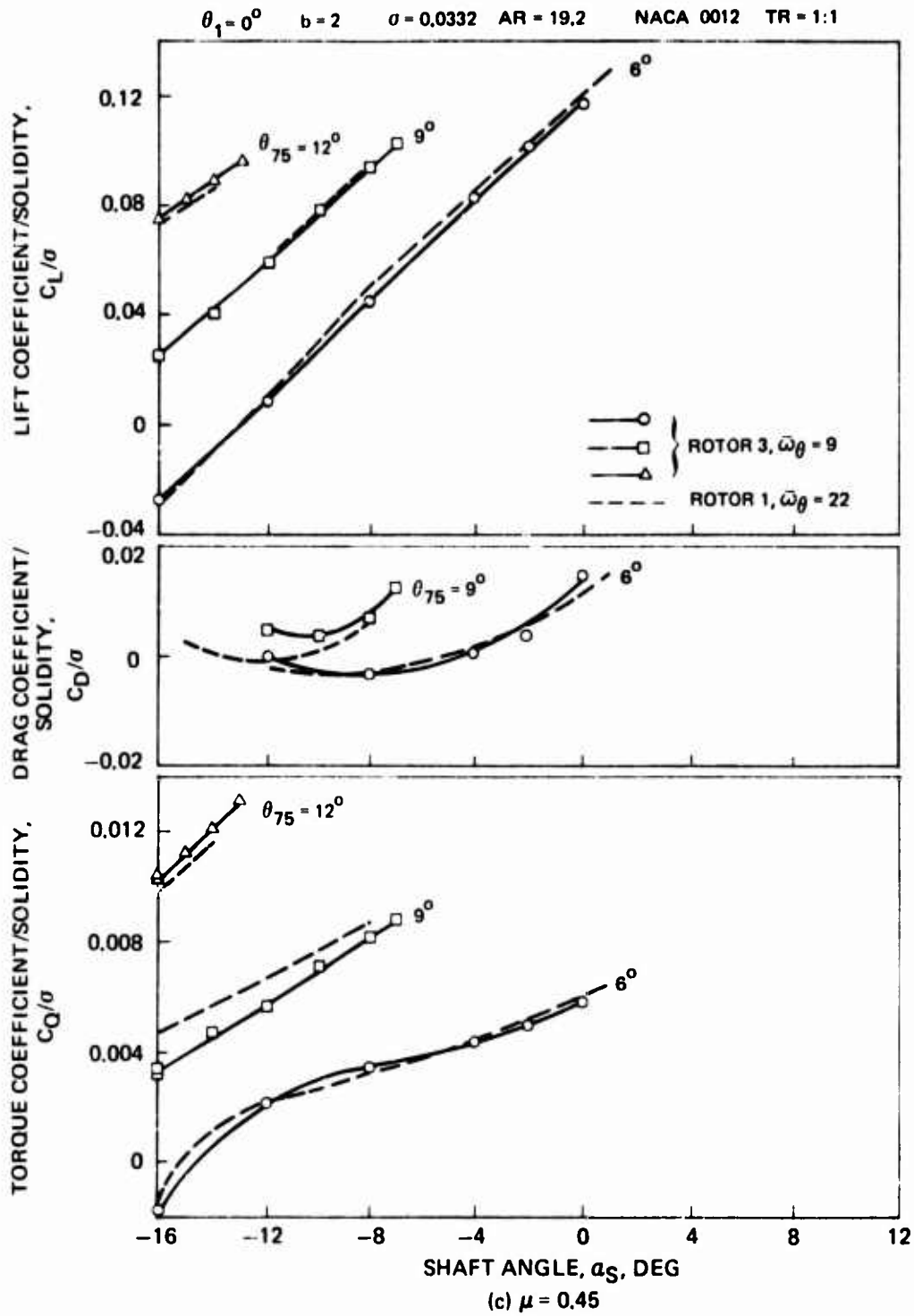


Figure 40. Concluded.

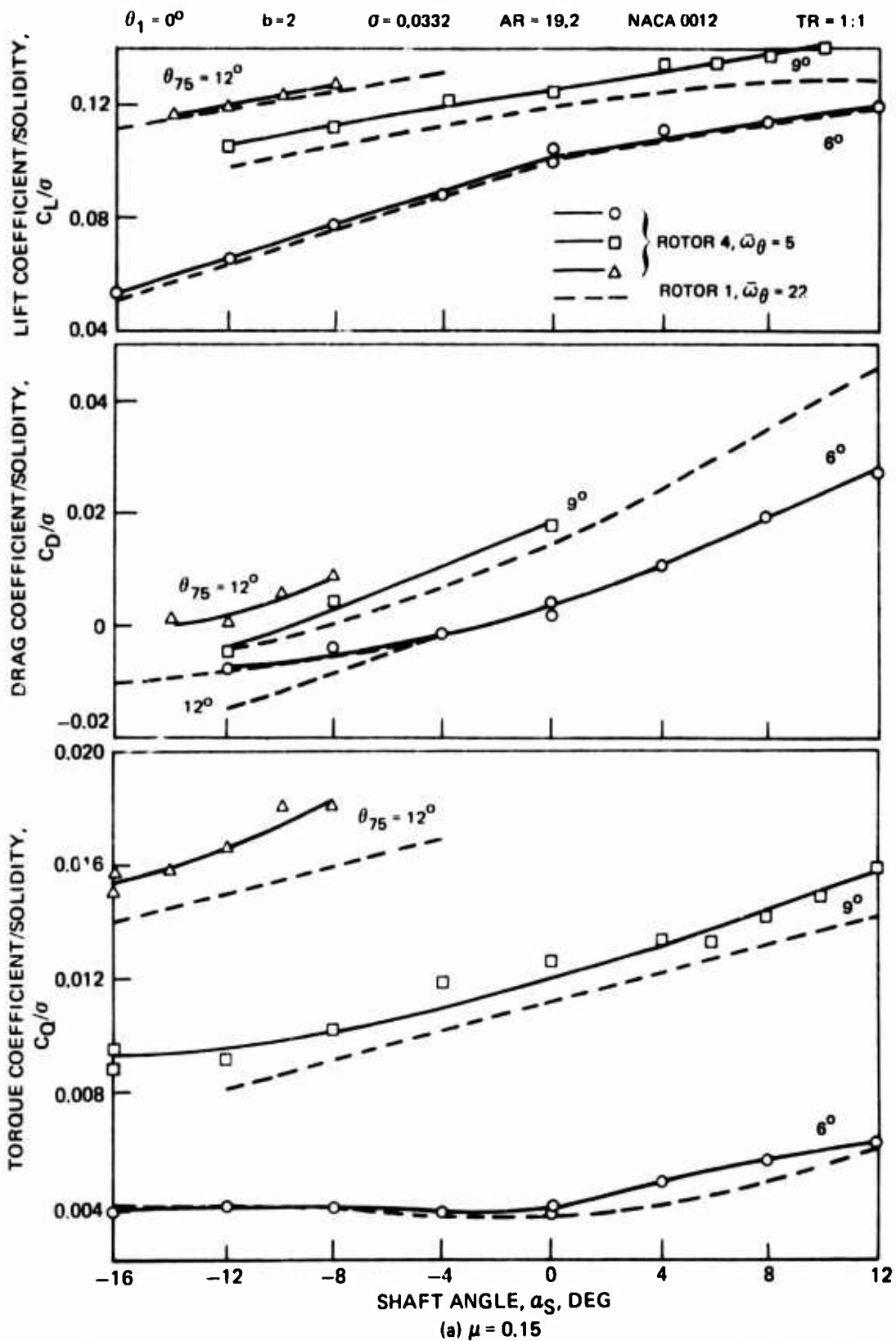


Figure 41. Effect of Torsional Frequency on Rotor Performance - $\bar{\omega}_\beta = 5$.

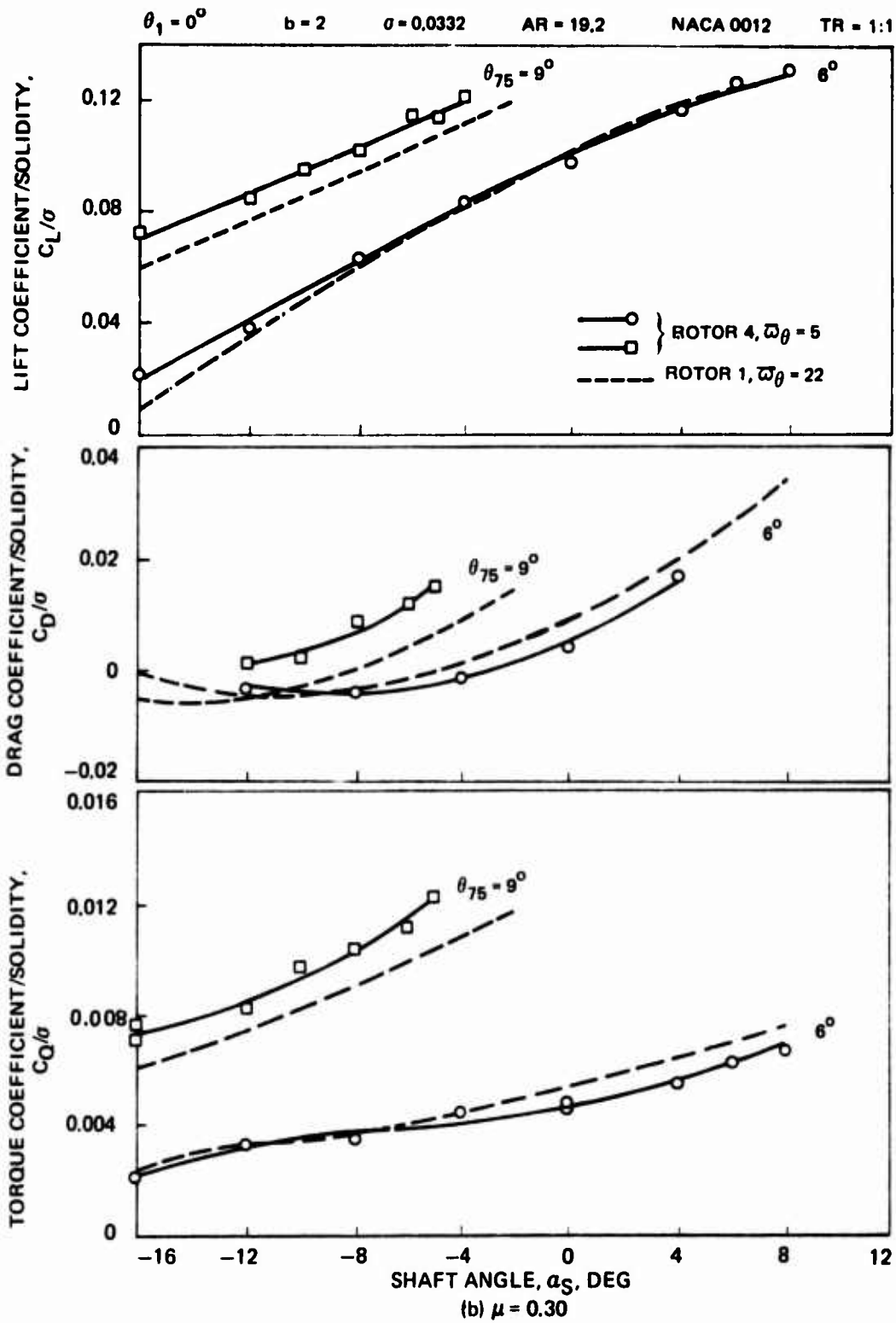


Figure 41. Continued.

$\theta_1 = 0^\circ$ $b = 2$ $\sigma = 0.0332$ $AR = 19.2$ $NACA 0012$ $TR = 1:1$

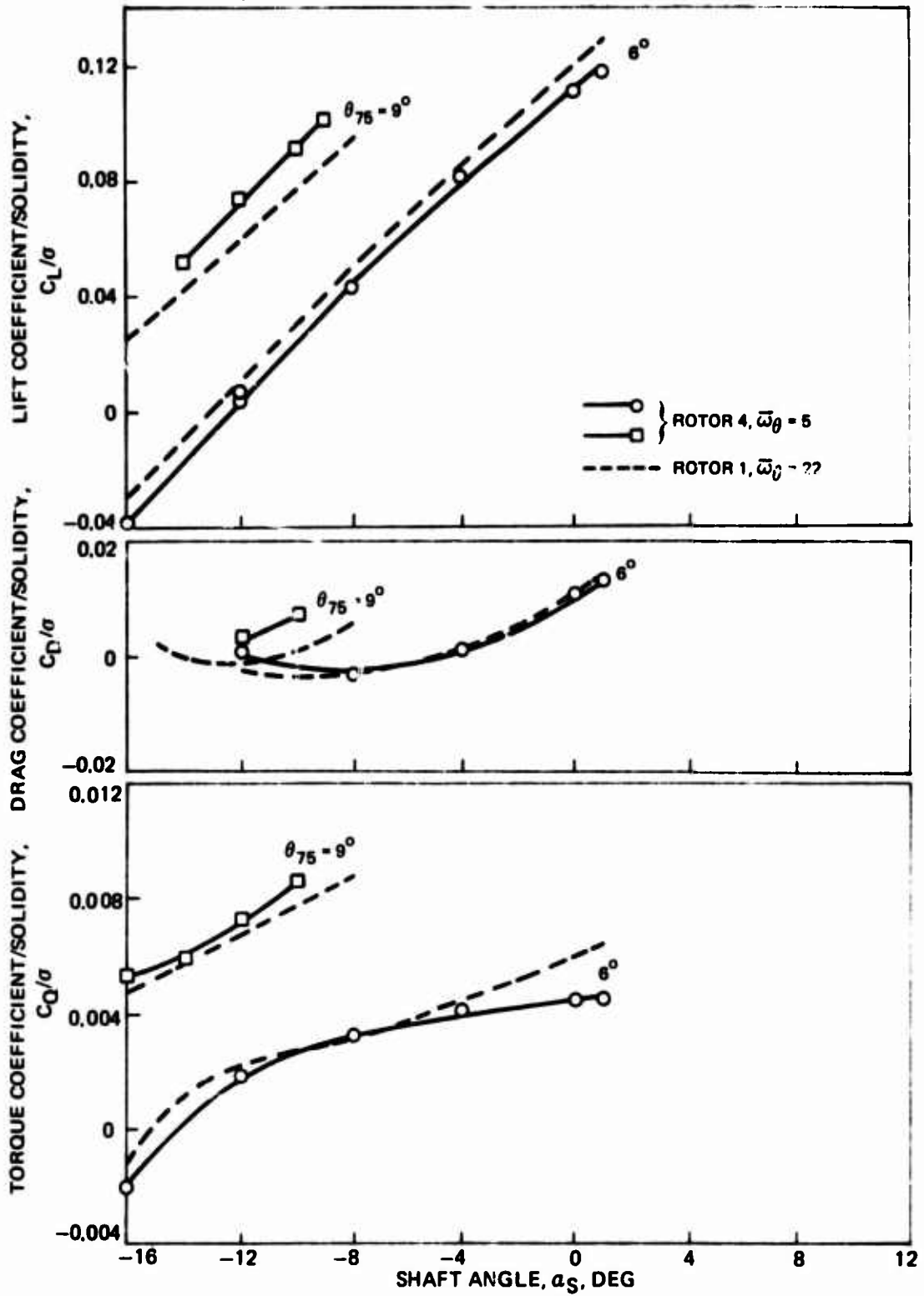


Figure 41. Concluded.

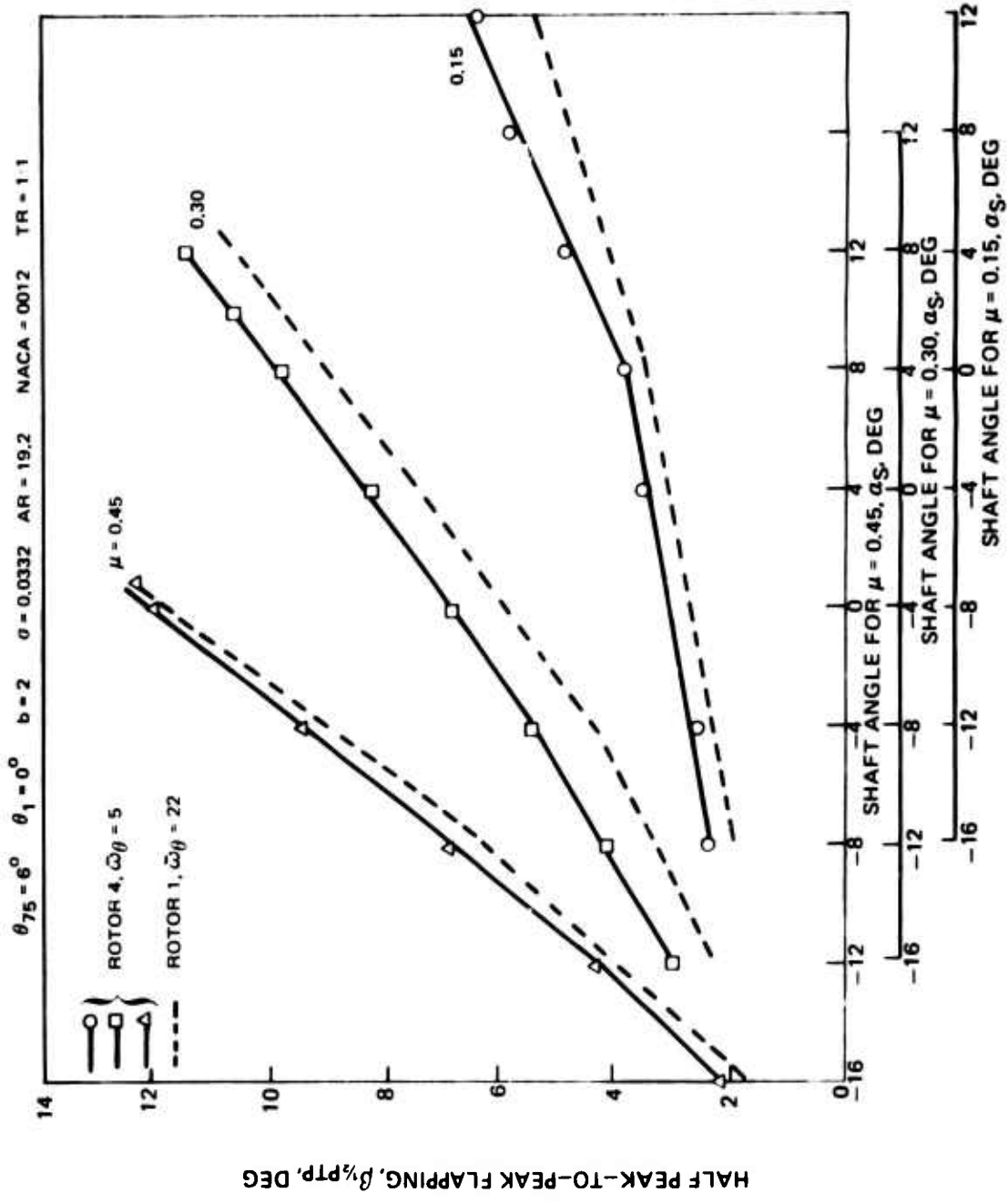


Figure 42. Effect of Torsional Frequency on Blade Flapping Response - $\bar{\omega}_\theta = 5$.

ROTOR 3 $\theta_{75} = 9^\circ$ $\theta_1 = 0^\circ$ $b = 2$ $\sigma = 0.0372$ $AR = 19.2$ $NACA\ 0012$ $TR = 1:1$

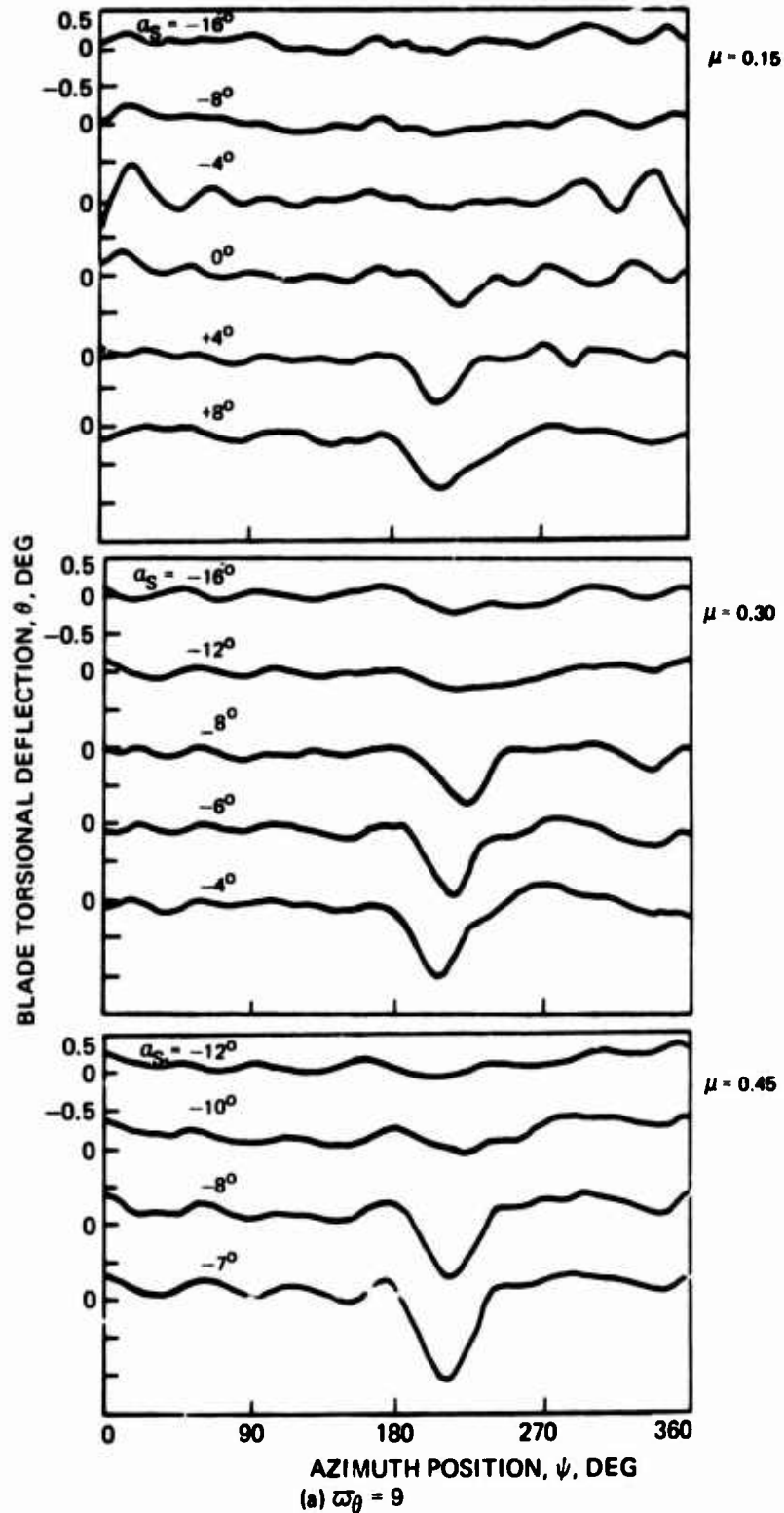
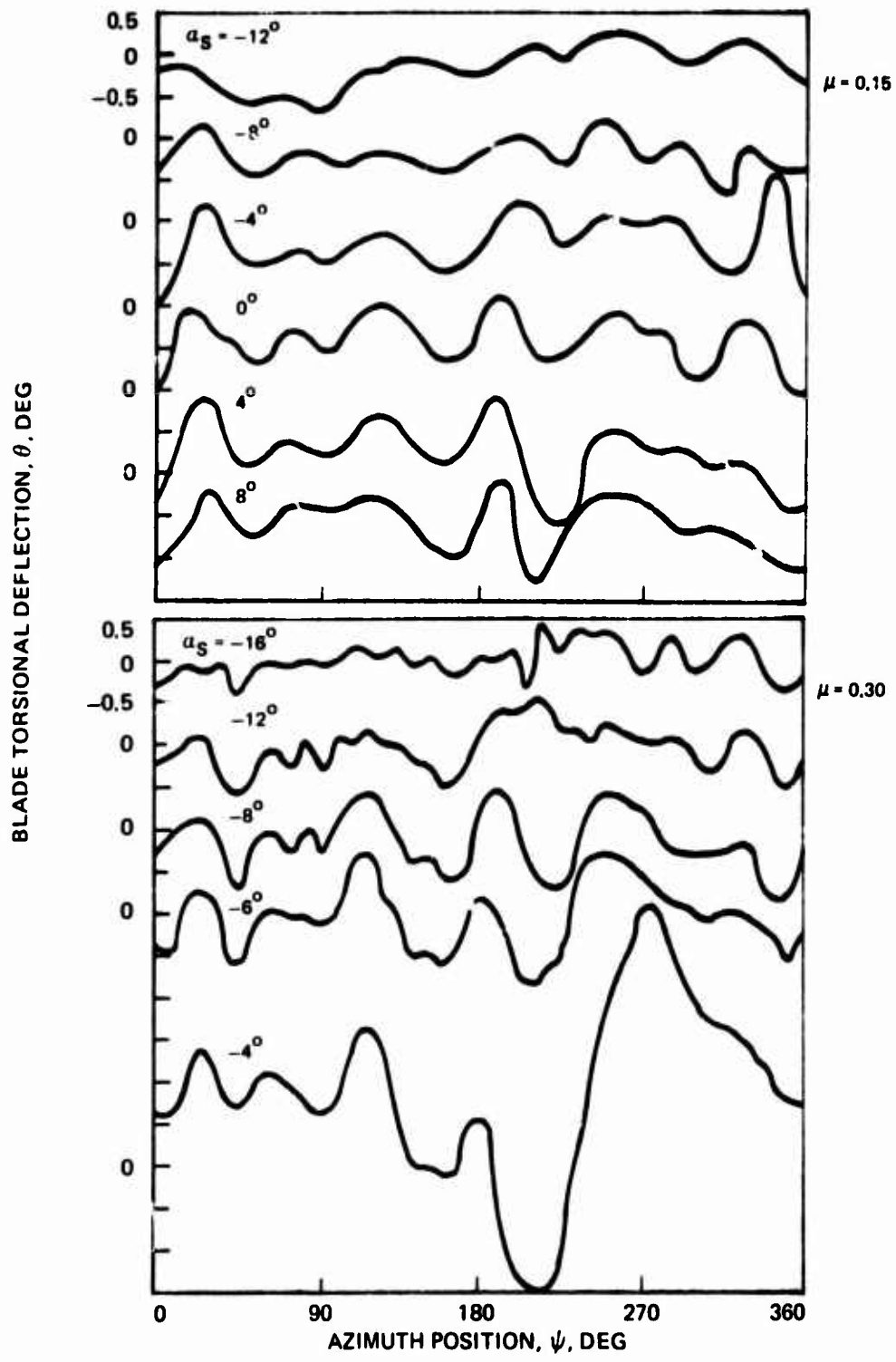


Figure 43. Effect on Torsional Deflection of Increasing Rotor Lift by Increasing Shaft Angle.



(b) $\bar{\omega}_\theta = 5$

Figure 43. Concluded.

$\theta_1 = 0^\circ$ $b = 2$ $c = 0.0332$ $AR = 19.2$ $NACA\ 0012$ $TR = 1:1$

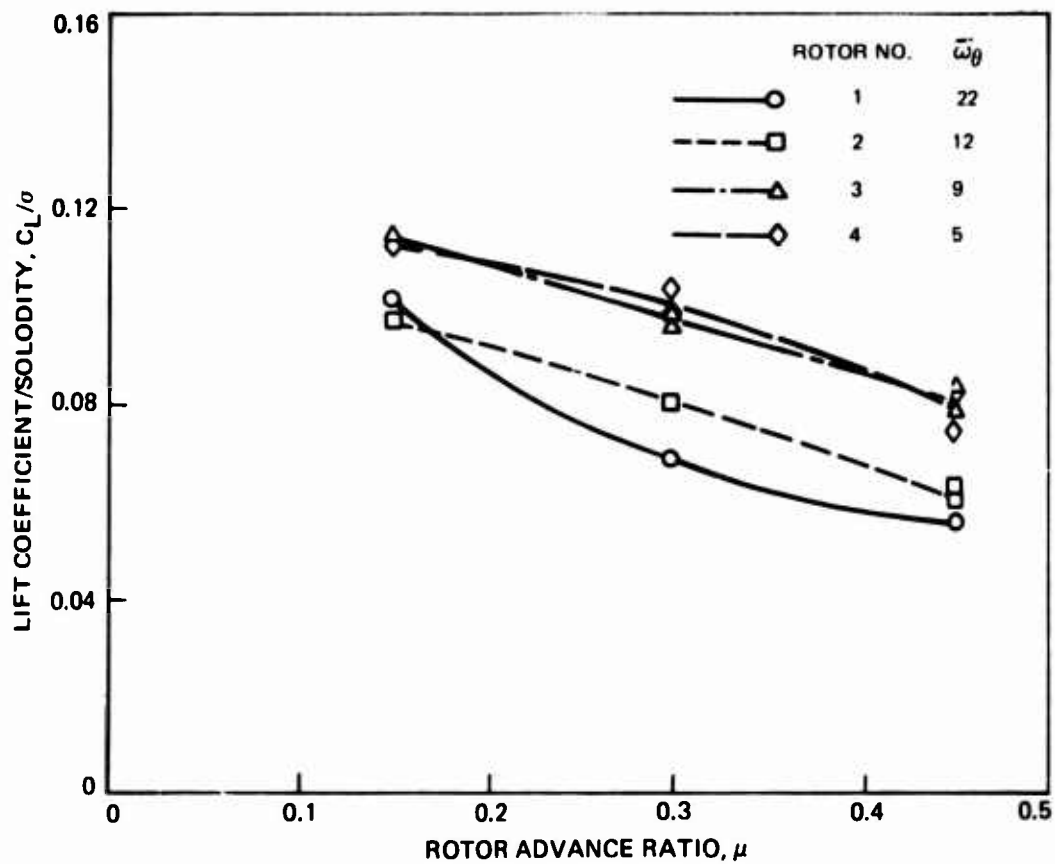


Figure 44 . Effect of Torsional Frequency on Oscillatory Torsional Deflection Onset.

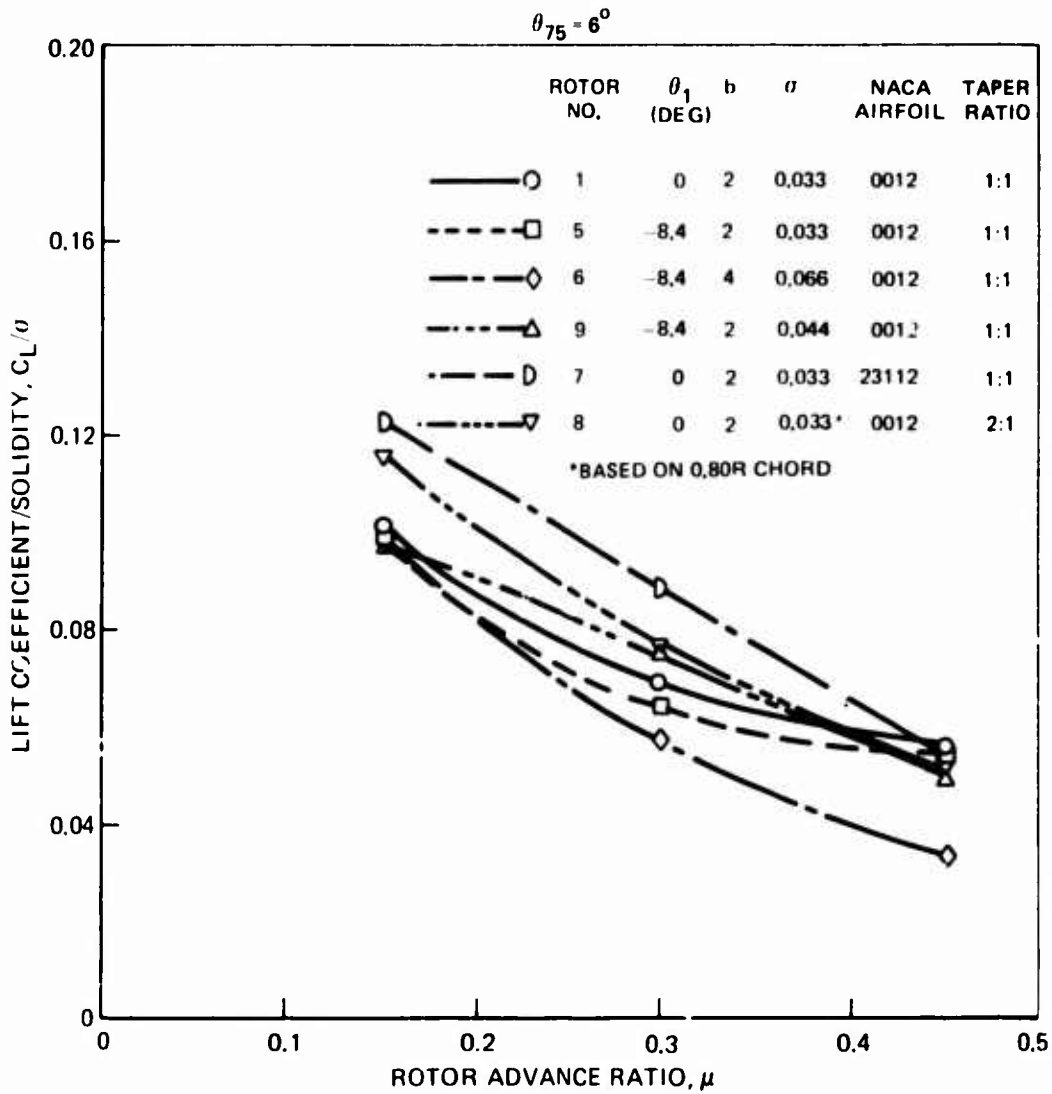


Figure 45. Comparison of the Average Rotor Lift Coefficient to Solidity Ratio at Stall Threshold Indicated by Hot-Film, C_L/σ , Flapping and Edgewise Stress Data.

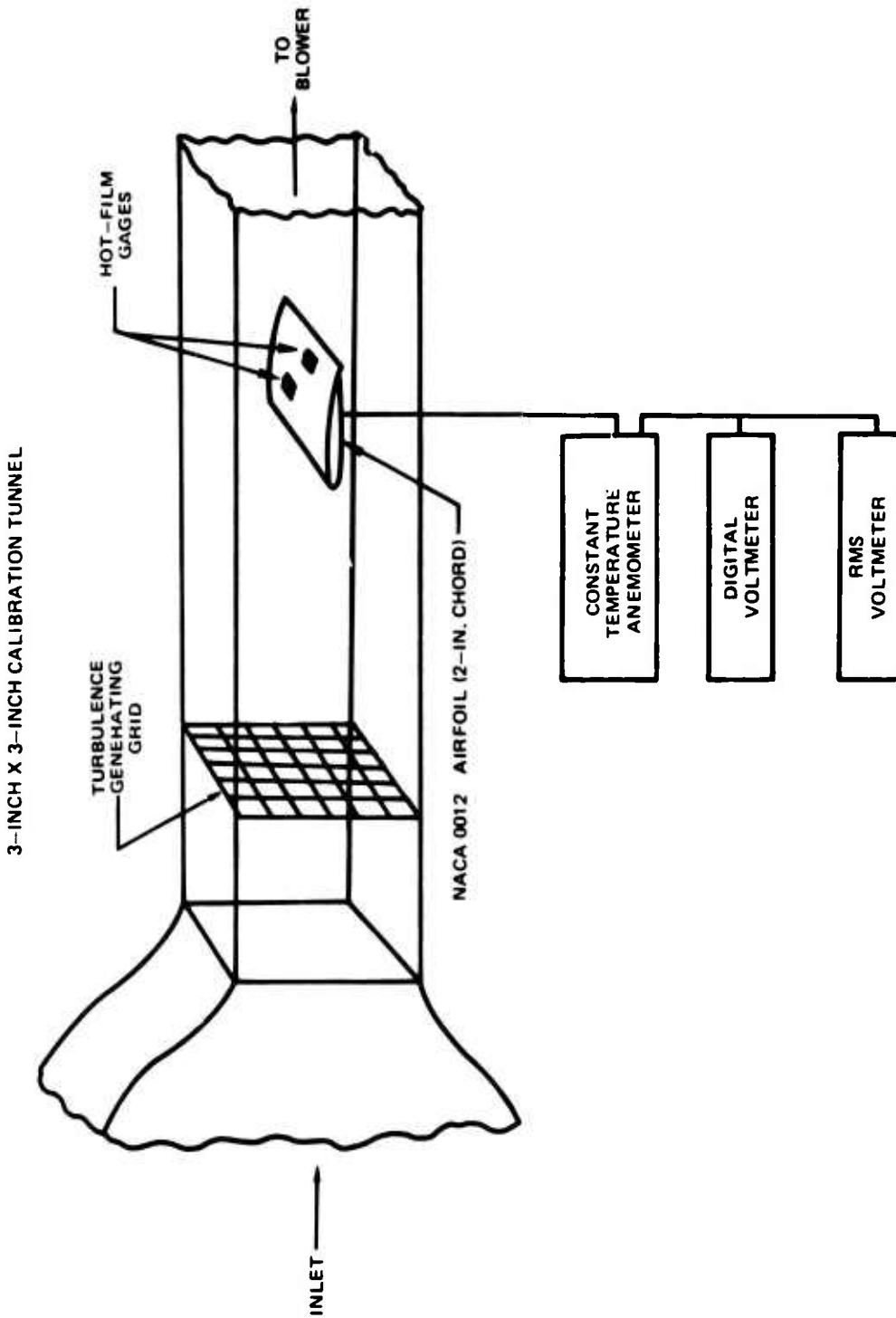


Figure 46. Experimental Apparatus for Correlation Tests Between Oil-Film Flow Visualization and Hot-Film Measurements.

1/4-INCH GRID - 2.5% TURBULENCE

NACA 0012 AIRFOIL (2-IN. CHORD)

ANGLE OF
ATTACK = -5°

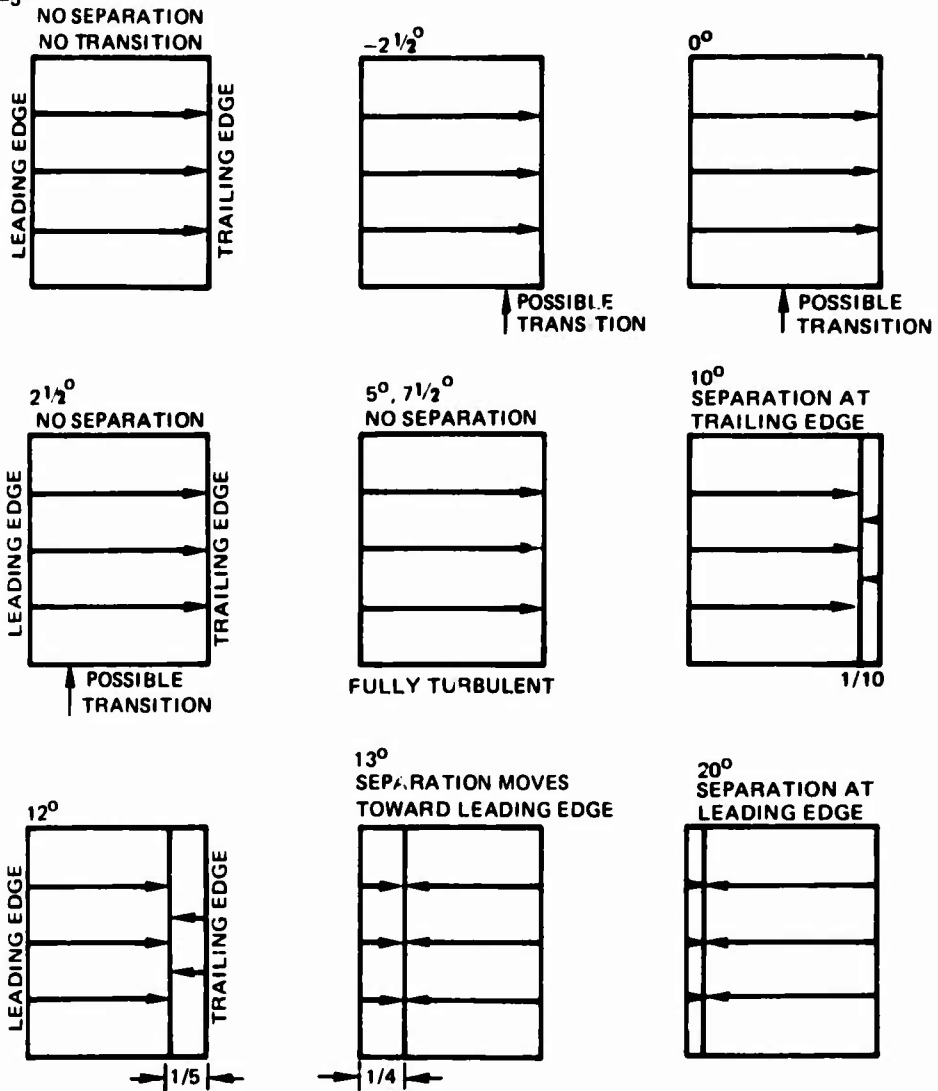


Figure 47. Flow Patterns on Nonrotating NACA 0012 Airfoil Determined by Oil-Film Flow Visualization.

1/4-INCH GRID - 2.5% TURBULENCE

○ MID CHORD

● TRAILING EDGE

■ SEPARATION REGION

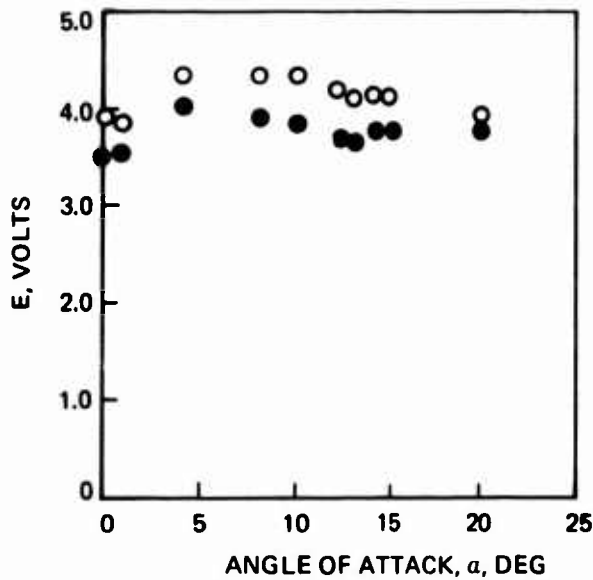
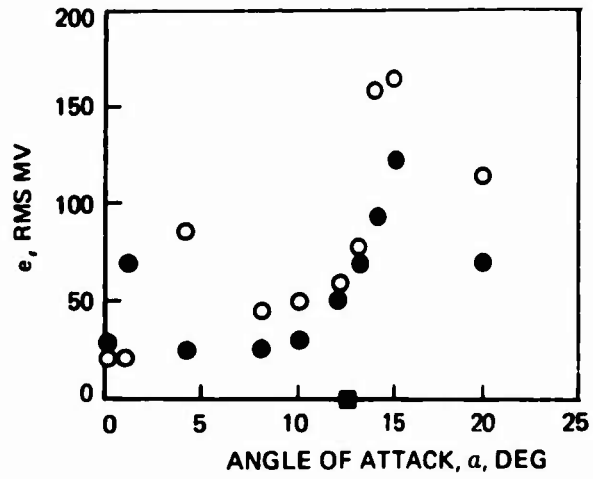


Figure 48. Output Voltages From Hot Films Mounted on Nonrotating NACA 0012 Airfoil.

ROTOR 5 $\mu = 0.30$ $\theta_{75} = 6^\circ$ $\theta_1 = -8.4^\circ$ $b = 2$ $\bar{\omega}_\theta = 23$ $\sigma = 0.0332$ $AR = 19.2$ $NACA\ 0012$ $TR = 1:1$

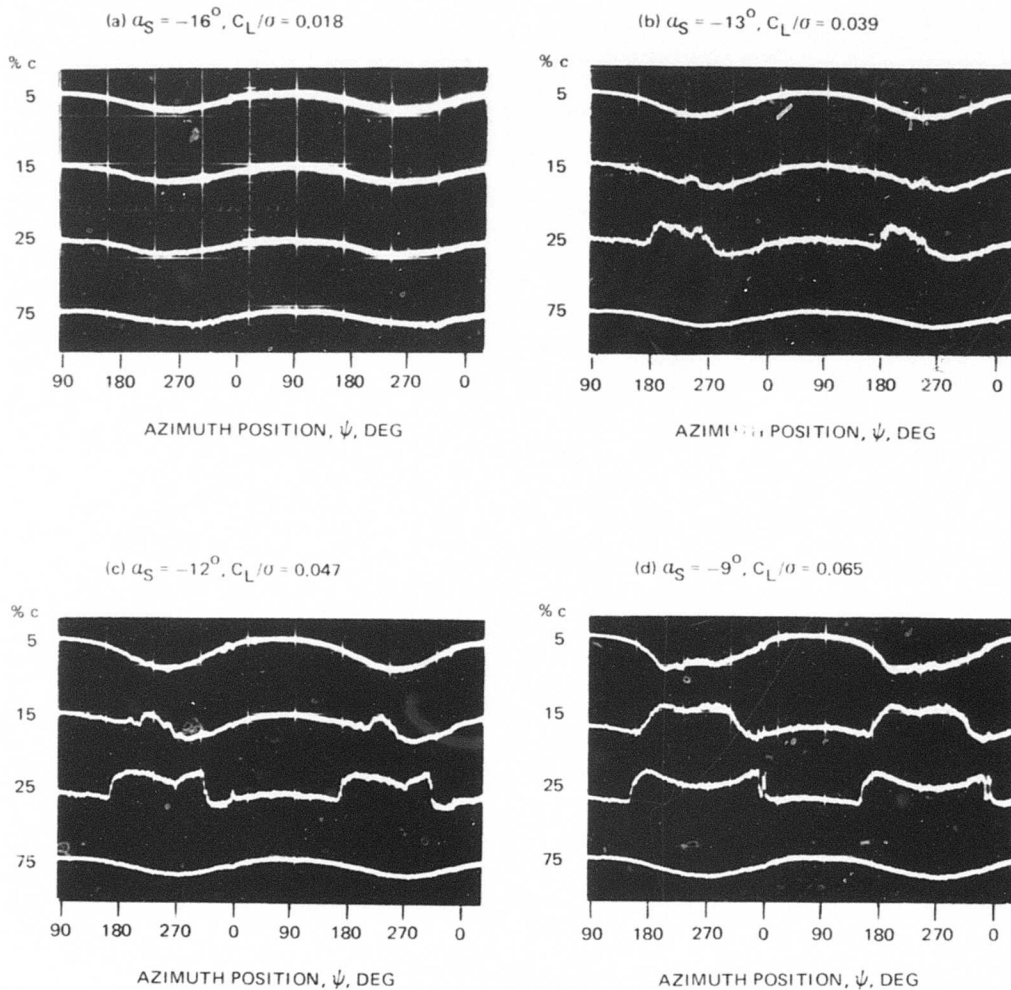
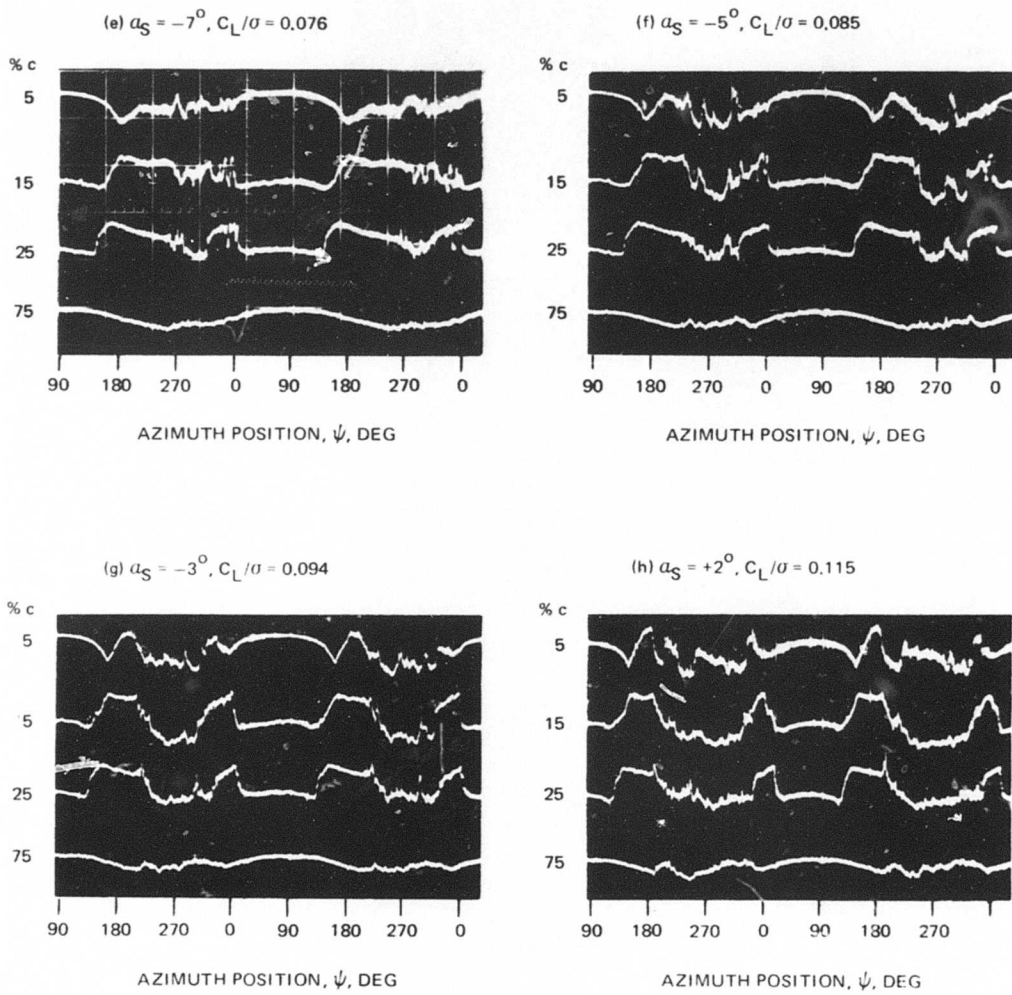


Figure 49. Oscilloscope Outputs of Hot-Film Signals at 85% Span.

ROTOR 5 $\mu = 0.30$ $\theta_{75} = 6^\circ$ $\theta_1 = -8.4^\circ$ $b = 2$ $\bar{\omega}_\theta = 23$ $\sigma = 0.0332$ $AR = 19.2$ $NACA\ 0012$ $TR = 1:1$



OSCILLOSCOPE SENSITIVITY: 0.5 V/cm @ 5% c, 15% c, AND 25% c, 1.0 V/cm @ 75% c

Figure 49. Concluded.

ROTOR 5 $\mu = 0.30$ $\theta_{75} = 6^\circ$ $\theta_1 = -8.4^\circ$ $b = 2$ $\bar{\omega}\beta = 23$ $\sigma = 0.0332$ $AR = 19.2$ $NACA$ 0012 $TR = 1:1$

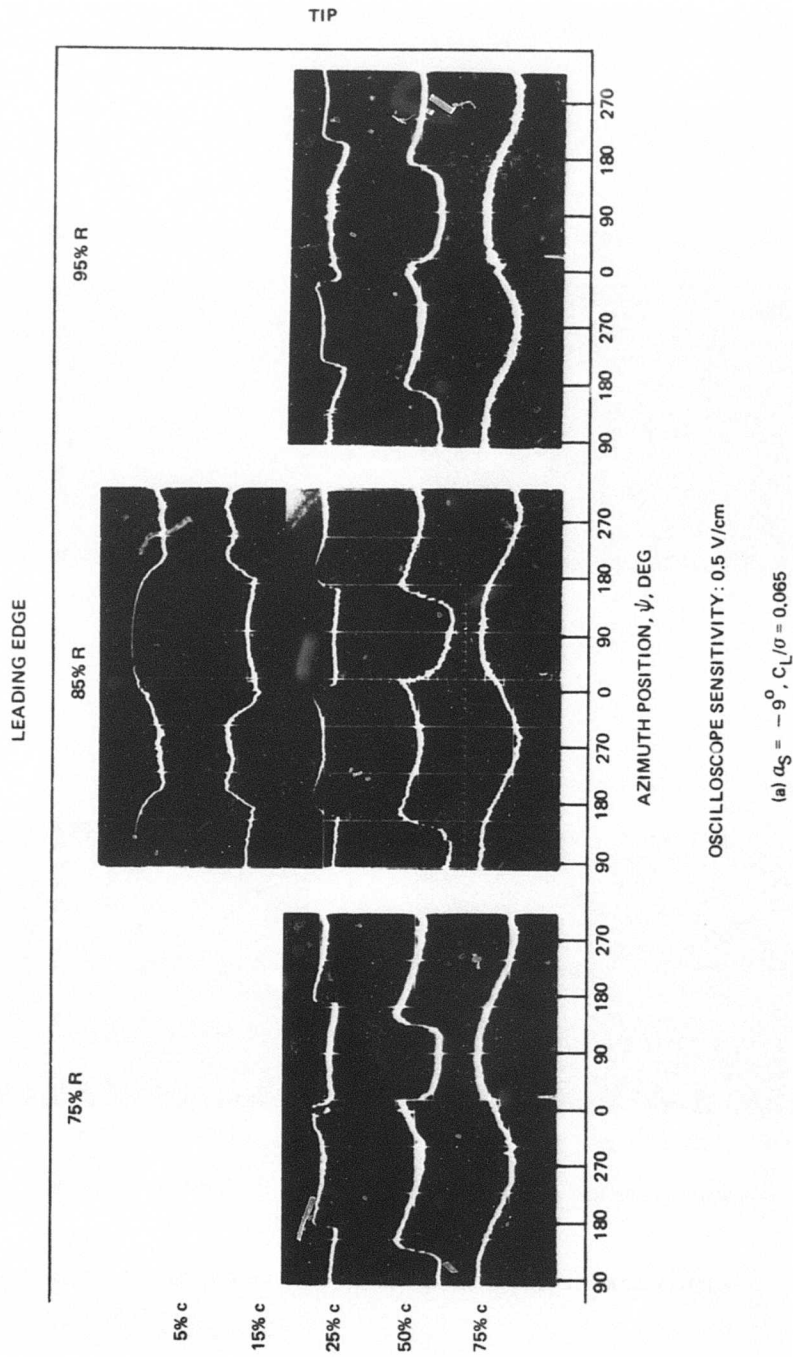
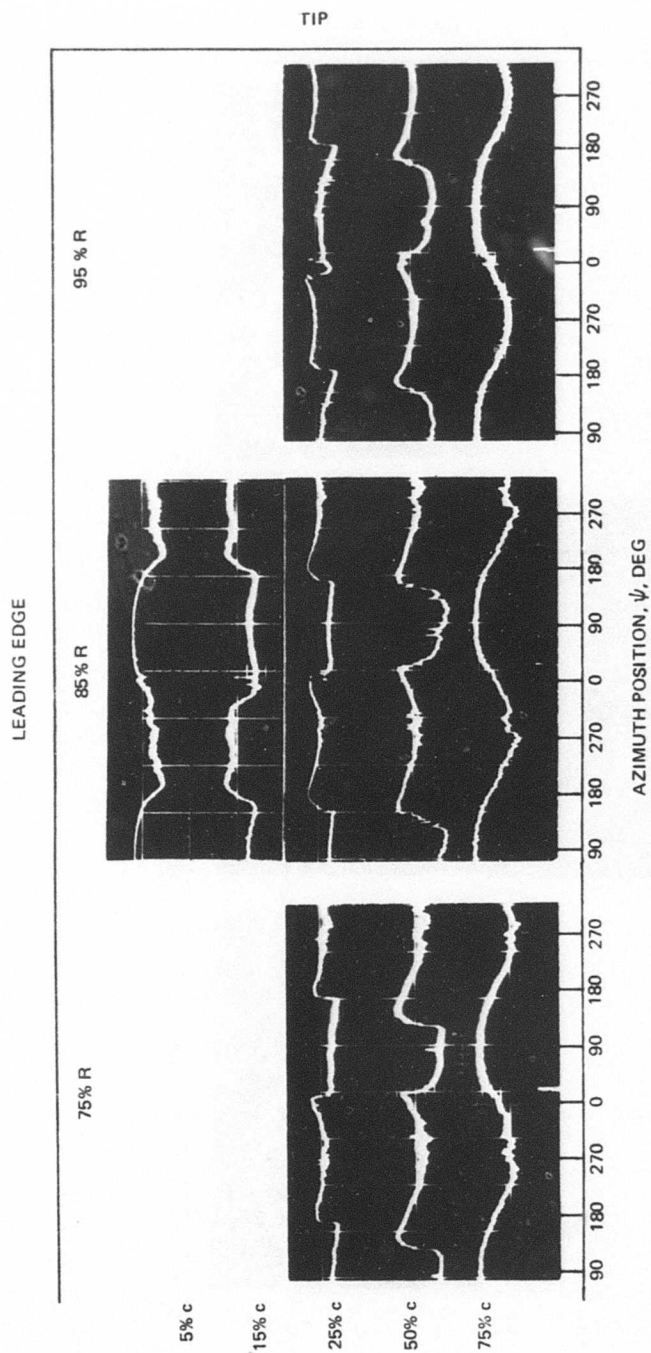


Figure 50. Oscilloscope Outputs of Hot-Film Signals for Rotor Number 5.

ROTOR 5 $\mu = 0.30$ $\theta_{75} = 6^\circ$ $\theta_1 = -8.4^\circ$ $b = 2$ $\bar{\omega}\bar{\theta} = 23$ $\sigma = 0.0332$ $AR = 19.2$ $NACA$ 0012 $TR = 1:1$



OSCILLOSCOPE SENSITIVITY: 0.5 V/cm

(b) $\alpha_S = -8^\circ$, $C_L/\sigma = 0.070$

Figure 50. Continued.

ROTOR 5 $\mu = 0.30$ $\theta_{75} = 6^\circ$ $\theta_1 = -8.4^\circ$ $b = 2$ $\bar{\omega}_0 = 23$ $\nu = 0.0332$ $AR = 19.2$ $NACA$ 0012 $TR = 1:1$

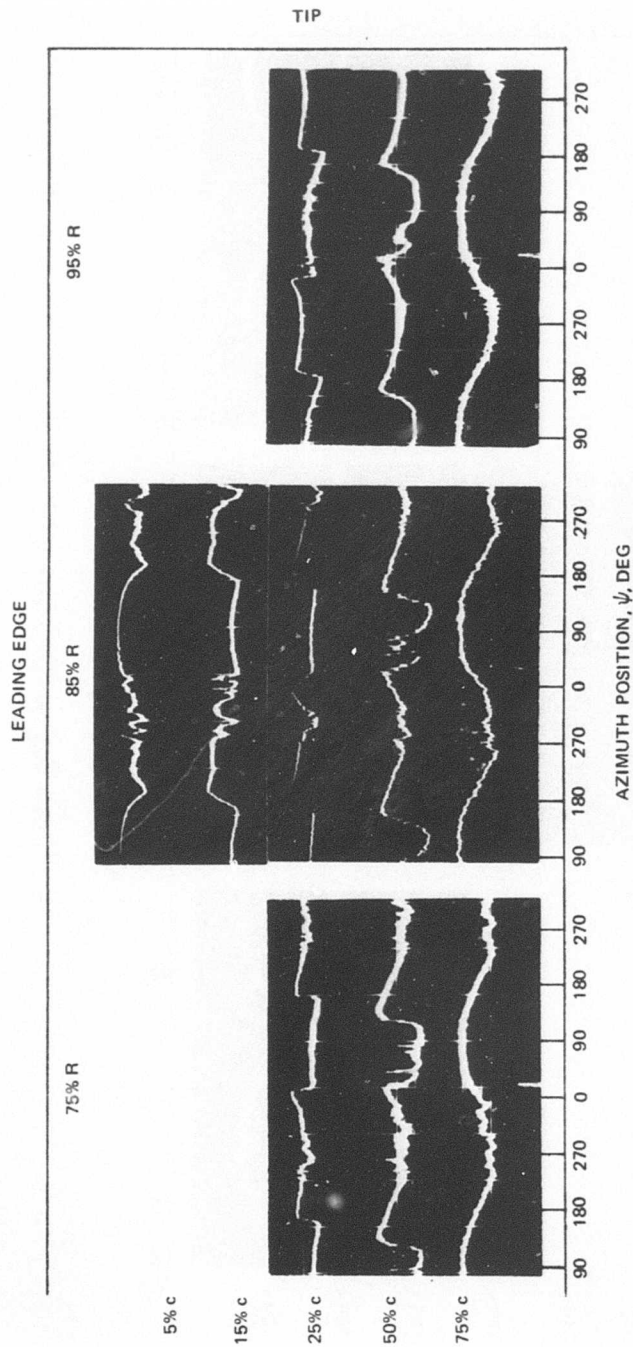


Figure 50. Continued.

ROTOR 5 $\mu = 0.30$ $\theta_{75} = 6^\circ$ $\theta_1 = -8.4^\circ$ $b = 2$ $\bar{\omega}g = 23$ $\sigma = 0.0332$ $AR = 19.2$ $NACA$ 0012 $TR = 1:1$

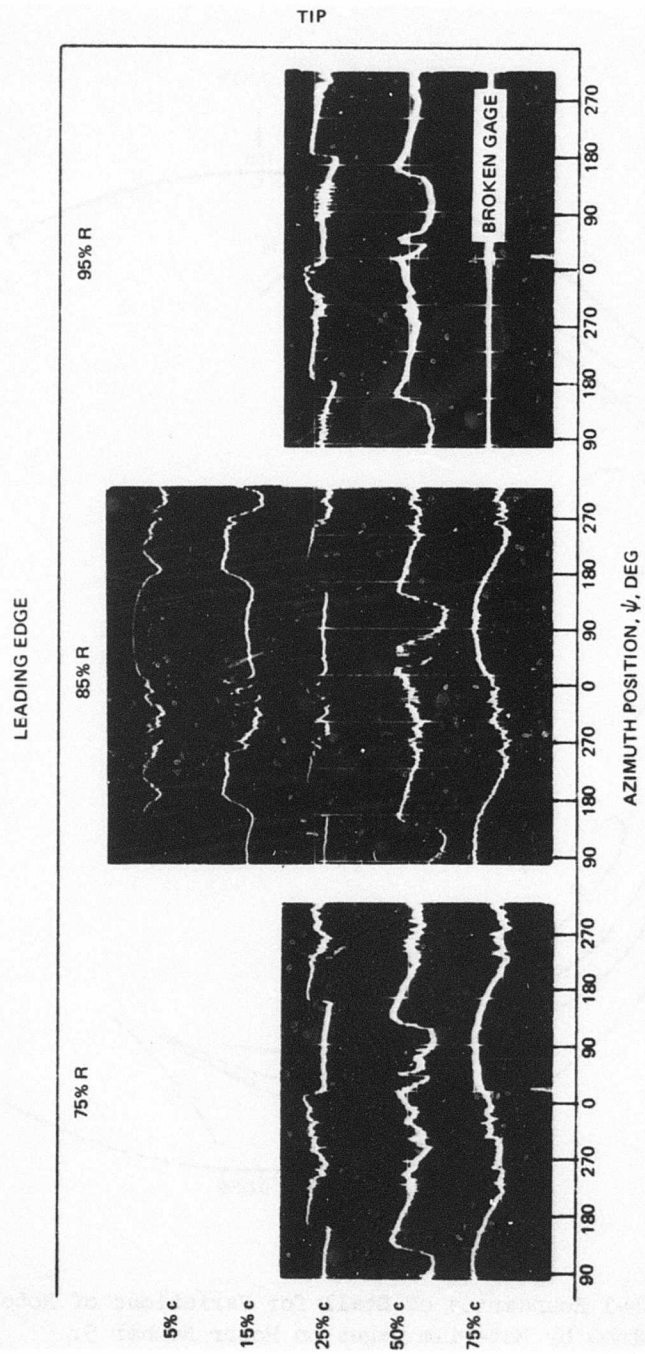


Figure 50. Concluded.

ROTOR 5 $\mu = 0.30$ $\theta_{75} = 6^\circ$ $\theta_1 = -8.4^\circ$ $b = 2$ $\bar{\omega}\theta = 23$ $\sigma = 0.0332$ $AR = 19.2$ $NACA 0012$ $TR = 1:1$

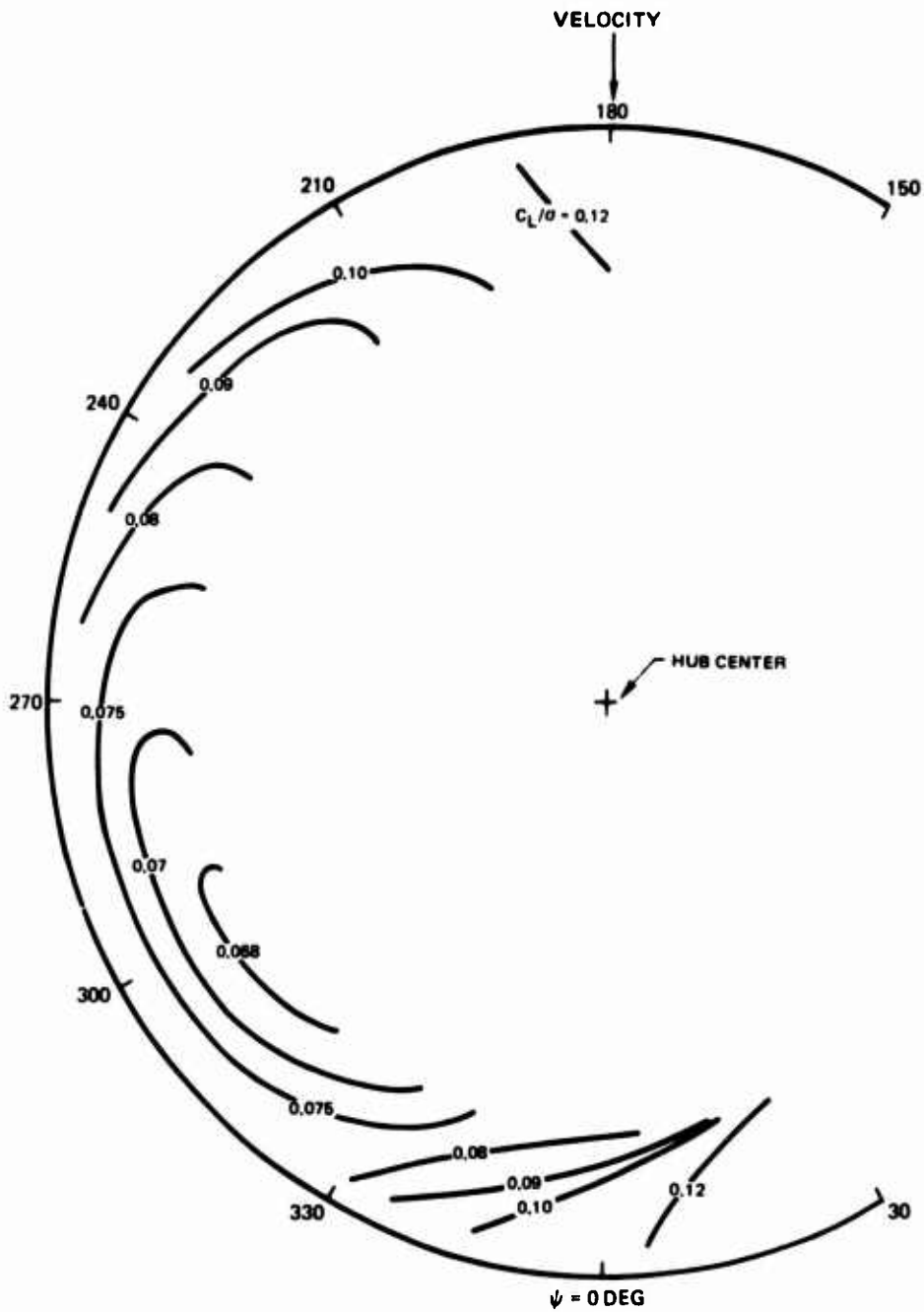


Figure 51. Azimuthal Boundaries of Stall for Variations of Rotor Lift as Determined by Hot-Film Gages on Rotor Number 5.

ROTOR 5 $\mu = 0.3$ $\theta_{75} = 6^\circ$ $\theta_1 = -8.4^\circ$ $b = 2$ $\bar{\omega} = 23$ $\sigma = 0.332$ $AR = 19.2$ $NACA 0012$ $TR = 1:1$

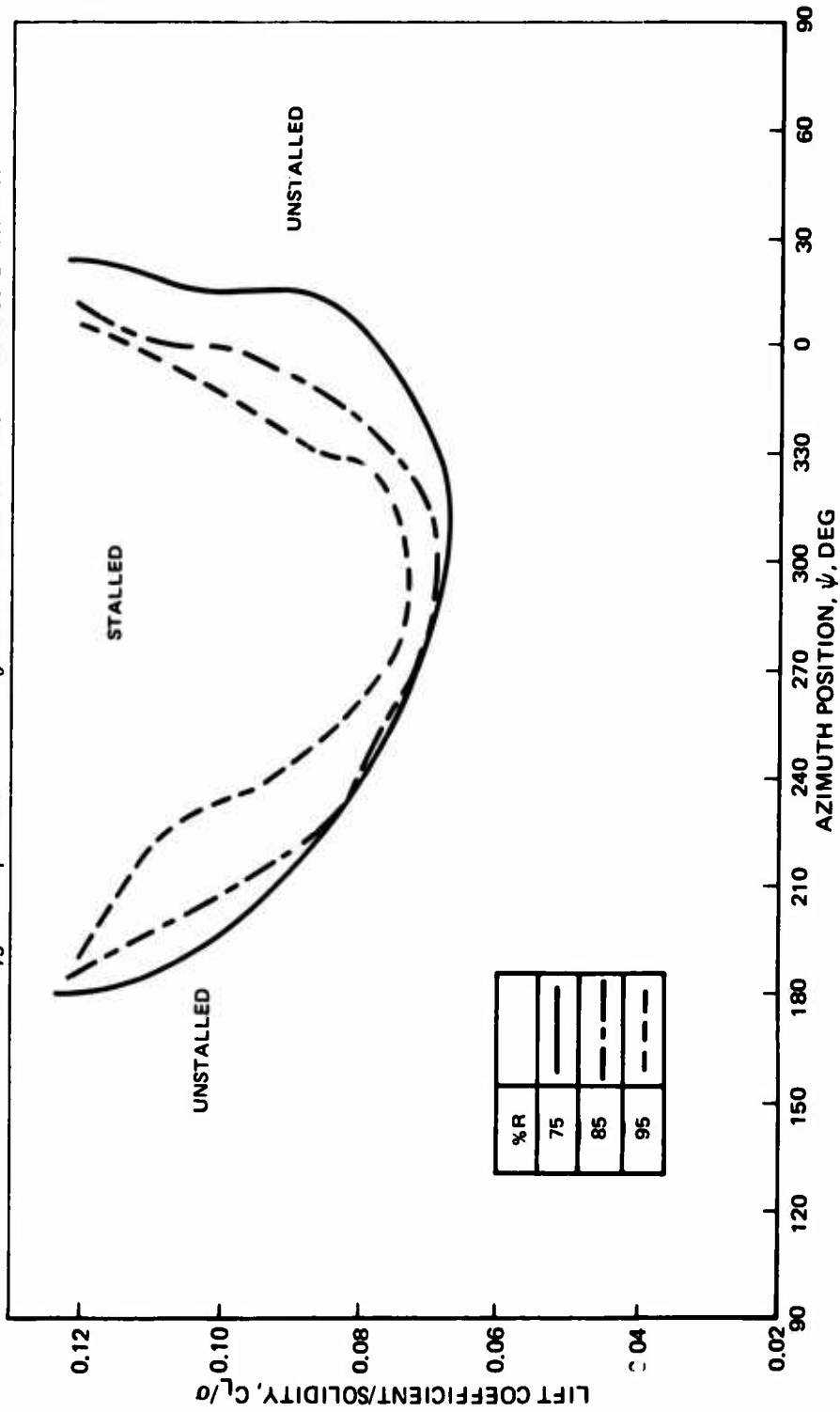


Figure 52. Spanwise Variations in Stall Boundaries at 75% Chord for Rotor Number 5.

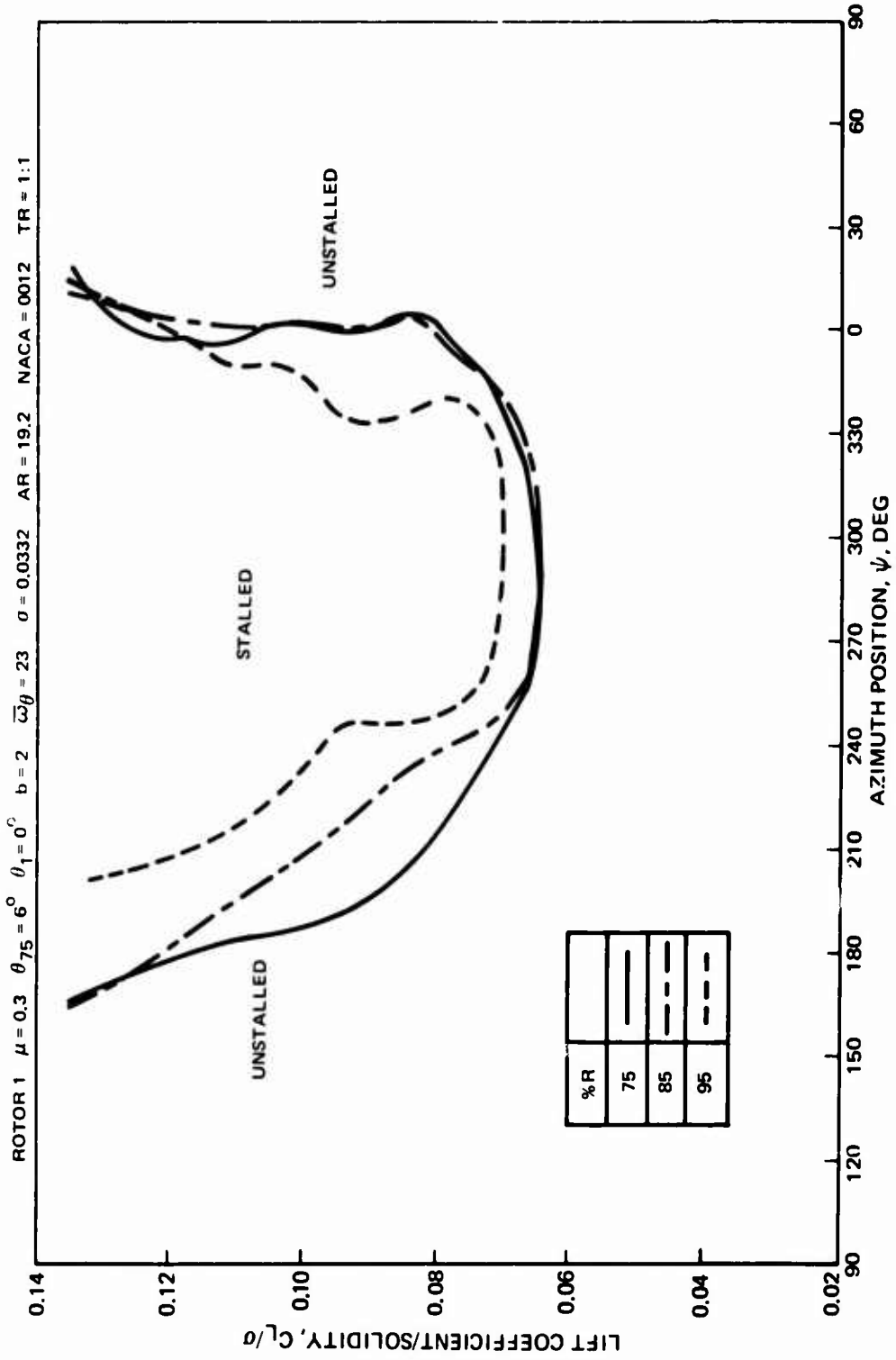


Figure 53. Spanwise Variations in Stall Boundaries at 75% Chord for Rotor Number 1.

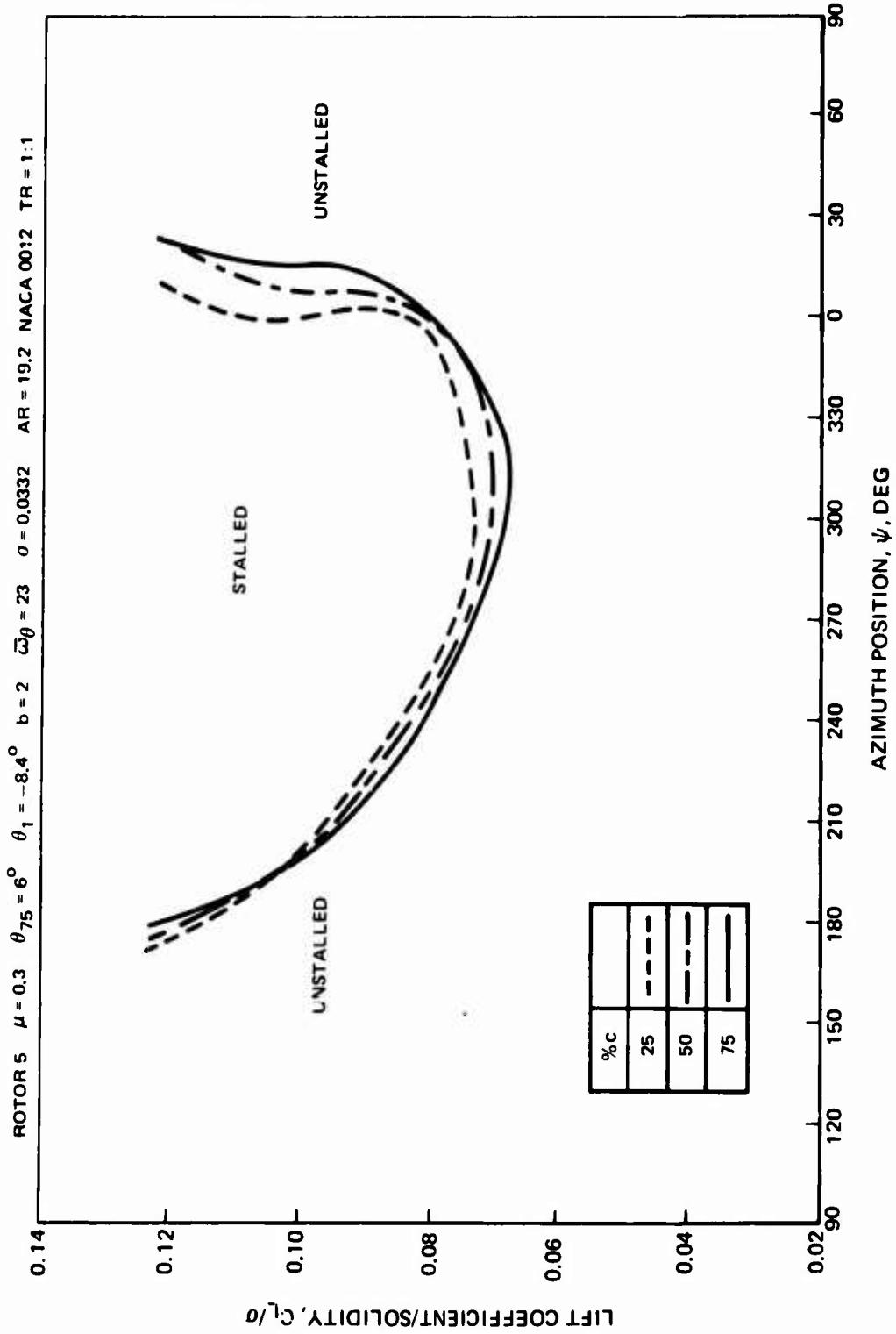


Figure 54. Chordwise Variations in Azimuthal Extent of Separated Boundary Layer at 75% Span.

ROTOR 1 $\mu = 0.30$ $\beta_1 = 0$ $b = 2$ $\omega\beta = 23$ $\sigma = 0.0332$ $AR = 19.2$ $NACA 0012$ $TR = 1:1$

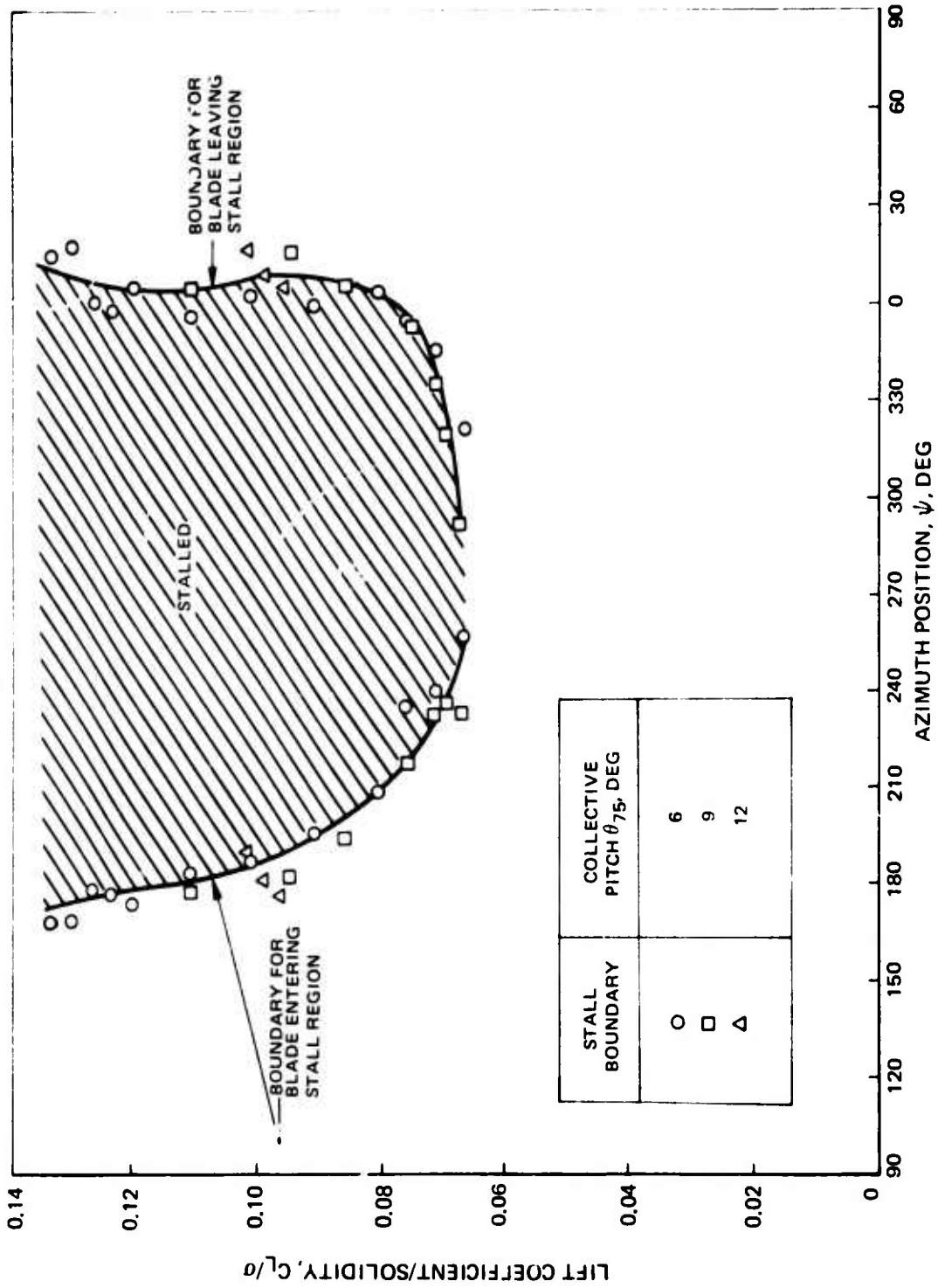


Figure 55. Effect of Collective Pitch on Stall Boundaries as Determined From Hot-Film Gage Data for Rotor Number 1.

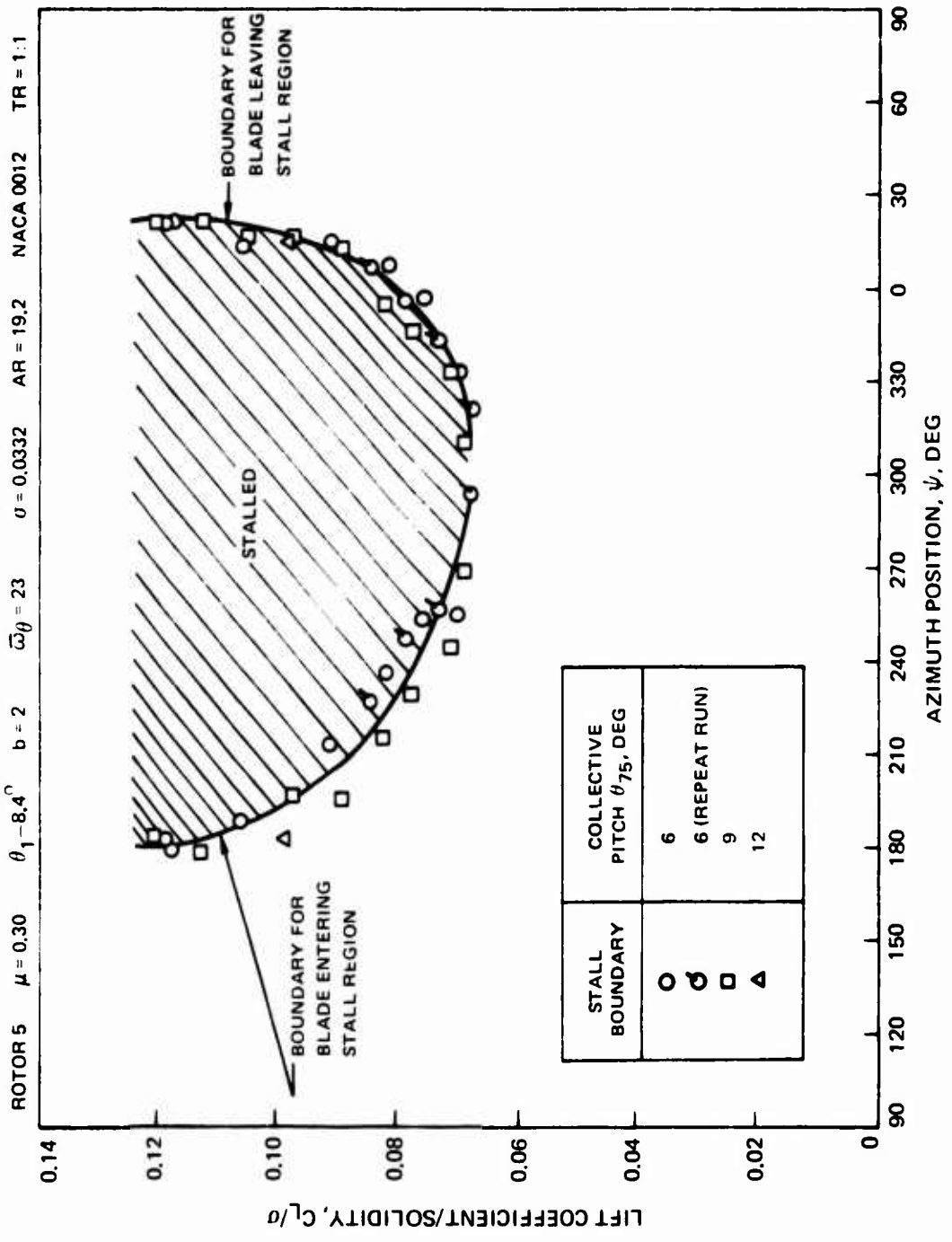


Figure 56. Effect of Collective Pitch on Stall Boundaries as Determined From Hot-Film Gage Data for Rotor Number 5.

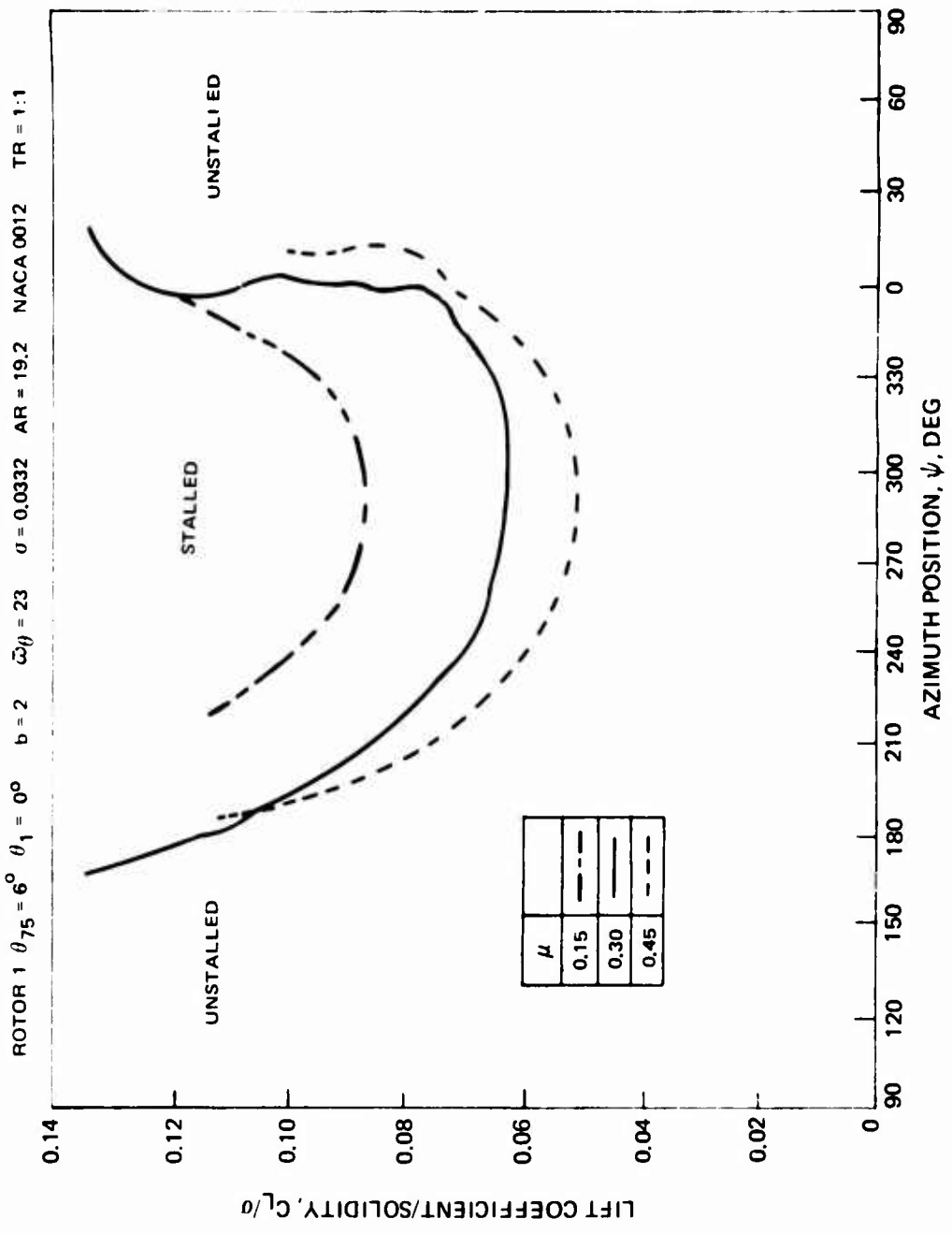


Figure 57. Effect of Advance Ratio on Stall Boundaries at 75% R, 75% c for Rotor Number 1.

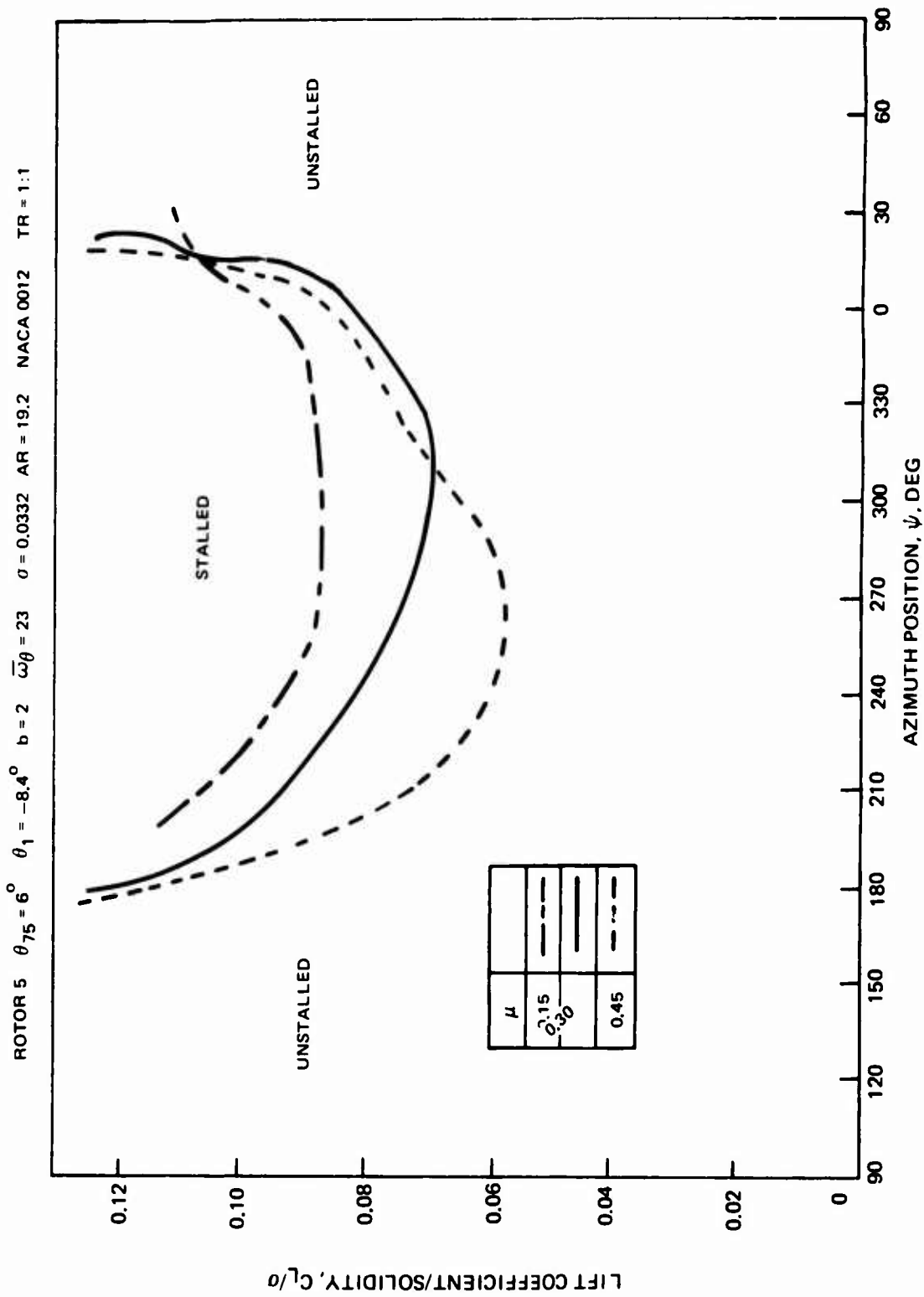


Figure 58. Effect of Advance Ratio on Azimuthal Extent of Stall at 75% R, 75% c for Rotor Number 5.

ROTOR 5 $\mu = 0.30$ $\theta_{75} = 6^\circ$ $\theta_1 = -8.4^\circ$ $b = 2$ $\bar{\omega}_\theta = 23$ $\sigma = 0.0332$ $AR = 19.2$ $NACA\ 0012$ $TR = 1:1$

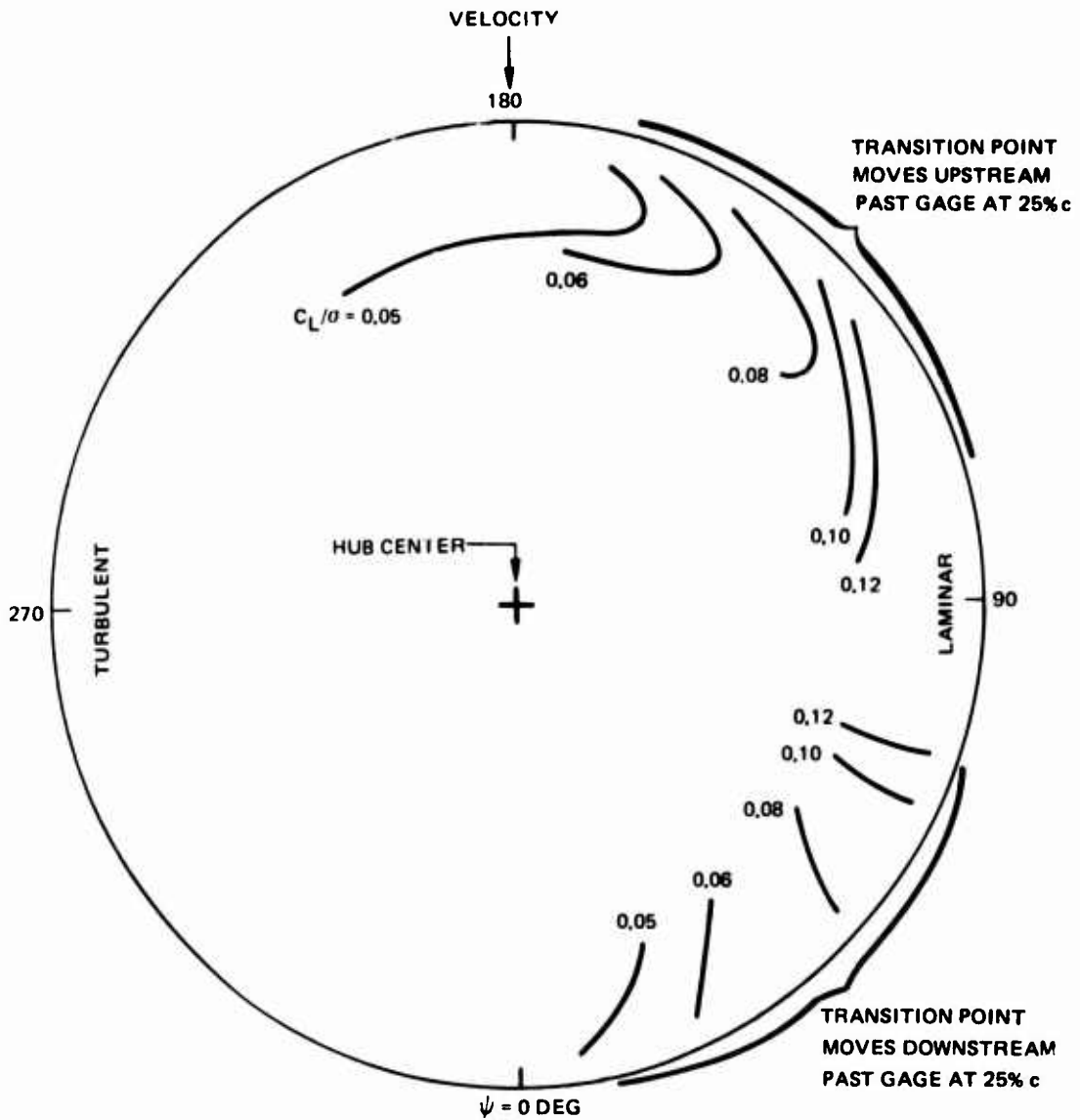


Figure 59. Azimuthal Extent of Laminar and Turbulent Boundary Layer at 25% Chord as Determined From Hot-Film Gage Data.

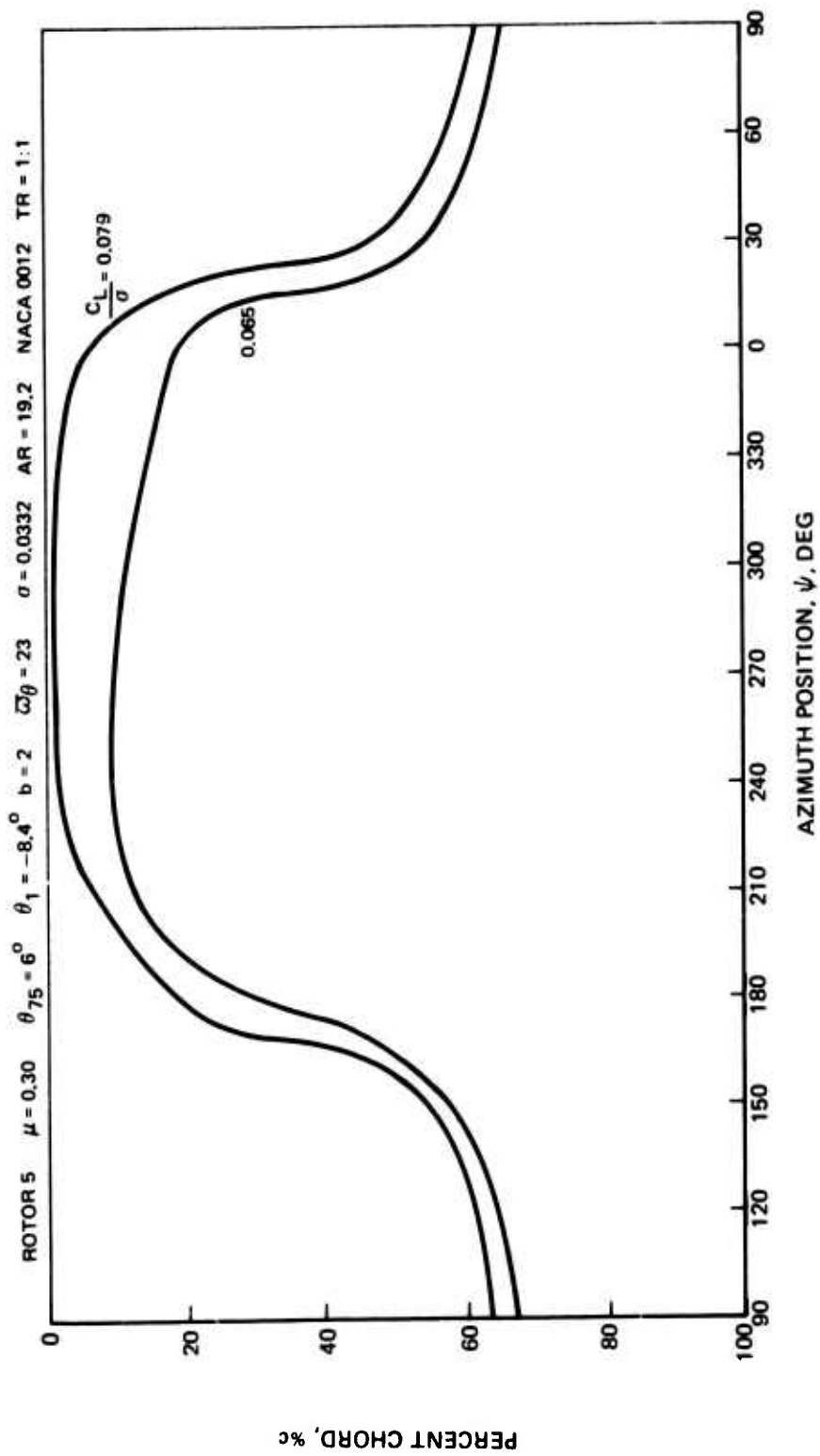


Figure 60. Chordwise Variations in Location of Boundary Layer Transition Point at 85% Span.

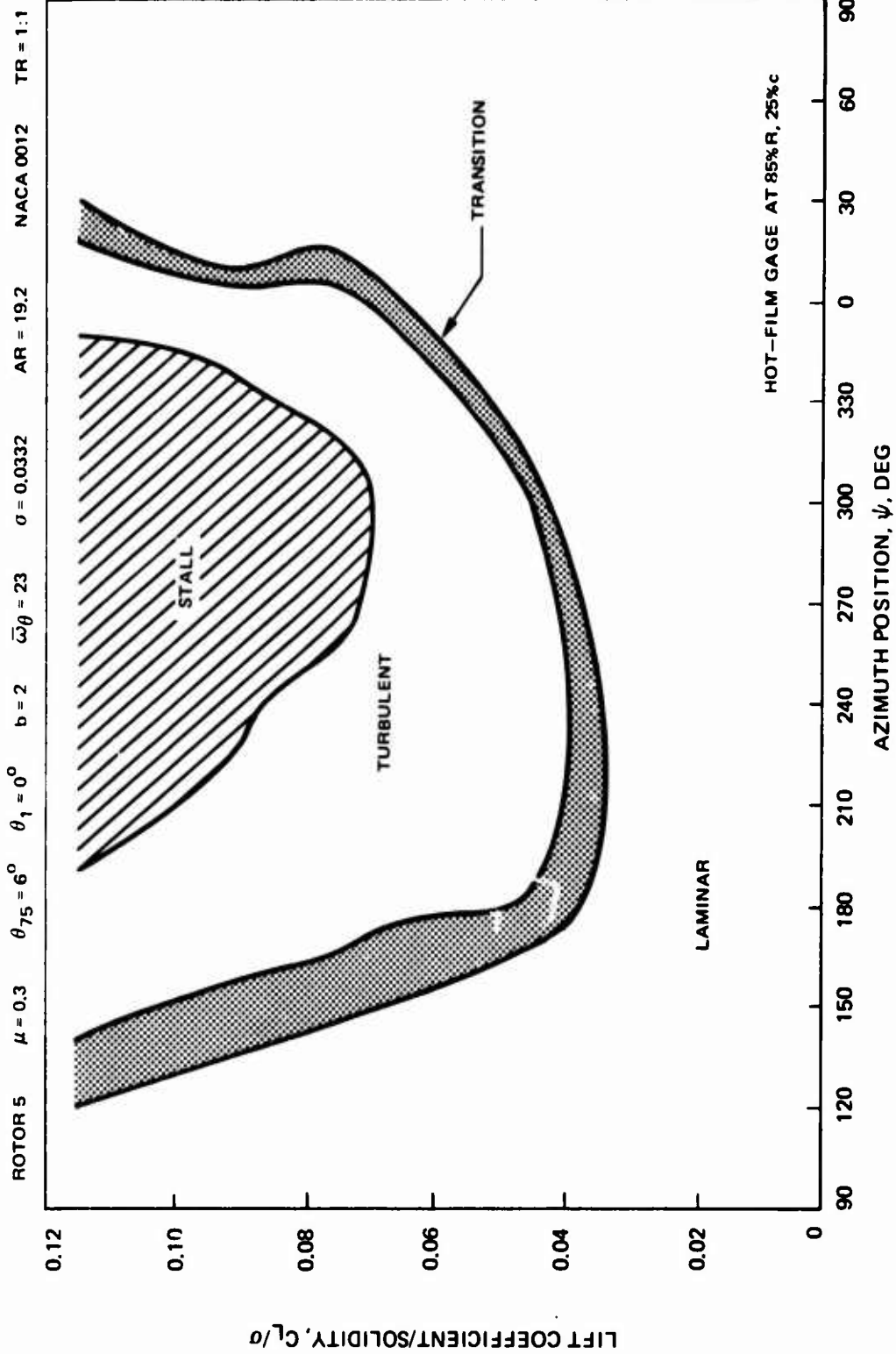
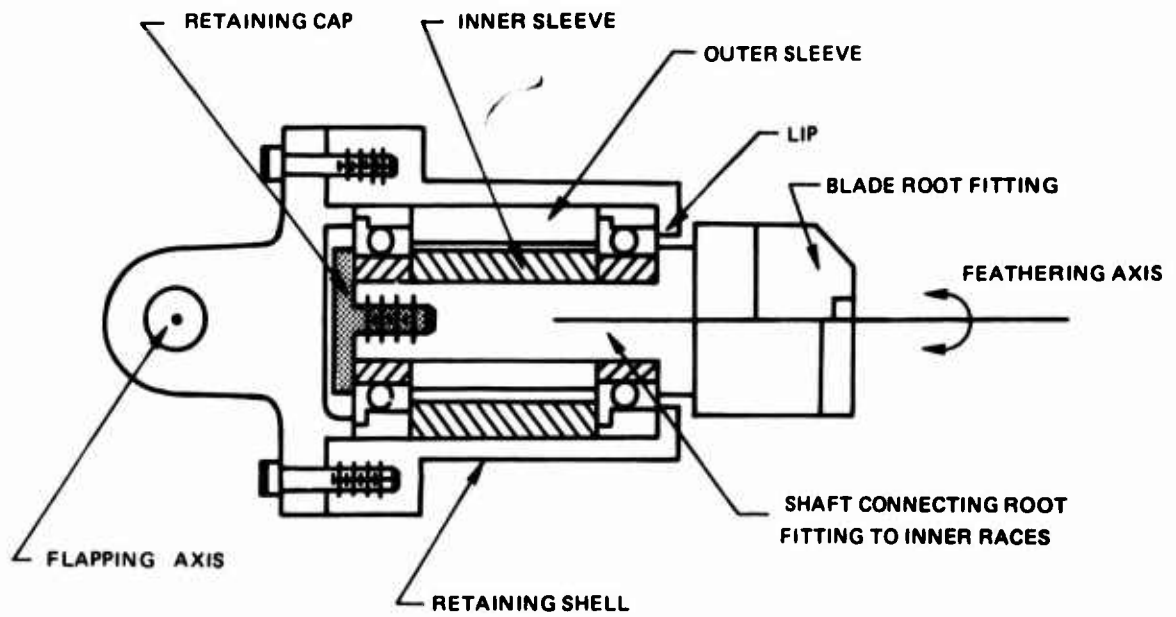


Figure 61. Effect of Thrust Level on Boundary Layer Flow Characteristics as Determined From Hot-Film Gages.

(FULL SCALE)



NOTE: ALL SHADED PARTS ROTATE WITH THE ROOT FITTING

Figure 62. Schematic Cross Section of Torsional Flexure.

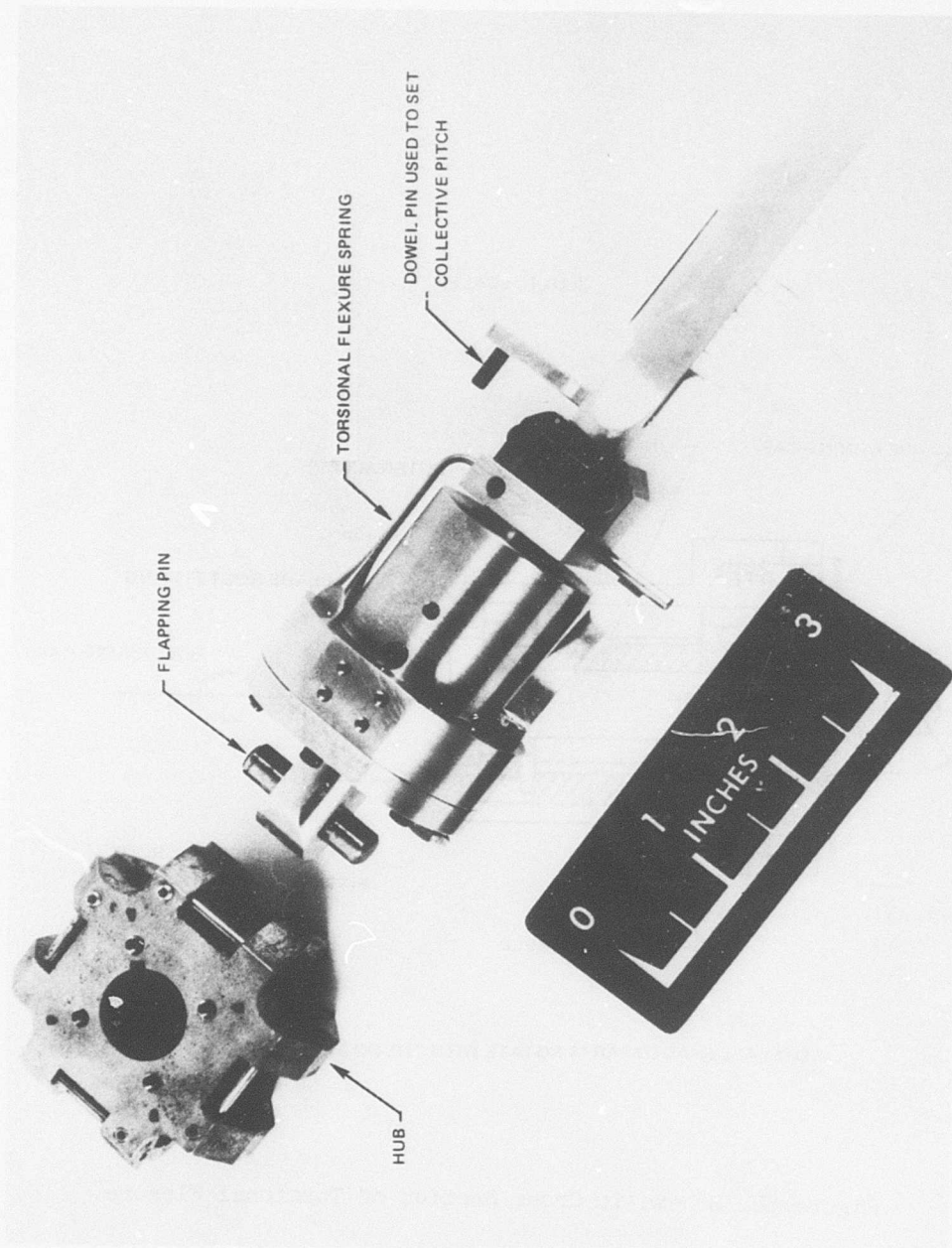


Figure 63. Hub, Torsional Flexure, and Blade.

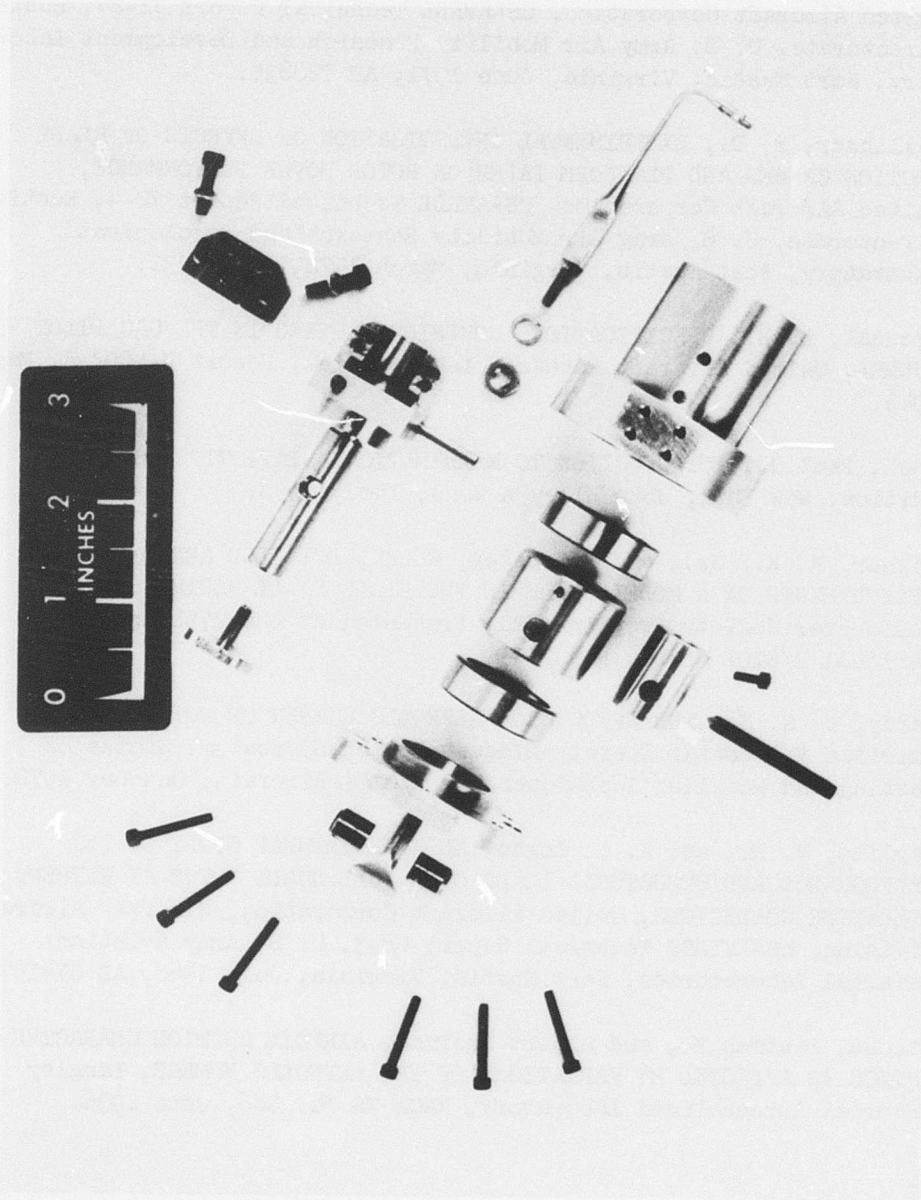


Figure 64. Exploded View of Torsional Flexure.

REFERENCES

1. Landgrebe, A. J., AN ANALYTICAL AND EXPERIMENTAL INVESTIGATION OF HELICOPTER ROTOR HOVER PERFORMANCE AND WAKE GEOMETRY CHARACTERISTICS, United Aircraft Corporation, USAAMRDL Technical Report 71-24, Eustis Directorate, U. S. Army Air Mobility Research and Development Laboratory, Fort Eustis, Virginia, June 1971, AD 728835.
2. Bellinger, E. D., EXPERIMENTAL INVESTIGATION OF EFFECTS OF BLADE SECTION CAMBER AND PLANFORM TAPER ON ROTOR HOVER PERFORMANCE, United Aircraft Corporation, USAAMRDL Technical Report 72-4, Eustis Directorate, U. S. Army Air Mobility Research and Development Laboratory, Fort Eustis, Virginia, March 1972, AD 743232.
3. Brendal, D. H., SPECIFICATIONS COVERING TESTING IN THE UAC PILOT WIND TUNNEL, United Aircraft Research Laboratories, Report R-5002-A, May 1945.
4. Hoel, Paul G., INTRODUCTION TO MATHEMATICAL STATISTICS, Second Edition, New York, John Wiley & Sons, Inc., 1958.
5. Fisher, R. K., Jr., and McCroskey, W. J., DETAILED AERODYNAMIC MEASUREMENTS ON A MODEL ROTOR IN THE BLADE STALL REGIME, American Helicopter Society Preprint 521, Presented at the 27th Annual National V/STOL Forum, May 1971.
6. Hardy, W. G. S., THE EFFECTS OF REYNOLDS NUMBER ON ROTOR STALL, American Helicopter Society Mideast Region Symposium, Status of Testing and Modeling Techniques for V/STOL Aircraft, October 1972.
7. Paglino, V. M., and A. H. Logan, AN EXPERIMENTAL STUDY OF THE PERFORMANCE AND STRUCTURAL LOADS OF A FULL-SCALE ROTOR AT EXTREME OPERATING CONDITIONS, United Aircraft Corporation, Sikorsky Aircraft Division, USAAVLABS Technical Report 68-3, U. S. Army Aviation Materiel Laboratories, Fort Eustis, Virginia, July 1968, AD 674187.
8. Jacobs, Eastman N., and Albert Sherman, AIRFOIL SECTION CHARACTERISTICS AS AFFECTED BY VARIATIONS OF THE REYNOLDS NUMBER, Langley Memorial Aeronautical Laboratory, NACA TR No. 586, June 1936.

APPENDIX TORSIONAL FLEXURES

INTRODUCTION

A unique set of torsional-flexure blade cuffs was designed and fabricated for this study to provide a means of selectively varying blade torsional frequency. The design utilizes low-friction angular-contact ball bearings (which have their axes of rotation coincident with the feathering axis of the blade) to carry the centrifugal load of the blade. The torsional stiffness (or torsional frequency) is determined by means of a spring in the form of a solid steel rod bent into an L-shape. Springs with different diameters (and hence different stiffnesses) are used to vary the blade torsional frequency.

FLEXURE DESIGN

The schematic cross section of the flexure shown in Fig. 62 illustrates the placement and action of the load-carrying bearings. The centrifugal load is transmitted from the blade root fitting to the inner races of the bearings by the retaining cap and the inner sleeve, and then via the balls to the outer races of the bearings. The outer races of the bearings then transmit the load to the hub through the housing via the outer sleeve and the lip on the end of the housing. Except for the restraining action of the torsional spring (not shown in Fig. 62) the root fitting and blade are free to rotate about the feathering axis of the blade. The inner and outer sleeves were machined to the same length in matched pairs so that the two bearings share the centrifugal load equally. The entire assembly, including the blade, root fitting, housing, bearings, etc., is free to rotate (as a rigid body) about the flapping axis. The rigidity and precision of the torsional flexure unit eliminate any pitch-lag coupling. Edgewise bending moments from the blade are transmitted to the hub by forces (transverse to the feathering axis of the blade) induced in the bearings by the shaft which is integral with the blade root fitting. Figure 63 shows an assembled flexure with a blade installed.

The torsional stiffness is provided solely by the flexure spring. By loosening a nut and a set screw, the flexure springs can be removed and/or interchanged without disturbing the rest of the rotor assembly. A set screw locks out the torsional degree of freedom for operating under fixed-root conditions. Blades are interchanged by removing the retaining cap which

is held in place by two cap screws (see Fig. 63), and simply loosening the screws allows the collective pitch to be set. The blade replacement, collective pitch setting, and the torsional spring replacement operations are mutually independent.

In the event of torsional oscillations of extreme amplitude or fatigue failure of the flexure spring, the torsional deflection of the blade is limited by a set screw which extends through a slot in the outer case. The maximum deflection is constrained to ± 15 deg.

An exploded view of the torsional flexure is shown in Fig. 64. Small strain gages were attached to the flexure spring rods and calibrated to provide a dynamic means of measuring torsional deflection. Sealed-type angular-contact ball bearings were used to prevent contamination from interfering with a free-rotating action. Very close tolerances were held during the machining of the flexures; as a result, the shaft and root fitting were able to rotate freely (with the fail-safe set screw and flexure spring removed) in the assembled flexure, and yet there was no discernible transverse play in the shaft when edgewise or flatwise loads were applied.

SIZING OF FLEXURE SPRINGS

The sizing of the flexure springs (or rods) to provide the required torsional frequencies was done in the following manner. First, knowing the geometry of the flexure assembly, the torsional inertia of those components which rotate with the blade (about the feathering axis) was calculated. This quantity when added to the known torsional inertia of the blade yielded an estimate of the total torsional inertia of the blade-flexure system. Then, based on a simplified model of the spring and flexure, a relationship between the diameter of the flexure rod and its equivalent torsional spring constant was derived. Knowing the torsional inertia and the spring constant, the dependence of torsional frequency on flexure rod diameter was obtained assuming small amplitude motion. Based on the desired nominal torsional frequencies of 4, 8, 12 cycles/rev, three diameters of flexure rod were calculated, and the flexure springs were machined, bent, and heat treated.

Following this, small strain gages were attached to the flexure rods, and a test rig was assembled to check the static stiffness and torsional frequency of the flexures. The rotor hub was rigidly clamped in a very stiff support frame with a flexure and blade attached. With the blade free to flap and oscillate in torsion, a 300-lb tensile load was applied to the end of the blade to simulate the centrifugal load under test

conditions. The static stiffness (spring constant) of the flexure was determined by applying a known moment to the blade about the feathering axis and measuring the resulting torsional deflection. The torsional frequency of vibration of the blade-flexure system was found by wiring the output of the strain gage bridge on the flexure rods to a memory-type oscilloscope, plucking the blade to obtain a torsional oscillation, and then recording the trace of the vibration on the oscilloscope. The results of these tests showed that the flexure springs were stiffer than predicted. An additional set of flexure rods of smaller diameter to produce the 4-cycle/rev torsional frequency was then machined based on an extrapolation of the experimental frequency results.

Because the true values of the torsional frequencies could only be determined from a rotating test, the final evaluations were made during the actual testing of the rotors. The frequencies were found by operating the rotor in a stalled condition (where large amplitude torsional oscillations become pronounced) and calculating the values from the traces on the recording oscillograph. The flexure rod diameters and their corresponding torsional frequencies are summarized below.

Flexure Rod Diameter (in.)	<u>1st Torsional Frequency</u>	
	<u>Nominal</u> (cycles/rev)	<u>Measured</u> (cycles/rev)
0.050	4	5
0.071	8	9
0.103	12	12

LIST OF SYMBOLS

a_{ng}	nth harmonic of blade flapping referenced to rotor shaft, positive is flap up over the nose, deg
AR	Blade aspect ratio, R/c
b	Number of blades
c	Blade chord at 0.75 R or as noted, in.
C_D	Rotor drag coefficient, $D/\rho\pi R^2(\Omega R)^2$
C_{De}	Effective drag coefficient, $D_e/\rho\pi R^2(\Omega R)^2$
C_L	Rotor lift coefficient, $L/\rho\pi R^2(\Omega R)^2$
C_Q	Rotor torque coefficient, $Q/\rho\pi R^3(\Omega R)^2$
D	Rotor drag, lb
D_e	Rotor effective drag, $D_e = D + (1/\mu)(Q/R)$, lb
e	AC component of hot-film voltage, v
E	DC component of hot-film voltage, v
E_0	Hot-film voltage at zero flow velocity, v
L	Rotor lift, lb
M	Blade pitching moment, in.-lb
P	Cycles per rotor revolution
Q	Rotor torque, ft-lb
R	Rotor radius, ft or in. as noted
\bar{r}	Blade radial station nondimensionalized by R
TR	Blade taper ratio, chord at center of rotation divided by chord at tip

U	Local blade section velocity component parallel to plane of rotation, ft/sec
α_{OL}	Blade section angle of attack at zero lift, deg
α_s	Rotor shaft angle, positive is nose-up deflection of plane of rotation relative to tunnel velocity, deg
α_{TPP}	Rotor tip path plane angle of attack, deg
$\beta_{\frac{1}{2}PTP}$	Half peak-to-peak blade flapping, deg
θ	Blade elastic torsional deflection, deg
θ_1	Blade linear twist, positive when root pitch is less than tip pitch, deg
θ_{75}	Blade collective pitch as measured at the 0.75 R station, deg
μ	Advance ratio
ρ	Air density, lb-sec ² /ft ⁴
σ	Rotor solidity, bc/ πR
σ_{E_n}	nth harmonic of blade edgewise stress, ksi
$\sigma_{E_{\frac{1}{2}PTP}}$	Half peak-to-peak blade edgewise stress, ksi
σ_{F_n}	nth harmonic of blade flatwise stress, ksi
$\sigma_{F_{\frac{1}{2}PTP}}$	Half peak-to-peak blade flatwise stress, ksi
τ	Local outflow angle as defined on Fig. 6, deg
ψ	Blade azimuth position measured from the downstream position, deg
$\bar{\omega}_\theta$	Torsional natural frequency nondimensionalized by rotor rate of rotation
Ω	Rotor rate of rotation, rad/sec